Numerical and Experimental Study of Dynamics and Vibration Control of Flexible Joint Robots

by

Minh Nha PHAM

THESIS PRESENTED TO ÉCOLE DE TECHNOLOGIE SUPÉRIEURE IN PARTIAL FULFILLMENT OF THE REQUIREMENTS FOR THE DEGREE OF DOCTOR OF PHILOSOPHY
PH. D.

MONTREAL, MARCH 2, 2020

ÉCOLE DE TECHNOLOGIE SUPÉRIEURE
UNIVERSITÉ DU QUÉBEC

BOARD OF EXAMINERS

THIS THESIS HAS BEEN EVALUATED

BY THE FOLLOWING BOARD OF EXAMINERS

Prof. Zhaoheng Liu, Thesis Supervisor
Department of Mechanical Engineering at École de technologie supérieure

Prof. Ilian Bonev, President of the Board of Examiners
Department of Systems Engineering at École de technologie supérieure

Prof. Antoine Tahan, Member of the jury
Department of Mechanical Engineering at École de technologie supérieure

Prof. Pierre Bélanger, Member of the jury
Department of Mechanical Engineering at École de technologie supérieure

Prof. Youmin Zhang, External Evaluator
Department of Mechanical, Industrial & Aerospace Engineering at Concordia University

THIS THESIS WAS PRENSENTED AND DEFENDED

IN THE PRESENCE OF A BOARD OF EXAMINERS AND PUBLIC

FEBRUARY 18, 2020

AT ÉCOLE DE TECHNOLOGIE SUPÉRIEURE

DEDICATION

For my family

ACKNOWLEDGMENT

First of all, I would like to thank my supervisor, Professor Zhaoheng Liu, for his patience, invaluable guidance, and encouragement during this research work. His scientific advice and continuous support help me to overcome all the difficulties through the period of my PhD study.

†I sincerely thank my co-supervisor, Professor Pascal Bigras for his supervision, support, and constructive suggestions during my work.

My sincere thanks also go to Mr. Bruce Hazel and Mr. Philippe Hamelin, my supervisors at Hydro-Québec Research Institute (IREQ). Their grateful support and insightful comments help me to widen my research from various perspectives. I am also grateful for all the technical help and support from the SCOMPI team at IREQ during my experimental study.

I also would like to thank the jury members for accepting to evaluate my thesis and for their helpful advice to improve this work.

Finally, I acknowledge the financial support from École de Technologie Supérieure, Natural Science and Engineering Research Council of Canada (NSERC), Hydro-Québec Research Institute, and Mitacs through the Mitacs Accelerate program.

Étude numérique et expérimentale de la dynamique et du contrôle des vibrations des robots articulations flexibles

Minh-Nha PHAM

RÉSUMÉ

Les robots sériels sont récemment l'une des méthodes les plus efficaces pour réaliser plusieurs applications industrielles, notamment le positionnement précis et les tâches d'inspection. Ils peuvent fournir une grande enveloppe de travail, un accès à des zones restreintes, des opérations dans des environnements dangereux et des travaux de précision avec un haut degré de fiabilité. Un désavantage majeur des robots sériels est le problème des vibrations, en raison de la dynamique des modes flexibles qui sont excités. La vibration provoque une détérioration de la précision du contrôle de mouvement, une grande contrainte dans les boîtes de vitesses et des déformations ou des dommages du robot manipulateur. La dynamique des modes flexibles est introduite en raison de la faible rigidité des robots manipulateurs, qui peut être causée par la flexibilité des articulations ou des membrures. Indépendamment de la taille et de la conception, la plupart des robots sériels sont encore assez flexibles avec la première résonance dans les basses fréquences d'environ 10 Hz. Pour éviter les conséquences causées par les vibrations, le contrôle des vibrations devient très important et doit être pris en compte dans la conception des contrôles.

L'objectif principal de cette étude est de concevoir des algorithmes de contrôle pour réduire les vibrations des robots sériels avec articulations flexibles. Les procédures de conception de contrôleur proposées peuvent être appliquées à divers robots industriels et sont testées expérimentalement sur un robot industriel à six articulations, le SCOMPI, actuellement en développement à l'Institut de recherche d'Hydro-Québec. Pour atteindre cet objectif, deux phases d'étude sont proposées.

L'objectif de la première phase est d'étudier la dynamique et de concevoir un algorithme de contrôle des vibrations pour un robot à articulation unique. Un modèle dynamique décentralisé de robot sériel avec articulation flexible est étudié. Les concepts de contrôle sont testés sur une configuration expérimentale simple composée d'une seule articulation et d'une seule membrure. Toutes les parties du système sont considérées comme rigides à l'exception d'un élément qui est l'articulation flexible. Le modèle de joint flexible unique est placé dans un environnement entièrement contrôlé, dans lequel l'accès à la commande de couple du moteur, à la référence du moteur ou aux états de rétroaction est disponible. Pour cet objectif, un contrôleur à deux étages amélioré est proposé, qui combine deux parties. La première partie est un contrôleur à deux étages basé sur la commande de backstepping, qui considère la position du moteur comme une entrée de commande virtuelle pour la dynamique côté membrure. La seconde partie est un observateur d'état et de perturbation, qui compense les

perturbations et reconstruit les mesures indirectes. La simulation numérique et les résultats expérimentaux valident que le contrôleur proposé améliore efficacement les performances de contrôle en termes de réduction des vibrations des membrures, d'extension de la bande passante et d'atténuation de l'erreur cinématique du réducteur d'entraînement harmonique du joint. Les limites du contrôleur proposé sont également discutées. Les performances de contrôle dépendent des paramètres du système, qui doivent être correctement identifiés. Cela nécessite également des efforts pour régler manuellement les gains du contrôleur. Et surtout, le contrôleur proposé doit avoir accès à la commande de couple du moteur pour implémenter son algorithme. Cependant, il convient de mentionner que les résultats de la première phase valident l'hypothèse de modélisation sous-jacente pour le joint flexible et que l'architecture en deux étages est réalisable à des fins de contrôle des vibrations.

Sur la base des résultats prometteurs du contrôle des vibrations pour le robot à articulation unique, la deuxième phase consiste à adapter les connaissances acquises pour un cas qui est beaucoup plus général, un robot série industriel à articulations multiples. Il y a une décision à prendre, soit qu‘une configuration expérimentale multi-joint est construite, soit qu‘un robot sériel existant est utilisé comme banc d'essai. Avec la première option, le contrôleur développé dans la première phase peut être directement appliqué. Cependant, la construction d'une nouvelle configuration expérimentale multi-joint peut nécessiter beaucoup d'efforts et de temps. La dernière option, utilisant un robot industriel existant comme banc d'essai, présente un gros avantage. Cela coûte beaucoup moins cher car la main-d'œuvre humaine, le matériel pour construire les composantes sont économisés et tous les éléments mécaniques ou électroniques sont inclus. Cependant, le nouveau contrôleur doit se conformer à l'interface de contrôle existante du robot. L'une des contraintes est que le robot est contrôlé en mode position et que l'accès au couple de joint n'est pas disponible. Sans accès à la commande de couple du moteur, le contrôleur proposé pour le robot à articulation unique dans la première phase ne peut pas être directement appliqué.

Dans l'étude de cette deuxième option, un robot industriel sériel à articulations multiples est utilisé pour développer un algorithme de contrôle des vibrations. Bien qu'un nouveau contrôleur doive être développé, il partage toujours certains aspects du modèle dynamique de robot avec articulation flexible développé dans la première phase. De plus, il peut être facilement industrialisé par la suite car toutes les contraintes sont déjà prises en compte. Notez que, en raison du fait que l’accès à la commande de couple du moteur n'est pas disponible, le contrôleur proposé doit être basé sur la commande de position du moteur.

L'objectif de la deuxième phase est de concevoir des algorithmes de contrôle des vibrations pour les robots industriels à articulations flexibles multiples. Un modèle flexible décentralisé est introduit, dans lequel la rigidité de couplage localisée est prise en compte. Dans le premier étage, une entrée à mise en forme variable dans le temps façonne la dynamique de contrôle rigide en une dynamique souhaitée qui ne produit pas de vibrations. Un deuxième étage est ajouté pour augmenter le rejet des perturbations. Un prédicteur de Smith généralisé est développé pour compenser le retard et le filtre passe-bas des capteurs de rétroaction. Des simulations numériques et des expériences sur un robot à six articulations SCOMPI confirment

que le contrôleur proposé améliore les performances de contrôle en termes de bande passante, d'atténuation des vibrations et de rejet des perturbations.

Mots clés: robot articulation flexible, contrôle des vibrations, contrôleur à deux étages, observateur de perturbation, observateur d'état, formation d’entrée variant dans le temps, prédicteur de Smith.

Numerical and experimental study of dynamics and vibration control of flexible joint robots

Minh-Nha PHAM

ABSTRACT

Serial robots are recently one of the most effective methods to realize several industrial applications including precision positioning and inspection tasks. They can provide a large working envelope, access to restricted areas, operations in hazardous environments, and precision works with high degree of reliability. A major issue of serial robots is vibration, due to flexible modes dynamics that are excited. The vibration causes deterioration of motion control accuracy, large stress in the joint gearboxes, and deformations or damages of the robot manipulator. The flexible modes dynamics are introduced due to the low rigidity of robot manipulators, which may be caused by the flexibility of joints or links. Regardless of size and design, most serial robots are still quite flexible with the first resonance in low frequencies of about 10 Hz. To avoid the consequences caused by vibrations, vibration control becomes very important and needs to be taken into account in control design.

The main objective of this study is to design control algorithms to reduce vibration of flexible joint robots. The proposed controller design procedure can be applied for various industrial robots and is tested experimentally on an industrial six-joint robot namely SCOMPI, developed at Hydro-Québec's Research Institute. In order to achieve that end, two phases of study are proposed.

The objective of the first phase is to study the dynamics of a single flexible joint robot and design a control algorithm to reduce the vibration. Decentralized dynamic model of flexible joint robot is studied. Control concepts are tested on a simple experimental setup consisting of only one joint and one link. All parts of the system are considered rigid except for one element that is the flexible joint. The single flexible joint model is placed in a fully-controlled environment, in which access to motor torque command, motor reference, or feedback states are available. For this objective, an enhanced two-stage feedback controller is proposed, which combines two parts. The first is a two-stage feedback loop based on backstepping control, which considers the motor position as a virtual control input for the link side dynamics. The second is a disturbance-state observer, which compensates disturbances and reconstructs indirect measurements. Numerical simulation and experimental results validate that the proposed controller effectively improves control performance in terms of reducing link vibration, extending control bandwidth, and attenuating the kinematic error from the joint's harmonic drive reducer. Limitations of the proposed controller are also discussed. The control performance relies on system parameters, which need to be properly identified. It also requires effort to manually tune controller gains. And most importantly, the proposed controller needs access to motor torque command to implement its algorithm. However, it is worth mentioning

that the results of the first phase validate the underlying modelling assumption for the flexible joint and that the two-stage architecture is feasible for vibration control purpose.

Based on promising results of vibration control on single flexible joint test bench, the second phase is to adapt the acquired knowledge for a much more general case, industrial serial robot with multiple joints. There is a decision to make, either a multi joint experimental setup is built or an existing serial robot is used as a test bench. With the former option, the controller developed in the first phase can be directly applied. However, building a new multi-joint experimental setup costs a lot of effort and time. The latter option, using an existing industrial robot as a test bench, has a big advantage. It costs much less since man power, material to build things are saved and all mechanical or electronic elements are included. However, a new controller must be designed to comply with the existing robot control interface. One of the constraints is that the industrial robot is controlled in position mode and that the access to the motor torque command is not provided. Without access to the motor torque command, the controller proposed for single joint test bench in the first phase can not to be directly applied.

Considering these two options, an existing industrial multiple joint serial robot is used to develop vibration control algorithms. Although a new controller needs to be developed, it still shares some aspects of the dynamic model of flexible joint robot developed in the first phase. Also, it can be easily industrialized afterward since all constrains are already taken into account. Note that, due to the fact that access to motor torque command is unavailable, the proposed controller needs to be based on the access to motor position command.

The objective of the second phase is to design vibration control algorithms for industrial robots with multiple flexible joints. A two-stage flexible joint discrete controller is presented, where the decentralized approach is extended with a lumped stiffness to take into account the dominant coupling mode. In the first stage, a time-varying input shaping feedforward shapes the rigid closed-loop dynamics into a desired dynamics that does not produce link vibrations. A second stage is added to increase disturbance rejection. A generalized Smith predictor is developed to compensate for delay and link feedback sensor filtering. Numerical simulations and experiments on a six-joint robot manipulator SCOMPI confirm that the proposed controller improves control performances in terms of bandwidth, vibration attenuation, and disturbance rejection.

Keywords: flexible joint robot, vibration control, two-stage controller, disturbance observer, state observer, time varying input shaping, Smith predictor.

TABLE OF CONTENTS

LIST OF TABLES

Page

LIST OF FIGURES

LIST OF SYMBOLS

Symbol	Units	Description
$a_{0...7}$	-	Coefficients of denominator of $G_1(s)$
$b_{0...4}$	-	Coefficients of numerator of $G_1(s)$
b_l	Nms/rad	Link viscous friction
b_m	Nms/rad	Motor viscous friction
$\mathbf{B}_l$	Nms/rad	Joint damping matrix
$\mathbf{B}_m$	Nms/rad	Motor viscous friction matrix
$\mathbf{C}(\mathbf{q}_l, \dot{\mathbf{q}}_l)$	-	Coriolis and Centrifugal matrix
C_{FB}	-	Feedback of rigid controller
C_{FF}	-	Feedforward of rigid controller
d_l	Nm	Disturbance on link side
d_m	Nm	Disturbance on motor side
$\hat{d}_{l,m}$	Nm	Estimated disturbance on link or motor side
$\tilde{d}_{l,m}$	Nm	Disturbance estimation error
$\mathbf{g}(\mathbf{q}_l)$	-	Gravitational forces vector
J_e	kgm^2	Effective inertia
J_l	kgm^2	Link inertia
J_m	kgm^2	Motor inertia
$\mathbf{J}_m$	kgm^2	Motor inertia matrix
k_c	kNm/rad	Coupling stiffness
k_j	kNm/rad	Joint effective stiffness
$K_{p1,d1,i1}$	-	Rigid control gains
$K_{p2,d2,i2}$	-	Second-stage PID gains
k_r	kNm/rad	Reducer stiffness
$\mathbf{K}_r$	kNm/rad	Reducer stiffness matrix
$\mathbf{M}_l(\mathbf{q}_l)$	-	Link inertia matrix
N_r	-	Reducer gear ratio
$\mathbf{N}_r$	-	Gear ratio matrix
q_l	rad	Link position
q_m	rad	Motor position
q_r	rad	Reducer output position

T_{d1}	s	Delay in rigid control feedback loop
T_{fb1}	s	Delay in motor feedback path
T_s	s	Sampling time
T_w	s	Compensated distortion delay
$\mathbf{u}$	Nm	Motor torque vector
u	Nm	Motor torque
$\overline{x}(n)$	rad	Filtered time inverse response vector
$\boldsymbol{\tau}_j$	Nm	Joint torque vector
ω_z	rad/s	Anti-resonant frequency
ω_p	rad/s	Resonant frequency
ω_c	rad/s	Warping frequency
ω_{n1}	rad/s	Natural frequency of rigid control
ω_{n2}	rad/s	Natural frequency of the second-stage PID
$\omega_{lc,mc}$	rad/s	Cut-off frequencies of low-pass filters
ζ_2	-	Damping ratio of the second-stage PID
ζ_1	-	Damping ratio of rigid control
λ_1	-	Rigid control frequency rate
λ_2	-	Second-stage PID frequency rate

INTRODUCTION

Vibration problem

Serial robots are used extensively in industrial applications including pick and place, assembly, machining, and inspection tasks. This is because serial robots can work on large parts in single operation setup, due to their wider working envelopes. In addition, robots can provide a cost-effective solution, by accurately following arbitrarily complex trajectories and accessing restricted areas. Robots are capable of operating in hazardous environments and delivering precision works with high degree of reliability.

At Hydro-Québec's Research Institute, a robot named "SCOMPI", which stands for "Super COMPact Ireq robot" is developed for on-side maintenances and inspections. It is a track-based six-joint serial robot with a total weight of about 33 kg and is designed to access difficult-to-reach locations such as turbine blades and unmovable parts like large hydropower equipment.

A major issue of serial robots in general and of the SCOMPI robot in particular is vibration. Vibration occurs when the trajectories, disturbances, or noises excite flexible modes, which are introduced by the low rigidity of the robot manipulator. The vibration may reduce motion control performance, induce large stress in the gearboxes, deform and damage the robot manipulator. The low rigidity, however, is an inherent natural property of open chain kinematic systems. In some particular cases such as space robotic arms, links can be the major source of compliance as they become longer and slender. For most modern industrial robots, the links are considered fairly rigid and the major source of flexibility comes from the joints. The joint speed reducer, the drive shaft, or the bearings may deflect during torque transmission, resulting in a degradation of the overall stiffness.

To increase the stiffness, mechanical stiffening of robot components is an option. A concept of mixing parallel and serial links has been introduced to increase the stiffness of industrial robots with maximum payload above 110 kg, such as Fanuc M-900*i*B, M-2000*i*A, or M-410*i*C robots. However, modification of existing robots is costly and generally requires a lot of effort. It is even almost impossible in some industrial robots, which do not allow modifying any part of the hardware.

Vibration control

Therefore, instead of trying to modify the robot structure, it is desirable to leave it untouched. Alternatively, much research effort has been devoted to design vibration control algorithms that takes into account the flexible dynamics of the robot manipulators. By introducing appropriate control signals, the controller may shape the robot dynamics into a desired dynamics where the vibration due to the flexibility is attenuated. Due to its effectiveness, the vibration control is a key to the robot's performance in terms of accuracy and speed.

There are several difficulties in the development of vibration control algorithms for flexible joint robots. The presence of flexibility introduces more degrees of freedom, resulting in more complicated dynamic models. In addition, when the control architectures that do not take the flexibility into account are used, the control gains should be small to avoid exciting flexible modes. As a price, the control performance in terms of the control bandwidth (defined by a band of frequencies that the output can track the reference input with a small error) and the disturbance rejection (defined by the effect of the disturbances on the output) are low. Another problem is the configuration-dependent of robot dynamics, which introduces more challenges to the robustness of the controllers. Besides, many constrains of industrial robots also pose more challenges to the development of control algorithms. For example, the SCOMPI robot just provides an access to the motor target position while the access to the motor torque and velocity feedback are totally unavailable. The position feedback is accessible, but it comes

with delay and quantization noises. Due to these difficulties, the development of control algorithms, which are practical and suitable for vibration control of the industrial flexible joint robots, is still an open problem.

Organization of this thesis

This thesis focuses on vibration control algorithms for flexible joint robots. The proposed method is then validated by numerical simulations and experiments on the industrial serial robot SCOMPI at Hydro-Québec's Research Institute. The thesis is arranged into four chapters. Chapter 1 presents the background and literature review on vibration control of flexible joint robot. Chapter 2 presents the main objectives, specific objectives, and methodologies needed to be carried out. Chapter 3 and chapter 4 respectively present technical works on designing vibration control algorithms to meet the specific objectives of this thesis. Numerical simulations and experimental results are presented to validate the effectiveness of proposed controllers in terms vibration attenuation, extending bandwidth, and disturbance rejection. The conclusion and recommendations are provided at the end of this thesis.

CHAPTER 1

BACKGROUND AND LITERATURE REVIEW

This chapter presents a background and literature review on dynamic models of robot manipulators and recent motion/vibration control techniques for flexible joint robots. A discussion on remaining problems is also given at the end of this chapter.

1.1 Dynamic models of robot manipulators

Dynamic models of robot manipulators are reviewed in this section. The dynamic model of robot manipulator is important in several ways. Firstly, appropriate dynamic models can be used to perform numerical simulations of robots. The simulation results predict the behavior of the robots under many different operating conditions. Secondly, the dynamic model can be used as a plant to develop control strategies. Some controllers use the dynamic model to determine their optimal gains while others use it to compute feedforward or compensation parts. In the following, dynamic models of both rigid and flexible joint robots are discussed.

1.1.1 Rigid manipulators

This section presents the equations of motion for a rigid-body serial robot manipulator. The robot manipulator is an open kinematic chain with revolute and prismatic joints. For some applications, such as arc welding or grinding, it is necessary to move the end effector of a manipulator from point to point rapidly and accurately. The dynamics of the manipulator plays an important role in achieving such high-speed and low steady-state error performance. There are two types of dynamics problems: direct dynamics and inverse dynamics. The direct dynamics problem is to find the response of a robot arm corresponding to some applied torque and/or forces. This is useful for simulating the manipulator. The inverse dynamics problem is to find the actuator torques and/or force required to generate a desired trajectory of the

manipulator. This formulation of dynamics may be useful for the problem of controlling the manipulator. The problem can be formulated in the joint space or in the Cartesian space. The dynamical equations of motion can be formulated by several methods. One of the most frequently used is the application of the Newton and Euler laws. Newton's and Euler's equations are written once for each body of a manipulator, resulting a system of equations with applied forces and constrained forces. Dynamic models can also be derived using Lagrange's equation of motion or Kane's method.

The dynamic model of rigid serial robot can be written in the form (Craig, 1989; Tsai, 1999):

$$\mathbf{M}_l(\mathbf{q}_l)\ddot{\mathbf{q}}_l + \mathbf{C}(\mathbf{q}_l, \dot{\mathbf{q}}_l)\dot{\mathbf{q}}_l + \mathbf{g}(\mathbf{q}_l) = \mathbf{u} \tag{1.1}$$

where $\mathbf{q}_l$ is an $n\times 1$ vector of link angular displacement, $\mathbf{u}$ is an $n\times 1$ vector of actuator torque, $\mathbf{M}_l(\mathbf{q}_l)$ is the $n\times n$ mass matrix of the manipulator, $\mathbf{C}(\mathbf{q}_l, \dot{\mathbf{q}}_l)$ is an $n\times 1$ vector of Coriolis and centrifugal terms, and $\mathbf{g}(\mathbf{q}_l)$ is an $n\times 1$ vector of gravity terms.

1.1.2 Flexible joint robot manipulators

Joint and link flexibilities introduce additional degrees of freedom, resulting in a much more complex dynamic model than the rigid robot dynamics. Depending on the mechanical design of the robot, the flexibility of joints and links may contribute to the overall flexibility in different ways. For example, in the case of aerospace manipulators with long and slender links, link becomes a major source of flexibility. For general industrial manipulators, the effect of flexible links on the vibration is normally much smaller than that of joints.

In this study, we focus on a robot with flexible joints. The flexible joint robot is modelled as an open kinematic chain having $n+1$ rigid bodies, the base and the n links, interconnected by n (rotary or prismatic) joints undergoing deflection, and actuated by n electrical drives (Craig, 1989; Tsai, 1999). Each motor is an additional rigid body with its inertial properties. The joint

flexibility is modelled by linear torsional spring. All joints are considered to be flexible, though mixed rigid-flexible joints may be encountered in some robots due to the use of different transmission devices. When reduction gearings are present, they are modelled as being placed before the joint deflection occurs (De Luca & Book, 2008).

The dynamic model of flexible joint robot can be obtained using Newton-Euler or Lagrange formulation. The kinetic energy stored by the manipulator is the sum of the kinetic energy due to the links alone and the kinetic energy arising from the rotation of the drive rotor alone (Craig, 1989; Readman & Belanger, 1990b; Tsai, 1999). The complete dynamical model for flexible joints manipulator can be expressed as follows:

$$\begin{bmatrix} \mathbf{M}(\mathbf{q}_l) & \mathbf{S}(\mathbf{q}_l) \\ \mathbf{S}^T(\mathbf{q}_l) & \mathbf{J}_m \end{bmatrix} \begin{bmatrix} \ddot{\mathbf{q}}_l \\ \ddot{\mathbf{q}}_m \end{bmatrix} + \begin{bmatrix} \mathbf{C}(\mathbf{q}_l, \dot{\mathbf{q}}_l)\dot{\mathbf{q}}_l + \mathbf{C}_1(\mathbf{q}_l, \dot{\mathbf{q}}_l)\dot{\mathbf{q}}_m \\ \mathbf{C}_2(\mathbf{q}_l, \dot{\mathbf{q}}_l)\dot{\mathbf{q}}_l \end{bmatrix} + \begin{bmatrix} \mathbf{g}(\mathbf{q}_l) + \mathbf{k}_r(\mathbf{q}_l - \mathbf{q}_m) \\ \mathbf{k}_r(\mathbf{q}_m - \mathbf{q}_l) \end{bmatrix} = \begin{bmatrix} \mathbf{0} \\ \mathbf{u} \end{bmatrix} - \begin{bmatrix} \boldsymbol{\tau}_{V,\mathbf{q}_l} \\ \boldsymbol{\tau}_{V,\mathbf{q}_m} \end{bmatrix} \tag{1.2}$$

where $\mathbf{S}(\mathbf{q}_l)$ is an $n \times n$ strictly upper triangular matrix corresponding to the inertial coupling between motors and links, $\mathbf{k}_r$ is an $n \times n$ diagonal matrix of joint stiffness, and the dissipative terms are:

$$\begin{bmatrix} \boldsymbol{\tau}_{V,\mathbf{q}_l} \\ \boldsymbol{\tau}_{V,\mathbf{q}_m} \end{bmatrix} = \begin{bmatrix} \mathbf{D}_r(\dot{\mathbf{q}}_l - \dot{\mathbf{q}}_m) + \mathbf{B}_l\dot{\mathbf{q}}_l \\ \mathbf{D}_r(\dot{\mathbf{q}}_m - \dot{\mathbf{q}}_l) + \mathbf{B}_m\dot{\mathbf{q}}_m + \mathbf{B}_f \operatorname{sgn}(\dot{\mathbf{q}}_m) \end{bmatrix} \tag{1.3}$$

where $\mathbf{D}_r$ is an $n \times n$ joint viscosity diagonal matrix, $\mathbf{B}_l$ and $\mathbf{B}_m$ are respectively $n \times n$ diagonal matrices of link and motor viscous friction, $\mathbf{B}_f$ is an $n \times n$ diagonal matrix of motor Coulomb friction, $\operatorname{sgn}(\square)$ is the sign function.

Spong provides an assumption that the kinetic energy of the rotors is due mainly to their own rotation (De Luca, Farina, & Lucibello, 2005; M. W. Spong, 1987). This implies the inertial

coupling between motors and links vanishes, i.e. $\mathbf{S}(\mathbf{q}_l)=\mathbf{0}$ and $\mathbf{C}_1(\mathbf{q}_l,\dot{\mathbf{q}}_l)\dot{\mathbf{q}}_m=\mathbf{C}_2(\mathbf{q}_l,\dot{\mathbf{q}}_l)\dot{\mathbf{q}}_l=\mathbf{0}$. By ignoring the joint viscosity ($\mathbf{D}_r=\mathbf{0}$), the complete dynamic model is reduced to a reduce model as follows:

$$\begin{cases} \mathbf{M}_l(\mathbf{q}_l)\ddot{\mathbf{q}}_l+\mathbf{C}(\mathbf{q}_l,\dot{\mathbf{q}}_l)\dot{\mathbf{q}}_l+\mathbf{g}(\mathbf{q}_l)+\mathbf{B}_l\dot{\mathbf{q}}_l+\mathbf{k}_r(\mathbf{q}_l-\mathbf{N}_r^{-1}\mathbf{q}_m)=\mathbf{0} \\ \mathbf{J}_m\ddot{\mathbf{q}}_m+\mathbf{B}_m\dot{\mathbf{q}}_m+\mathbf{B}_f\,\mathrm{sgn}(\dot{\mathbf{q}}_m)+\mathbf{N}_r^{-1}\mathbf{k}_r(\mathbf{N}_r^{-1}\mathbf{q}_m-\mathbf{q}_l)=\mathbf{u} \end{cases} \tag{1.4}$$

The stability of flexible joint robot dynamics is presented using the theory of singular perturbations in (Mills, 1992).

A remaining problem of the robot dynamic model expressed in Eq. (1.4) is that only the reducer stiffness is taken into account. For a robot manipulator where the flexibility of other components is high, the model of Eq. (1.4) may lack accuracy.

1.2 Vibration control of flexible joint robot

This section presents the most common motion control technologies used for flexible joint robots. Model-based controllers are widely used for flexible joint robots. These controllers are favored to take advantage of the available dynamic models, which can be computed using many techniques such as Newton-Euler or Lagrange formulation. However, an identification process is normally required to obtain accurate values of parameters. Well-known model-based control algorithms for flexible joint robot are listed in the following:

- PID control (De Luca, 2000; De Luca & Flacco, 2011; De Luca, Siciliano, & Zollo, 2005; Tomei, 1991b): The PID (proportional-integral-derivative) control has three elements: a proportional term to close the feedback loop, an integral term to assure zero error to constant reference and disturbance inputs, and a derivative term to improve stability and good dynamic response. It is adapted for the flexible joint robot.

- Feed-forward control: (De Luca, 2000) shows that PD-type control law based on the nominal feed-forward computation is a viable solution for a cheap but effective implementation of a feedback controller for the various motion tasks. In (Lessard, Bigras, Liu, & Hazel, 2014), the authors demonstrated the high performance of feed-forward control compared to rigid control and singular perturbation methods in a specific experiment test rig of flexible joint and single link robot.

- Singular perturbation (Lessard et al., 2014; Wilson & Irwin, 1993): The singular perturbation method separates the system into two parts: slow dynamics and fast dynamics. The slow part has a rigid control law that ignores robot flexibility. The fast part, which takes into account the flexibility, is stabilized by linear state feedback.

- Adaptive control (Al-Ashoor, Patel, & Khorasani, 1993; An-Chyau & Yuan-Chih, 2004; Elbestawi, Yuen, Srivastava, & Dai, 1991; Ge, Lee, & Tan, 1997; Khorasani, 1991; Lee, Ge, & Wang, 2001; Readman & Belanger, 1990b; Ser Yong, Dawson, Jun, & de Queiroz, 1997; Mark W. Spong, 1989; Yin-Chieh & Jinsiang, 2011): The basic idea of adaptive control is to change the gains or other parameters in the control law according to some on-line algorithm. In this way the controller can "learn" an appropriate set of parameters during the course of its operation. This idea is especially useful for manipulators that are performing repetitive task. Without adaptation the tracking errors are also repetitive. With adaptation, the tracking performance can be improved through successive repetition.

- Robust control (D.-W. Gu, 2005; Jae Young, Je Sung, & Jong Hyeon, 2007; Kwan & Yeung, 1993; Mark W. Spong, 1989; Tae-Jun, Jaeyoung, & Jong Hyeon, 2007; Yeon, Yim, & Park, 2011): robust control techniques are based on worst case estimates of the uncertainty or mismatch between the plant and the inner loop control. In these approaches the inner loop control law is fixed and the gains in the outer loop are set according to the estimate of the uncertainty.

- Backstepping approach (J. H. Oh & Lee, 1997): This approach considers joint elastic torque or motor position as an intermediate virtual input to control the link dynamics. The backstepping control is favored to take advantage of the available dynamic models including the joint flexibility. Both motor and link side feedback are used in the control architecture.

In recent years, model-free control has been proposed for flexible joint robots. An advantage of these control techniques is that they do not require a precise system model in the design of the controller. However, they normally need data to train their networks and several iterations to improve control performance. Some literatures are listed in the following:

- Fuzzy PID control (Botsali, Kalyoncu, Tinkir, & Onen, 2010; Malki, Misir, Feigenspan, & Guanrong, 1997): authors proposed the mathematical principle for the fuzzy PID controller design, including the fuzzification, rule-base and defuzzification. In this design, a standard PD+I controller configuration is conducted. The design of the fuzzy PID controller consists of two parts: one fuzzy PD and one fuzzy I controllers.

- Neural network control (Chatlatanagulchai & Meckl, 2005; Ge et al., 1997; Hunmo & Parker, 1993a, 1993b; Miao & Wang, 2013; Shipitko & Zmeu, 2003; Yeşildirek, Vandegrift, & Lewis, 1996): In (Chatlatanagulchai & Meckl, 2005), authors derive a desired control law based on Lyapunov's equations. Then, a three-layer neural network is proposed to learn unknown parts of the desired control laws. However, the time-varying case such as the change in payload has not been fully covered in this research.

- Iterative learning control: Iterative learning control is a data-driven methodology that iteratively uses the error profile from previous trails to compute the system inputs for the next iteration (W. Chen & Tomizuka, 2014). Normally, the iterative learning control performs as an add-on feedforward controller in addition to the existing real-time feedback controller, to further enhance the performance over the standalone real-time feedback system. A drawback of iterative learning control is that it requires the

system to perform repetitive tasks under the same conditions. This assumption may be invalid if the robot follows arbitrary trajectories under effect of different disturbances.

Control techniques mentioned above normally require access to motor torque command. This requirement becomes an issue for many industrial robots, in which robot joints are equipped with built-in motion controller and no access to motor torque command is provided. In that case, input shaping of the reference profile is an effective technique to reduce vibration. As explained in (Singhose, 2009), input shaping reduces vibration of closed-loop dynamic systems by optimizing only position command signals such that they does not excited flexible modes. The shaped command signal is obtained by convolving the command signal with a sequence of impulses, known as an input shaper. Parameters of the input shaper directly relies on the natural frequencies and damping ratios of the induced vibration.

Based on the literature review, there are some important points that require more attention. The first concern is the flexible joint robot modelling. Recently, the robot dynamic model including flexible dynamics is presented. However, for simplicity, this model only takes the reducer stiffness into account while ignoring the coupling stiffness and the distortions of all other parts of the robot manipulator. To better model the behaviors of the robot manipulators with high coupling stiffness, a dynamic model including the coupling dynamics is necessary to be developed.

The second point is on the control of flexible joint robots. Based on the review of recent techniques, the following observations are drawn:

- Backstepping approach is a promising approach for motion and vibration control. No additional devices such as joint torque or acceleration sensors are needed. However, experimental study of backstepping approach is limited since the motor torque signal is very noisy. The performance of this method also relies on the knowledge of parameters, which are difficult to be precisely identified. Due to these difficulties, an

application of backstepping approach on flexible joint robot has not been fully developed in recent publications.

- Input shaping is an effective method to reduce vibration of system with limited access to the motor torque command. However, how it can be used in combination with the state feedback for industrial serial robots has not been fully detailed in previous literature.

CHAPTER 2

OBJECTIVE AND RESEARCH APPROACH

Based on the literature review, the objective and corresponding methodologies of this thesis are given in this chapter.

2.1 Objective of the thesis

Main objective:

The main objective of this work is to design control algorithms to reduce vibrations while improve control bandwidth and disturbance rejection of flexible joint robots. The control algorithms need to be robust to the changes of the robot's configurations. The control methods are expected to be practical, which can be retrofitted into industrial robots with limited access to feedback and command signals.

The effectiveness of the proposed approaches is verified by numerical simulations and experiments. Even though this study is validated using a specific robot, namely SCOMPI developed at Hydro-Québec's Research Institute, the proposed controller design procedures can be used as a practical guideline for various other industrial robots.

Specific objectives:

The main objective is broken down into a series of smaller objectives with intermediate validation. These two specific objectives are given in the following:

Specific objective 1: The first specific objective is to study dynamics and to develop a vibration control algorithm for a single flexible joint robot using a simple and well controlled testbed. The single joint testbed is designed such that all other components are much more rigid than the joint's harmonic drive reducer. A full control environment is provided, in which access to motor torque and reference profile is available. The goal of this phase of study is to find how, with this simple testbed, the vibration of a flexible joint can be attenuated.

Specific objective 2: The second specific objective is to study dynamics and to develop a control algorithm for multiple flexible joint robots. Control algorithm developed in this phase is expected to be practical, which can be consequently applied into recent industrial robots.

2.2 Research approach

The research approach used to conduct this research work is briefly discussed in the following:

For the first specific objective, a single flexible joint testbed is built to test control algorithms. A single flexible joint testbed can be built by connecting a rigid rotor and a rigid link via a harmonic drive reducer, which is considered flexible. A motion control drive providing access to motor torque command is used. A vibration control algorithm based on a two-stage feedback controller combined with dual observer is presented. The first part of the controller is a two-stage feedback loop, which considers the motor position as a virtual control input for the link side dynamics. The second is a disturbance-state observer, which compensates disturbances and reconstructs indirect measurements. Numerical simulation and experimental results on a flexible joint robot show the effectiveness of the proposed controller in terms of position tracking, link vibration and rejection of the kinematic error from the joint's harmonic drive reducer. The first objective is conducted during the first phase of this study. Details of the proposed controller are discussed in chapter 3.

Based on promising results of vibration control on the single flexible joint, the second phase is to develop vibration control algorithm for industrial serial robot with multiple flexible joints. There are two ways to establish a testbed for controller development. The first is to build a new multiple joint experimental setup, in which each joint uses the single flexible joint architecture developed in the first phase. The second is to employ an existing serial robot as a test bench. A main advantage of the former option is that the controller developed in the first phase can be directly applied. However, building a new multi-joint experimental setup costs a lot of effort and time. A big advantage of the latter option, using an existing industrial robot as a test bench,

is that it costs much less since man power are saved and all mechanical or electronic elements are already included. However, a disadvantage is that industrial robot may come with several constrains in terms of the access to its software. Industrial robots are normally controlled in position mode and an access to the motor torque reference is not provided. Without the access to the joint torque command, the controller proposed for the single joint test bench in the first phase can not to be directly applied.

Considering these two options, an existing multiple joint serial robot is selected to develop vibration control algorithm. With the option selected, a new controller based on the access to the motor position command is developed. Although the control algorithm developed in the first phase cannot be directly applied, the understanding of the dynamic model of flexible joint robot can be reused. A benefit of developing controller directly for industrial robots is that the controller can be easily industrialized afterward since all constraints are already taken into account.

A vibration control study for an industrial multiple flexible joint robot is conducted in the second phase of this study. A two-stage flexible joint controller based on input shaping is proposed. The decentralized modelling approach for flexible joint is extended with a lumped stiffness to take into account the dominant coupling mode. The proposed controller can be retrofitted into existing robots, for which access to motor torque command is unavailable. Numerical simulations and experiments on a six-joint robot manipulator confirm that the proposed controller improves control performances in terms of bandwidth, vibration attenuation, and disturbance rejection. Details of the proposed controller are discussed in chapter 4.

CHAPTER 3

A TWO-STAGE FEEDBACK CONTROLLER SUPPORTED BY DISTURBANCE-STATE OBSERVER FOR VIBRATION CONTROL OF A FLEXIBLE JOINT ROBOT

The performance of robot manipulator is limited due to the presence of the joint flexibility, which introduces additional degrees of freedom to the robot dynamic model and additional vibration modes. To overcome these problems, this chapter introduces an enhanced two-stage feedback controller, which is a combination of two subsystems. The first subsystem is a two-stage feedback control, in which the motor position is considered as a virtual control input of the link side dynamics. The second subsystem is a dual observer, which combines a disturbance observer and a state observer. The dual observer compensates disturbances and estimates the feedback signals that could not be measured directly. To validate the effectiveness of the proposed controller, numerical simulations and experiments on a single flexible joint testbed are conducted. The simulation and experimental results show that the control preformation are improved significantly in terms of link vibration, position tracking, and rejection of the kinematic error due to harmonic drive reducers. This chapter is based on an article titled *"A Two-Stage State Feedback Controller Supported by Disturbance-State Observer for Vibration Control of a Flexible-Joint Robot"* published on Robotica (in press), accepted in July 2019.

3.1 Introduction

Serial robots are used in several industrial applications. The control performance is reduced mainly by vibration problems, which are caused by the presence of joint flexibility. Since the joint flexibility induces a distortion between motor and link positions, a single joint becomes a multiple degrees of freedom system with a complex dynamic model. The joint flexibility introduces flexible modes, which may be excited by the reference or disturbances such as external torques, coupling torques, or kinematic error frequencies if harmonic drive reducers are used at robot joints (Gandhi & Ghorbel, 2002; Tonshoff & Kummetz, 1999).

In order to avoid exciting flexible modes, the control bandwidth of flexible joint robots is kept lower than a half the lowest flexible frequency (Craig, 1989). The low control bandwidth, however, may significantly deteriorate the robot control performances in terms of vibration control, motion control, and disturbance rejections. Although many studies on control algorithms for flexible joint robots has been conducted, extending robot control bandwidth while minimizing the effect of kinematic error with experimental validation on flexible joint robots is still open for further research.

3.1.1 Flexible joint robot control background

Most industrial serial robots currently use a decentralized control approach, in which the robot joints are controlled individually using joint-level controllers (Houman Dallali, Lee, Tsagarakis, & Caldwell, 2015). The decentralized approach is based on an idea that that the multiple joint robot dynamic model can be decoupled into multiple single-joint systems. The nonlinear terms and coupling effects are grouped into lumped disturbances (Cong Wang, Zheng, Wang, Peng, & Tomizuka, 2017). These disturbances are considered substantially small and treated independently by joint-level controllers, resulting in stable and good control performance (W. Chen & Tomizuka, 2014). Due to the success of the decentralized control approach, most studies including the study in this chapter focus on a development of joint-level controllers for the decoupled single-joint model.

Several methods for motion control in joint-level of flexible joint robots are well documented in (M.W. Spong, 1990). The first approach is rigid controller, which is still extensively used for recent industrial serial robots. The proportional-integral-derivative (PID) controller for flexible joint robots are studied in (Nanos & Papadopoulos, 2015; Pham & Ahn, 2014). Another approach is singular perturbation control, in which the flexible joint robot dynamics is approximated by a singular perturbation model (Liu & Huang, 2018; Readman & Belanger, 1990a). A problem of the rigid, the PID, and the singular perturbation control algorithms is that they work only when the flexible mode frequencies are very high in comparison with the dominant frequencies of the transient response. In other word, the robot dynamics can be

separated into fast and slow dynamics, which are well separated from each other. However, that frequency separation is not always fulfilled in industrial serial robots. For example, even big serial robots with very high joint stiffness normally carry heavy links and loads, resulting in relatively low flexible mode frequencies. Another reason preventing the extension of the singular perturbation method is that the fluctuation and saturation problems of the control effort, which may damage the test bench (Lessard et al., 2014). The combination of feedback and feedforward control are proposed for flexible joint robots in (Bang, Shim, Park, & Seo, 2010; Losey, Erwin, McDonald, Sergi, & O'Malley, 2016; Yamada et al., 2015). In (Bang et al., 2010), although the control architecture is practical, the feedforward gains are obtained based on a complicated backstepping procedure, making implementation not a trivial matter. The feedforward control approach in (Yamada et al., 2015) provides acceptable motion tracking performance and the closed-loop control bandwidth of about half of the minimum flexible mode frequency. However, the method still requires an experimental validation and more efforts to deal with noises and modeling errors. Another control method for flexible joint robots is iterative learning control, which is discussed thoroughly in (W. Chen & Tomizuka, 2014; Cong Wang et al., 2017; L. Wang, Freeman, & Rogers, 2016; Xu, Chu, & Rogers, 2014). The iterative learning control is suitable for robotic systems performing repetitive tasks under unchanged conditions. The input and the tracking error of the recent iteration are used to construct the input for the next iteration. As a result, the tracking error is decreased proportionally to the iteration number. Another successful control approach for flexible joint robots is feedback linearization, which is discussed in (Nanos & Papadopoulos, 2015). By providing a nonlinear state feedback law, a closed-loop system of flexible joint robots with exactly linear behavior and decoupled dynamics is achieved. However, the feedback linearization may be sensitive to model mismatches since it relies on the exact cancellation of the robot dynamics (Giusti, Malzahn, Tsagarakis, & Althoff, 2017).

Another control method for flexible joint robot is backstepping control, which is also known as two-stage feedback control approach. The two-stage feedback control considers the joint elastic torque or the motor position as an intermediate virtual reference for the link dynamics. When the joint elastic torque is sensed using a torque sensor, the joint elastic torque is

considered as a state variable and is controlled by a torque feedback loop (Lin & Goldenberg, 1995). In (Baspinar, 2011), a two-stage feedback controller is proposed, assuming that the robot links converge to their reference motions if the motors track appropriate trajectories. However, most two-stage feedback controllers have been proven only by numerical simulations in recent studies (Baspinar, 2011; Jong H. Oh & Lee, 1999; Sungha Kwon, 2016). The two-stage feedback control approaches, to the authors' knowledge, has undergone fairly limited testing. This is primarily because of the natural complexity of the flexible joint robot dynamics. For example, although a two-stage feedback control obtains acceptable motion control performance in terms of position tracking error (Uh, Oh, & Lee, 1998), the applied torque on the motor is too noisy. Moreover, complex adaptive schemes proposed by Baspinar may require to deal with uncertainties. The two-stage feedback control approach proposed by (An-Chyau & Yuan-Chih, 2004) was proven to be effective, however, the joint stiffness coefficient selected for simulations was unrealistically low for most recent robotic configurations. Consequently, due to the remaining problems, the recent two-stage feedback controllers developed in the literature cannot be directly applied to actual flexible joint robots. More experimental investigations need to be conducted to validate the performance of the two-stage feedback control approaches. However, despite the practical difficulties mentioned above, the two-stage feedback approach is still very promising since the closed-loop dynamic model is explicit and the control performance can be expressed by analytical solutions.

3.1.2 Need for disturbance-state observer

Most controller mentioned in the previous section are model-based control approaches. The main obstacles that limit the performance of the model-based control algorithms are disturbances and the lack of state measurements. The disturbances may include external torques, kinematic errors, unmodelled joint friction, unmodelled joint stiffness, or parametric uncertainties. A common method to deal with disturbances is disturbance observers. The disturbance observers estimate unknown disturbances in real-time and then cancel them through an appropriate torque feedback loop. General principle of the disturbance observers is presented in (M. Chen & Ge, 2013; Hamelin, Bigras, Beaudry, Richard, & Blain, 2014; S.-K.

Kim, Park, Yoon, & Lee, 2015). Active disturbance rejection control is another approach to compensate disturbances (Han, 2009; Parvathy & Daniel, 2013; Zhao & Guo, 2015). Similarity analysis of disturbance observer and active disturbance rejection control are presented in (Y. Wang, Tian, Dai, Shen, & Jia, 2018). A recent work of using the disturbance observers on flexible link systems is discussed in (Morales, Feliu, & Jaramillo, 2012). Morales introduces a disturbance cancellation to only the outer feedback loop, which is the link side dynamics. In (M. J. Kim & Chung, 2015), a disturbance compensation is presented to the inner loop, which is the motor feedback loop of a flexible joint system. However, a disturbance observer on both link and motor sides of flexible joint robots has not been fully developed.

To deal with the lack of feedback signal, the disturbance observer can be combined with state observer, resulting in a dual disturbance-state observer. Although the disturbance-state observer is successfully implemented on several mechanical systems (W. Chen, Yang, Guo, & Li, 2016; Hamelin, Bigras, Beaudry, Richard, & Blain, 2012; Yang, Chen, Li, Guo, & Yan, 2017), a combination of the disturbance-state observer and the two-stage feedback controllers to enhance motion control of flexible joint robots is still a very open problem.

3.1.3 Purpose and structure of this chapter

As discussed in the previous section, the major problems of the conventional two-stage feedback controller applied to flexible joint robots may include very noisy applied motor torques, the effect of uncertainties, and the lack of experimental validations. In order to deal with these problems, this chapter presents a design concept and an experimental study of a two-stage feedback controller supported by a disturbance-state observer to improve control performance in terms of motion tracking and vibration rejections. The two-stage feedback controller is designed based on a backstepping approach. Especially, partitioned controllers are employed on the motor and link side controllers. To support the two-stage feedback controller, a disturbance observer is added to compensate the unwanted disturbances on both the motor side and link side dynamics. In combination with the disturbance observer, a state observer is implemented to estimate the velocity feedback signals. The state observer aims to achieve the

feedback signals with low noise and without delay. Using the estimated feedback signals from the disturbance-state observer helps to avoid the motor torque noise, which may be induced by the two-stage feedback controller alone.

The proposed approach introduces some interesting properties, which can be summarized as follows. First, although disturbance observers are successfully applied for flexible joint robots in the literature, normally only the disturbances on the motor side dynamics are compensated (M. J. Kim & Chung, 2015; Paine et al., 2015; Yun & Su, 2014). This is due to the fact that most robots have only a motor feedback control loop, which allows only motor torque reference modification. In contrast to these controllers, the proposed controller may estimate the disturbances on both link and motor sides simultaneously, and then feeds the estimated disturbances to a two-stage feedback architecture. Second, the proposed controller is validated experimentally on an actual flexible joint robot. The experimental validation presented in this study is motivated by very successful numerical simulations of the disturbance observer for flexible joint robots shown in (M. J. Kim & Chung, 2015; Yun & Su, 2014). A design procedure of the proposed controller can be considered as a guideline for practically controlling of various industrial serial robots other than the one described in this study.

This chapter is organized as follows. In section 3.2 and 3.3, the flexible joint robot modelling and the rigid control are reviewed. Then, the proposed enhanced two-stage feedback controller is introduced in the section 3.4. In the section 3.5, experimental results are presented to validate the effectiveness and the improvement of the proposed controller. The section 3.6 presents the summary and the contributions of this work.

3.2 Modelling of the flexible joint robot

The dynamic models of the multiple flexible joint robot and the decoupled single flexible joint robot are presented in this section. The complete dynamic model of multiple flexible joint robots can be governed using Lagrange formulation (De Luca & Book, 2008). In the complete multiple joint robot model, the link and motor dynamic equations are not only coupled through

the elastic joint torques but also at the acceleration level (De Luca, 1998). By assuming that the angular velocity of the robots is due only to their own spinning (De Luca & Book, 2008; M. W. Spong, 1987), the complete model reduces to the simplified model as follows:

$$\begin{cases} \mathbf{M}_l(\mathbf{q}_l)\ddot{\mathbf{q}}_l + \mathbf{C}(\mathbf{q}_l, \dot{\mathbf{q}}_l)\dot{\mathbf{q}}_l + \mathbf{B}_l\dot{\mathbf{q}}_l + \mathbf{g}(\mathbf{q}_l) = \mathbf{K}_r\left(\mathbf{N}^{-1}\mathbf{q}_m - \mathbf{q}_l\right) \\ \mathbf{J}_m\ddot{\mathbf{q}}_m + \mathbf{B}_m\dot{\mathbf{q}}_m + \mathbf{B}_f \mathrm{sgn}(\dot{\mathbf{q}}_m) + \mathbf{N}_r^{-1}\mathbf{K}_r\left(\mathbf{N}_r^{-1}\mathbf{q}_m - \mathbf{q}_l\right) = \mathbf{u} \end{cases} \tag{3.1}$$

where $\mathbf{q}_l \in \mathbb{R}^n$ and $\mathbf{q}_m \in \mathbb{R}^n$ are the vectors of link and motor positions, $\mathbf{M}_l(\mathbf{q}_l) \in \mathbb{R}^{n\times n}$ is the matrix of link inertias, $\mathbf{C}(\mathbf{q}_l, \dot{\mathbf{q}}_l) \in \mathbb{R}^n$ is the vector of Coriolis and centrifugal forces, $\mathbf{B}_l \in \mathbb{R}^{n\times n}$ is the diagonal matrix of joint damping coefficients, $\mathbf{g}(\mathbf{q}_l) \in \mathbb{R}^n$ is the vector of gravitational forces, $\mathbf{K} \in \mathbb{R}^{n\times n}$ is the diagonal matrix of joint stiffness, $\mathbf{N}_r \in \mathbb{R}^{n\times n}$ is the diagonal matrix of harmonic drive gear ratio, $\mathbf{J}_m \in \mathbb{R}^{n\times n}$ is the diagonal matrix of motor inertias, $\mathbf{B}_m$ and $\mathbf{B}_f \in \mathbb{R}^{n\times n}$ are diagonal matrices of motor viscous friction coefficients and motor Coulomb friction coefficients, sgn(□) denotes the sign function, and $\mathbf{u} \in \mathbb{R}^n$ is the vector of actuator torques with n is the number of the robot joint.

Applying the decentralized approach to the simplified multiple joint dynamic model in (3.1) yields a single flexible joint robot (SFJ) model, in which the Coriolis and centrifugal forces, the coupling effects, the Coulomb frictions, and the gravitational forces can be grouped into lumped torque disturbances as follows (Bang et al., 2010; Sariyildiz, Chen, & Yu, 2016):

$$J_l\ddot{q}_l + b_l\dot{q}_l + k_r\left(q_l - \frac{1}{N}q_m\right) + d_l = 0 \tag{3.2}$$

$$J_m\ddot{q}_m + b_m\dot{q}_m - \frac{k_r}{N_r}\left(q_l - \frac{1}{N}q_m\right) + d_m = u \tag{3.3}$$

where q_l and q_m are the link and the motor angular displacements, J_m is the motor inertia, J_l is the total link side inertia, b_l is the link side viscous friction coefficient, b_m is the motor

viscous friction coefficient, k_r is the harmonic drive stiffness and N_r is the harmonic drive gear ratio, u is the motor torque, d_l and d_m are the lumped disturbances on the motor side and the link side, respectively. Eq. (3.2) can be called "*link side dynamics*" while Eq. (3.3) can be called "*motor side dynamics*". Figure 3.1 shows a schematic of the single flexible joint robot. Note that bolded letters are used to denote matrices and vectors while plain letters denotes scalars.

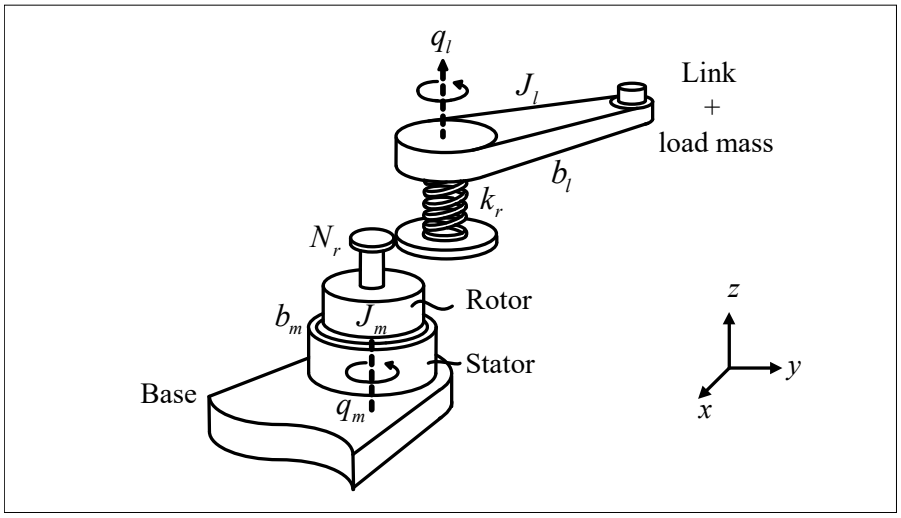

Figure 3.1 The single flexible joint robot schematic diagram

The single flexible joint dynamic model can be expressed using a state-space representation as follows:

$$\dot{\mathbf{x}} = \mathbf{A}\mathbf{x} + \mathbf{B}u + \mathbf{\Gamma}\mathbf{d} \tag{3.4}$$

$$\mathbf{y} = \mathbf{C}\mathbf{x} \tag{3.5}$$

where

$$\mathbf{A} = \begin{bmatrix} 0 & 1 & 0 & 0 \\ -J_l^{-1}k_r & -J_l^{-1}b_l & J_l^{-1}N_r^{-1}k_r & 0 \\ 0 & 0 & 0 & 1 \\ J_m^{-1}N_r^{-1}k_r & 0 & -J_m^{-1}N_r^{-2}k_r & -J_m^{-1}b_m \end{bmatrix} \in \mathbb{R}^{4n\times 4n},$$

$$\mathbf{B} = \begin{bmatrix} 0 & 0 & 0 & J_m^{-1} \end{bmatrix}^T \in \mathbb{R}^{4n},\ \mathbf{\Gamma} = \begin{bmatrix} 0 & -J_l^{-1} & 0 & 0 \\ 0 & 0 & 0 & -J_m^{-1} \end{bmatrix}^T \in \mathbb{R}^{4n\times 2n},$$

$$\mathbf{C} = \begin{bmatrix} 1 & 0 & 0 & 0 \\ 0 & 0 & 1 & 0 \end{bmatrix} \in \mathbb{R}^{2n\times 4n},\ \mathbf{x} = \begin{bmatrix} q_l & \dot{q}_l & q_m & \dot{q}_m \end{bmatrix}^T \in \mathbb{R}^{4n},$$

and $\mathbf{d} = \begin{bmatrix} d_l & d_m \end{bmatrix}^T \in \mathbb{R}^{2n}$, where $n = 1$ for the single flexible joint model.

The transfer functions from the actuator torque u to the motor position q_m and to the link position q_l can be derived from the dynamic equations Eqs. (3.2) and (3.3). By considering only the actuator torque u as the input signal, Eqs. (3.2) and (3.3) can be rearranged as follows:

$$\mathbf{A}_{op}\mathbf{x}_{op} = \mathbf{B}_{op} \tag{3.6}$$

where $\mathbf{A}_{op} = \begin{bmatrix} J_l s^2 + b_l s + k & -\frac{k_r}{N_r} \\ -\frac{k_r}{N_r} & J_m s^2 + b_m s + \frac{k_r}{N_r^2} \end{bmatrix} \in \mathbb{R}^{2\times 2}$, $\mathbf{B}_{op} = \begin{bmatrix} 0 \\ u(s) \end{bmatrix} \in \mathbb{R}^{2}$, and $\mathbf{x}_{op} = \begin{bmatrix} q_l(s) \\ q_m(s) \end{bmatrix} \in \mathbb{R}^{2}$.

The i-th element of the vector $\mathbf{x_{op}}$ of Eq. (3.6) can be obtained using Cramer's Rule as shown in Eq. (3.7).

$$\mathbf{x}_{\mathbf{op}}^{i} = \frac{\det(\mathbf{A}_{op}^{i})}{\det(\mathbf{A}_{op})} \text{ with } i = 1,2 \tag{3.7}$$

where $\mathbf{A}_{op}^{i}$ is the matrix obtained by replacing the i-th column of the matrix $\mathbf{A}_{op}$ by the vector $\mathbf{B}_{op}$.

Substituting $i=1$ and $i=2$ into (3.7) gives the link and motor position $q_l(s)$ and $q_m(s)$ corresponding to the input $u(s)$, as expressed in Eqs. (3.8) and (3.9), respectively.

$$\frac{q_l(s)}{u(s)} = \frac{\det\begin{bmatrix} 0 & -\frac{k_r}{N_r} \\ 1 & J_m s^2 + b_m s + \frac{k_r}{N_r^2} \end{bmatrix}}{\det\begin{bmatrix} J_l s^2 + b_l s + k_r & -\frac{k_r}{N_r} \\ -\frac{k_r}{N_r} & J_m s^2 + b_m s + \frac{k_r}{N_r^2} \end{bmatrix}} \tag{3.8}$$

$$\frac{q_m(s)}{u(s)} = \frac{\det\begin{bmatrix} J_l s^2 + b_l s + k_r & 0 \\ -\frac{k_r}{N_r} & 1 \end{bmatrix}}{\det\begin{bmatrix} J_l s^2 + b_l s + k_r & -\frac{k_r}{N_r} \\ -\frac{k_r}{N_r} & J_m s^2 + b_m s + \frac{k_r}{N_r^2} \end{bmatrix}} \tag{3.9}$$

By simple matrix manipulations of Eqs. (3.8) and (3.9), the transfer functions from the motor torque to the motor and to the link positions are given in Eqs. (3.10) and (3.11), respectively.

$$\frac{q_m(s)}{u(s)} = \frac{J_l s^2 + b_l s + k_r}{J_l J_m s^4 + (J_l b_m + J_m b_l) s^3 + \left(J_l k_r N_r^{-2} + b_m b_l + k_r J_m\right) s^2 + \left(k_r b_m + k_r b_l N_r^{-2}\right) s} \tag{3.10}$$

$$\frac{q_l(s)}{u(s)} = \frac{N_r^{-1} k_r}{J_l J_m s^4 + (J_l b_m + J_m b_l) s^3 + \left(J_l k_r N_r^{-2} + b_m b_l + k_r J_m\right) s^2 + \left(k_r b_m + k_r b_l N_r^{-2}\right) s} \tag{3.11}$$

The frequencies of anti-resonance and resonance can be determined as the frequencies of conjugate zeros and poles of the motor transfer function in Eq. (3.10), respectively. By ignoring the damping, the undamped anti-resonant frequency can be computed by:

$$\omega_z = \sqrt{\frac{k_r}{J_l}} \tag{3.12}$$

and the undamped resonant frequency is:

$$\omega_p = \sqrt{\frac{k_r}{J_l} + \frac{k_r}{J_m N_r^2}} \tag{3.13}$$

These two frequencies ω_z and ω_p are called "flexible mode frequencies", which are discussed in (Zinn, Khatib, Roth, & Salisbury, 2003). The link position can be computed from the motor position following the transfer function shown in Eq. (3.14), which is obtained by dividing Eq. (3.10) by Eq. (3.11). Note that the zeros of transfer function in Eq. (3.11) turns out to be the poles of transfer function in Eq. (3.14), leading to that fact that the anti-resonance frequency on the motor side becomes the oscillation natural frequency of the link (Ellis, 2004).

$$\frac{q_l(s)}{q_m(s)} = \frac{N_r^{-1} k_r}{J_l s^2 + b_l s + k_r} \tag{3.14}$$

The dynamic model of the single flexible joint shown in Eqs. (3.2)-(3.3) and its representations will be used to develop the control algorithm in the next sections.

3.3 Rigid control limitation background

In this section, a review on the rigid controller, the most common used controller for industrial robot, is presented. It is worth emphasizing that the rigid control presented here is only for providing a baseline of current industrial robot control performances.

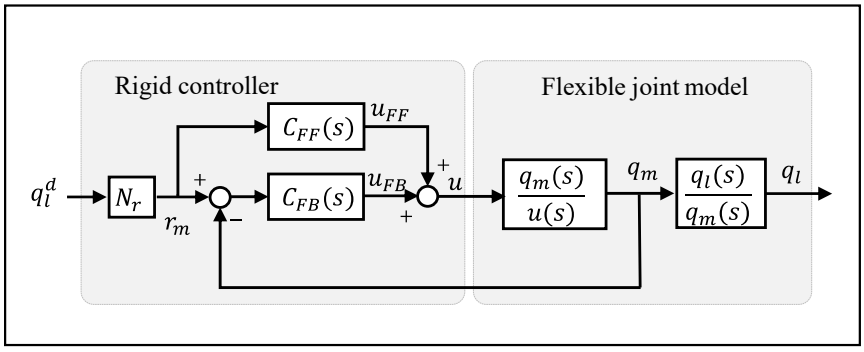

Figure 3.2 Rigid control for the single flexible joint robot

3.3.1 Rigid control design

When designing the rigid control, the joint is assumed to be rigid (Craig, 1989; Lessard et al., 2014). This assumption significantly simplifies the design and analysis of the controller since the complex flexible joint model is regarded as a rigid joint model. Moreover, by ignoring the joint friction, the controller can be even simpler. In fact, the friction compensation, in some flexible joint robot controllers, does not significantly improve the responses. For example, by varying the friction coefficient in the control model, the tracking error changes very little (Lessard et al., 2014).

To give an overview of the rigid control approach, the closed-loop block diagram is shown in Figure 3.2. The rigid control is basically a PID feedback loop with acceleration feedforward control.

By ignoring the joint flexibility, the motor frictions, and the lumped disturbances, the dynamic model of the single flexible joint (shown in Eqs. (3.2) and (3.3)) reduces significantly to:

$$\begin{cases} J_e \ddot{q}_m = u \\ q_l = N^{-1} q_m \end{cases} \tag{3.15}$$

where the term $J_e = J_m + \dfrac{J_l}{N^2}$ is the effective inertia seen from the motor side. The flexible joint dynamics now appears to be very simple, consisting of only a rigid inertia.

The rigid control law is proposed for the reduced model Eq. (3.15) as follows:

$$u = \underbrace{J_e \ddot{r}_m}_{\substack{\text{Feedforward} \\ \text{portion}}} \underbrace{+ K_{p1}\left(\theta_m^d - q_m\right) + K_{d1}\left(\dot{\theta}_m^d - \dot{q}_m\right) + K_{i1}\int_0^t \left(\theta_m^d - q_m\right) dt}_{\text{Feedback portion}} \tag{3.16}$$

where K_{p1}, K_{d1} and K_{i1} are the motor feedback control gains, and r_m is the reference motor position, which is computed as $r_m = N_r q_l^d$.

By taking the Laplace transform of Eq. (3.16), the transfer functions of feedforward and feedback portions in Figure 3.2 are obtained as follows:

$$C_{FF}(s) = J_e s^2 \tag{3.17}$$

$$C_{FB}(s) = \frac{K_{p1} s + K_{d1} s^2 + K_{i1}}{s} \tag{3.18}$$

Substituting Eq. (3.16) into Eq. (3.15) yields the closed-loop motor dynamics in the error space as follows:

$$\ddot{\varepsilon}_m + \frac{K_{d1}}{J_e}\dot{\varepsilon}_m + \frac{K_{p1}}{J_e}\varepsilon_m + \frac{K_{i1}}{J_e}\int_o^t \varepsilon_m dt = 0 \tag{3.19}$$

where $\varepsilon_m = r_m - q_m$ is the motor position tracking error. The feedback gains are defined as follows:

$$K_{p1} = J_e \omega_{n1}^2 \tag{3.20}$$

$$K_{d1} = 2J_e\zeta\omega_{n1} \tag{3.21}$$

$$K_{i1} = J_e\left(\frac{\omega_{n1}}{2\zeta}\right)^3 \tag{3.22}$$

where ζ and ω_{n1} are the damping ratio and the natural frequency of the rigid controller, respectively. In the rigid control scheme, the gain K_{p1} sets the stiffness of the closed-loop system. The integral gain K_{i1} is computed such that the feedback controller Eq. (3.18) has critical damped zeros for a given value of ω_{n1}. The Eq. (3.19) implies that the motor steady state error vanishes with the rigid controller.

3.3.2 Bandwidth limitation

The closed-loop stiffness can be increased by increasing the parameter ω_{n1} in Eqs. (3.20), (3.21), and (3.22), resulting in higher disturbance rejection and faster response. However, too high stiffness leads to an excessive vibration in the link transient responses if the flexible mode frequencies in Eqs. (3.12) and (3.13) are unintentionally excited (Zinn et al., 2003). To avoid exciting these flexible mode frequencies, the parameter ω_{n1} is set to be half of the lowest flexible mode (Craig, 1989), as follows:

$$\omega_{n1} = \frac{1}{2}\omega_z \tag{3.23}$$

with ω_z corresponding to the lowest flexible mode frequency computed using (3.12). To obtain critical damped responses, the damping ratio ζ is set to 1, then, the PID gains can be computed using Eqs. (3.20) , (3.21), and (3.22).

The relationship between ω_{n1} and ω_z in Eq. (3.23) implies that a higher flexible mode frequency ω_z allows boosting the rigid controller natural frequency ω_{n1}, resulting in better performances in terms of disturbance rejection and responsiveness. Intuitively, high flexible mode frequency ω_z is expected. However, since the frequencies of the flexible modes rely on the physical properties of the robot manipulators, they could not be modified without putting so much effort on mechanical designs. Eventually, due to the nature of the open-chain robotic dynamics, variations of robot size and design may not cause significant changes of flexible mode frequencies. Big robot joints with high joint stiffness normally drive large and long links with heavy loads while small robot joints carrying small links but having low joint stiffness. As a result, dynamic behaviors of big and small robots are similar, with the first resonance within a low frequency range about 5 Hz to 25 Hz (Paul, 1981). This low frequency range leads to low control bandwidth of robotic systems using rigid control approach.

3.4 Enhanced two-stage feedback controller

This section presents a control algorithm to improve control performances of flexible joint robots, especially in terms of control bandwidth. The proposed controller entitled enhanced two-stage feedback (ESFB) is a combination of a two-stage feedback controller and a disturbance-state observer. The two-stage feedback considers the actual motor position as an intermediate virtual input for the link side dynamics. The link position may converge to the reference position if the motor position follows an appropriate trajectory. The disturbance-state observer compensates the lumped disturbances on both motor and link sides and estimates the feedback velocities, which are not directly measured. The block diagram of the closed-loop system using the proposed controller is shown in Figure 3.3. In the next sections, two main parts (the two-stage feedback controller and the disturbance-state observer) of the proposed controller are presented.

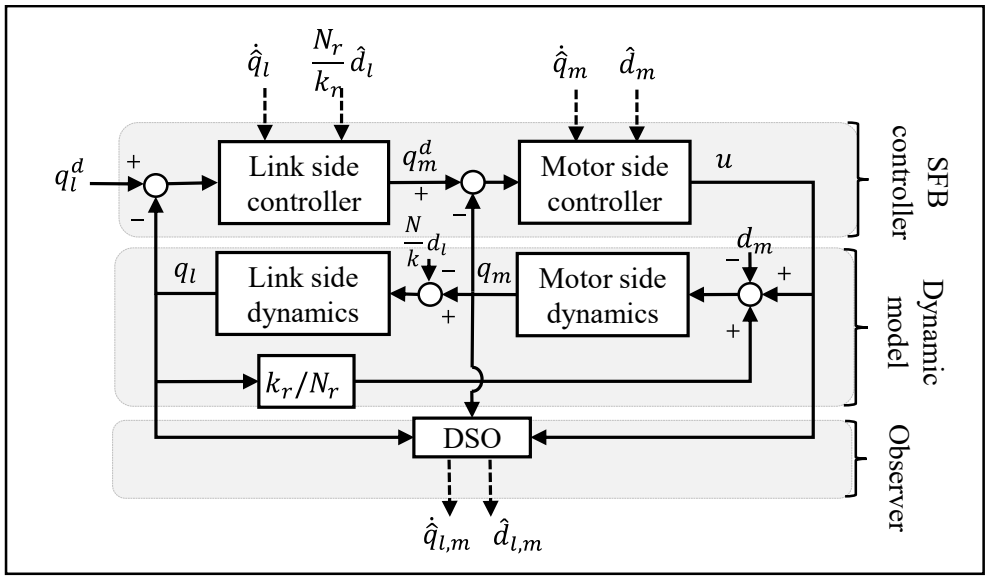

Figure 3.3 Block diagram of the closed-loop system using the proposed controller ESFB. The link side controller shown in (3.31), the motor side controller shown in (3.24), the link side dynamics shown in (3.2) or (3.30), the motor side dynamics shown in (3.3) and the disturbance-state observer shown in (3.37) and (3.40)

3.4.1 Two-stage feedback controller design

First, assuming that an appropriate reference of the motor that leads the link to accurately follow the link reference is known. This motor position reference is denoted as a vector $\mathbf{q}_m^d = \begin{bmatrix} q_m^d & \dot{q}_m^d & \ddot{q}_m^d \end{bmatrix}^T$. A partitioned controller (Craig, 1989) can be employed to control the motor. The partitioned controller is basically a computed torque controller, which can be considered as a special application of the feedback linearization of nonlinear systems. Although feedback linearization may be sensitive to model mismatches and disturbances, the robustness of the partitioned controller can be improved by adding disturbance compensations. Basically, the partitioned control uses an inner feedback loop to reduce the complex motor side dynamics to a $1/s^2$ type system. An outer feedback loop is then employed to place the closed-loop poles at desired locations in the *s*-plane. The partitioned control on the motor side is expressed as follows:

$$u = J_m \alpha + b_m \dot{\hat{q}}_m - \frac{k_r}{N_r}\left(q_l - \frac{1}{N} q_m \right) + \hat{d}_m \tag{3.24}$$

with $$\alpha = \ddot{q}_m^d + K_m^v \left(\dot{q}_m^d - \dot{\hat{q}}_m \right) + K_m^p \left(q_m^d - q_m \right) \tag{3.25}$$

where K_m^p and K_m^v are the feedback control gains, $\hat{d}_m$ and $\dot{\hat{q}}_m$ are the estimated motor side disturbance and the estimated motor velocity, respectively. The last three terms in the right hand side of the Eq. (3.24) are of the inner feedback loop, which cancels out the complex system dynamics. The Eq. (3.25) is the outer feedback loop, which modify the behaviors of the closed-loop system.

Rearranging the Eq. (3.25) using the estimation error of the motor velocity $\dot{\tilde{q}}_m = \dot{q}_m - \dot{\hat{q}}_m$ as follows:

$$\alpha = \ddot{q}_m^d + K_m^v \left(\dot{q}_m^d - \dot{q}_m \right) + K_m^p \left(q_m^d - q_m \right) + K_m^v \dot{\tilde{q}}_m \tag{3.26}$$

Substituting Eq. (3.24) into Eq. (3.3) yields the motor side closed-loop dynamics in error space as follows:

$$\ddot{e}_m + K_m^v \dot{e}_m + K_m^p e_m = \left(\frac{b_m}{J_m} - K_m^v \right) \dot{\tilde{q}}_m + \frac{1}{J_m} \tilde{d}_m \tag{3.27}$$

where $\tilde{d}_m = d_m - \hat{d}_m$ is the estimation error of the motor disturbance and $e_m = q_m^d - q_m$ is the tracking error of the motor position.

If $\tilde{d}_m$ and $\dot{\tilde{q}}_m$ are small, the selection of control gains is pretty simple and is independent of the flexible joint parameters such that

$$K_m^p = \lambda_m^2 \tag{3.28}$$

$$K_m^v = 2\xi_m \lambda_m \tag{3.29}$$

where the parameter λ_m sets the closed-loop stiffness provided by the motor side controller. Eqs. (3.28) and (3.29) implies that the critical damped of the motor position tracking error is preserved by setting $\xi_m = 1$.

In the following, the steps to find the motor reference are presented. The link side dynamics expressed in Eq. (3.2) can be reformulated as:

$$J_l \frac{N_r}{k_r} \ddot{q}_l + \frac{b_l N_r}{k_r} \dot{q}_l + N_r q_l + \frac{N_r}{k_r} d_l = q_m \tag{3.30}$$

According to the link side dynamics in Eq. (3.30), the link position is the output while the motor position is the input signal. The motor reference is defined based on the partitioned control as:

$$q_m^d = J_l \frac{N_r}{k_r} \beta + \frac{b_l N_r}{k_r} \dot{\hat{q}}_l + N_r q_l + \frac{N_r}{k_r} \hat{d}_l \tag{3.31}$$

with

$$\beta = \ddot{q}_l^d + K_l^v \left(\dot{q}_l^d - \dot{\hat{q}}_l \right) + K_l^p \left(q_l^d - q_l \right) \tag{3.32}$$

where K_l^p and K_l^v are the feedback control gains, the parameters $\hat{d}_l$ and $\dot{\hat{q}}_l$ are the estimated disturbances on the link side and the estimated link velocity, respectively. The Eq. (3.31) is considered the link side controller since it derives the input for the link side dynamics.

The first and the second numerical derivative of the motor reference q_m^d are used to implement the motor side controller expressed in Eqs. (3.24) and (3.25). For practical implementations, the typical sampling frequency is one kHz, which is about 50 times faster than the frequency of the first flexible mode of most flexible joint robots (which is normally less than 20 Hz), resulting in fairly small numerical derivation errors.

The Eq. (3.32) is rearranged using the estimation error of the link velocity $\dot{\tilde{q}}_l = \dot{q}_l - \dot{\hat{q}}_l$ as follows:

$$\beta = \ddot{q}_l^d + k_l^v \left(\dot{q}_l^d - \dot{q}_l \right) + k_l^p \left(q_l^d - q_l \right) + k_l^v \dot{\tilde{q}}_l \tag{3.33}$$

Substituting Eq. (3.31) into Eq. (3.30), given that $q_m = q_m^d - e_m$, yields the closed-loop dynamics of the link side in the error space as follows:

$$\ddot{e}_l + K_l^v \dot{e}_l + K_l^p e_l = \left(\frac{b_l}{J_l} - K_l^v \right) \dot{\tilde{q}}_l + \frac{1}{J_l} \tilde{d}_l + \frac{1}{J_l} \frac{k_r}{N_r} e_m \tag{3.34}$$

where $\tilde{d}_l = d_l - \hat{d}_l$ is the estimation error of the link disturbance and $e_l = q_l^d - q_l$ is the tracking error of the link position.

If $\tilde{d}_l$, e_m and $\dot{\tilde{q}}_l$ are small, the feedback control gains of the link side controller can be determined using Eqs. (3.35) and (3.36). Note that the critical damped of the tracking error of the link is obtained by setting $\xi_l = 1$.

$$K_l^p = \lambda_l^2 \tag{3.35}$$

$$K_l^v = 2\xi_l \lambda_l \tag{3.36}$$

where the parameter λ_l sets the closed-loop stiffness provided by the link side controller.

3.4.2 Disturbance-state observer design

A disturbance-state observer is combined with the enhanced two-stage feedback presented in the previous section to improve the robustness. The block diagram of the combination of the disturbance-state observer and the two-stage controller is shown in Figure 3.4. Note that the

diagram in Figure 3.4 can be considered as a simpler view of the proposed controller shown in Figure 3.3. The disturbance-state observer is the integration of a disturbance observer and a state observer. While the disturbance observer subsystem estimates and compensates the disturbances, the state observer subsystem provides the estimations of the angular velocities. Up to now, the applications of the disturbance observers for several systems with flexible elements are presented in the literature of the control theory. However, the motion control performances of disturbance observers combining multiple feedback loop controllers have not been fully understood. In contrast with previous studies, the proposed control approach described in this study presents the disturbance compensation implemented simultaneously in both inner and outer loop of the controller, as shown in Eqs. (3.24) and (3.31).

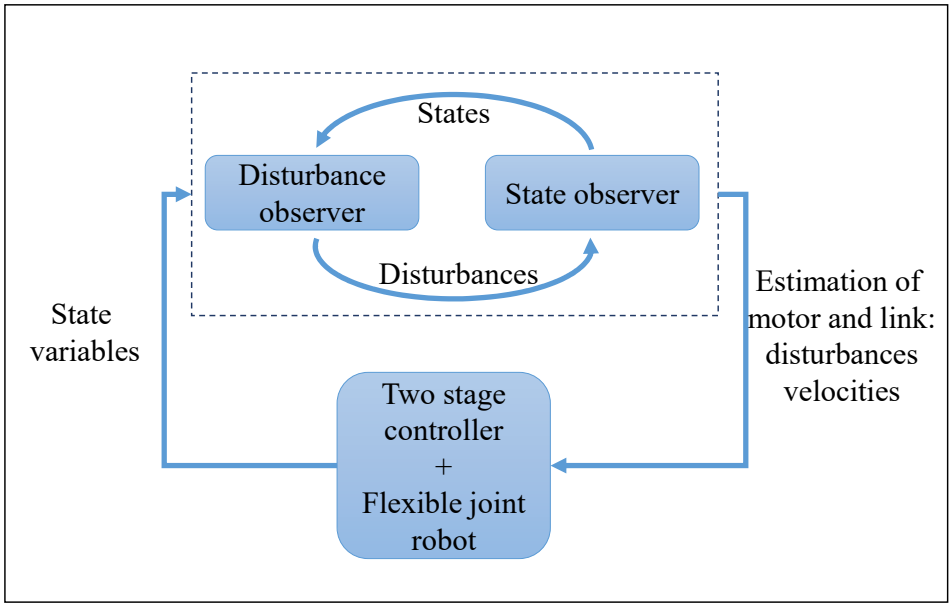

Figure 3.4 Combination of the disturbance-state observer and the two-stage controller

The general form of state observer subsystem of the disturbance-state observer is defined as:

$$\dot{\hat{\mathbf{x}}} = \mathbf{A}\hat{\mathbf{x}} + \mathbf{B}u + \mathbf{L}(\mathbf{y} - \mathbf{C}\hat{\mathbf{x}}) + \mathbf{\Gamma}\hat{\mathbf{d}} \tag{3.37}$$

where $\mathbf{L} \in \mathbb{R}^{4n \times 2n}$ is the matrix of the observer gains, $\mathbf{C} \in \mathbb{R}^{2n \times 4n}$ is the selection matrix that maps the vector of state variables to the vector of the state measurements, $\hat{\mathbf{x}} \in \mathbb{R}^{4n}$ is the vector

of the estimated states, and $\hat{\mathbf{d}} \in \mathbb{R}^{2n}$ is the vector of the estimated disturbances. If only the link and the motor angular positions are directly measured (using embedded encoders), the dimensions of the matrix **L** and the matrix **C** can be determined using $n = 1$.

The lumped disturbances of the flexible joint dynamic model can be derived from Eq. (3.4) as follows:

$$\mathbf{d} = \boldsymbol{\Gamma}^{+}(\dot{\mathbf{x}} - \mathbf{A}\mathbf{x} - \mathbf{B}u) \tag{3.38}$$

where $\boldsymbol{\Gamma}^{+} \in \mathbb{R}^{2n \times 4n}$ is the Moore-Penrose pseudoinverse of $\boldsymbol{\Gamma}$ and it can be determined by the equation $\boldsymbol{\Gamma}^{+} = \left(\boldsymbol{\Gamma}^{\mathrm{T}}\boldsymbol{\Gamma}\right)^{-1}\boldsymbol{\Gamma}^{\mathrm{T}}$.

Note that the implementation of Eq. (3.38) requires a full state feedback, which is unavailable in practice. When the missing feedback states are estimated by the state observer, the equivalent estimated disturbance can be expressed as follows:

$$\mathbf{d}_{eq} = \boldsymbol{\Gamma}^{+}(\dot{\hat{\mathbf{x}}} - \mathbf{A}\hat{\mathbf{x}} - \mathbf{B}u) \tag{3.39}$$

where $\mathbf{d}_{eq} = \begin{bmatrix} d_{eq-l} & d_{eq-m} \end{bmatrix}^{T} \in \mathbb{R}^{2n}$.

Then the disturbance observer subsystem is a combination of the vector of the equivalent estimated disturbance $\mathbf{d}_{eq}$ and low-pass filters as follows:

$$\hat{\mathbf{d}} = \mathbf{Q}\mathbf{d}_{eq} \tag{3.40}$$

where $\mathbf{Q} = \mathrm{diag}\{Q_l, Q_m\}$ is a diagonal matrix, in which the diagonal elements are low-pass filtering linear operators. Q_l and Q_m are the low-pass filters on the link side and the motor side, respectively. Since a systematic way to determine the type and structure for the low-pass filter of Eq. (3.40) is not fully developed in previous literatures, it is still unclear which design technique should be taken. However, based on a successfully implemented in several

researches (Hamelin et al., 2014; Hamelin et al., 2012; Yan & Shiu, 2008), a third-order binominal filter is a promising approach and is used in this study.

The state-space representation of the low-pass filters Q_l and Q_m are given in Eqs. (3.41) to (3.44), respectively.

$$\dot{\hat{\boldsymbol{\eta}}}_l = \mathbf{F}_l \hat{\boldsymbol{\eta}}_l + \mathbf{G}_l d_{eq-l} \tag{3.41}$$

$$\hat{d}_l = \mathbf{H}_l \hat{\boldsymbol{\eta}}_l \tag{3.42}$$

and

$$\dot{\hat{\boldsymbol{\eta}}}_m = \mathbf{F}_m \hat{\boldsymbol{\eta}}_m + \mathbf{G}_m d_{eq-m} \tag{3.43}$$

$$\hat{d}_m = \mathbf{H}_m \hat{\boldsymbol{\eta}}_m \tag{3.44}$$

Combining Eqs. (3.41), (3.42), (3.43), and (3.44) yields the low-pass filter $\mathbf{Q}$ in state-space representation as follows:

$$\underbrace{\begin{bmatrix} \dot{\hat{\boldsymbol{\eta}}}_l \\ \dot{\hat{\boldsymbol{\eta}}}_m \end{bmatrix}}_{\dot{\hat{\boldsymbol{\eta}}} \in \mathbb{R}^{(r_l+r_m)}} = \underbrace{\begin{bmatrix} \mathbf{F}_l & \mathbf{0} \\ \mathbf{0} & \mathbf{F}_m \end{bmatrix}}_{\mathbf{F} \in \mathbb{R}^{(r_l+r_m)\times(r_l+r_m)}} \underbrace{\begin{bmatrix} \hat{\boldsymbol{\eta}}_l \\ \hat{\boldsymbol{\eta}}_m \end{bmatrix}}_{\hat{\boldsymbol{\eta}} \in \mathbb{R}^{(r_l+r_m)}} + \underbrace{\begin{bmatrix} \mathbf{G}_l & \mathbf{0} \\ \mathbf{0} & \mathbf{G}_m \end{bmatrix}}_{\mathbf{G} \in \mathbb{R}^{(r_l+r_m)\times 2n}} \underbrace{\begin{bmatrix} d_{eq-l} \\ d_{eq-m} \end{bmatrix}}_{\mathbf{d}_{eq} \in \mathbb{R}^{2n}} \tag{3.45}$$

$$\underbrace{\begin{bmatrix} \hat{d}_l \\ \hat{d}_m \end{bmatrix}}_{\hat{\mathbf{d}} \in \mathbb{R}^{2n}} = \underbrace{\begin{bmatrix} \mathbf{H}_l & \mathbf{0} \\ \mathbf{0} & \mathbf{H}_m \end{bmatrix}}_{\mathbf{H} \in \mathbb{R}^{2n\times(r_l+r_m)}} \begin{bmatrix} \hat{\boldsymbol{\eta}}_l \\ \hat{\boldsymbol{\eta}}_m \end{bmatrix} \tag{3.46}$$

where $\hat{\boldsymbol{\eta}} = \begin{bmatrix} \hat{\boldsymbol{\eta}}_l & \hat{\boldsymbol{\eta}}_m \end{bmatrix}^T \in \mathbb{R}^{(r_l+r_m)}$ presents the vector of filter states, r_l and r_m are the order of the filter Q_l and Q_m, respectively, $\mathbf{F} = \operatorname{diag}\left\{\mathbf{F}_l \in \mathbb{R}^{r_l\times r_l}, \mathbf{F}_m \in \mathbb{R}^{r_m\times r_m}\right\} \in \mathbb{R}^{(r_l+r_m)\times(r_l+r_m)}$, $\mathbf{G} = \operatorname{diag}\left\{\mathbf{G}_l \in \mathbb{R}^{r_l}, \mathbf{G}_m \in \mathbb{R}^{r_m}\right\} \in \mathbb{R}^{(r_l+r_m)\times 2n}$, and $\mathbf{H} = \operatorname{diag}\left\{\mathbf{H}_l \in \mathbb{R}^{r_l}, \mathbf{H}_m \in \mathbb{R}^{r_m}\right\} \in \mathbb{R}^{2n\times(r_l+r_m)}$ are block diagonal matrices of the state-space representation. Note that all elements of the matrices **F**, **G**, and **H** are determined from the link side low-pass filter $Q_l(s) = \mathbf{H}_l \left(s\mathbf{I} - \mathbf{F}_l\right)^{-1} \mathbf{G}_l$ and

motor side low-pass filter $Q_m(s) = \mathbf{H}_m \left(s\mathbf{I} - \mathbf{F}_m \right)^{-1} \mathbf{G}_m$, and s is the Laplace complex variable.

The filter state error is derived from Eq. (3.40) as:

$$\tilde{\boldsymbol{\eta}} = \left(\mathbf{Q}(s) - \mathbf{I}_{2n} \right) \mathbf{d}_{eq} \tag{3.47}$$

where $\mathbf{I}_{2n} \in \mathbb{R}^{2n \times 2n}$ is a unity matrix and the filter state error $\tilde{\boldsymbol{\eta}} \in \mathbb{R}^{(r_l + r_m)}$ is computed by $\tilde{\boldsymbol{\eta}} = \boldsymbol{\eta} - \hat{\boldsymbol{\eta}}$.

Combining Eqs. (3.37), (3.4), and (3.46) yields the state estimation error as follows:

$$\dot{\tilde{\mathbf{x}}} = \left(\mathbf{A} - \mathbf{LC} \right) \tilde{\mathbf{x}} + \boldsymbol{\Gamma} \mathbf{H} \tilde{\boldsymbol{\eta}} \tag{3.48}$$

where $\tilde{\mathbf{x}} \in \mathbb{R}^{4n}$ is computed by $\tilde{\mathbf{x}} = \mathbf{x} - \hat{\mathbf{x}}$, $\tilde{\boldsymbol{\eta}}$ is computed from Eq. (3.47), and $\mathbf{H}$ is from Eq. (3.46).

The disturbance estimation errors are derived as follows:

$$\tilde{\mathbf{d}} = \boldsymbol{\delta}_1 + \boldsymbol{\delta}_2 \tag{3.49}$$

where $\boldsymbol{\delta}_1 = \left(\mathbf{d} - \mathbf{d}_{\mathbf{eq}} \right) \in \mathbb{R}^{2n}$ and $\boldsymbol{\delta}_2 = \left(\mathbf{d}_{\mathbf{eq}} - \hat{\mathbf{d}} \right) \in \mathbb{R}^{2n}$. Combining Eqs. (3.38), (3.39), and (3.48) yields:

$$\boldsymbol{\delta}_1 = -\boldsymbol{\Gamma}^{+} \mathbf{LC} \tilde{\mathbf{x}} + \mathbf{H} \tilde{\boldsymbol{\eta}} \tag{3.50}$$

In addition, $\boldsymbol{\delta}_2$ also may be derived from Eq. (3.46) as:

$$\boldsymbol{\delta}_2 = \mathbf{H} \tilde{\boldsymbol{\eta}} \tag{3.51}$$

Substituting Eqs. (3.50) and (3.51) into Eq. (3.49) yields:

$$\tilde{\mathbf{d}} = -\boldsymbol{\Gamma}^{+}\mathbf{LC}\tilde{\mathbf{x}} + 2\mathbf{H}\tilde{\boldsymbol{\eta}} \tag{3.52}$$

The disturbance estimation on the motor side and on the link side can be obtained from Eq. (3.52) as:

$$\tilde{d}_l = -\mathbf{S}_l\boldsymbol{\Gamma}^{+}\mathbf{LC}\tilde{\mathbf{x}} + 2\mathbf{H}_l\tilde{\boldsymbol{\eta}}_l \tag{3.53}$$

$$\tilde{d}_m = -\mathbf{S}_m\boldsymbol{\Gamma}^{+}\mathbf{LC}\tilde{\mathbf{x}} + 2\mathbf{H}_m\tilde{\boldsymbol{\eta}}_m \tag{3.54}$$

where $\mathbf{S}_l = \begin{bmatrix} 1 \\ 0 \end{bmatrix}^T \in \mathbb{R}^{2n}$, and $\mathbf{S}_m = \begin{bmatrix} 0 \\ 1 \end{bmatrix}^T \in \mathbb{R}^{2n}$.

The state estimation error expressed in Eq. (3.48) and the disturbance estimation error expressed in Eq. (3.52) are used to conduct the stability analysis presented in the next sections. Note that the architecture of the disturbance observer shown in Eq. (3.40) is used in this study since its effectiveness in practical applications is validated in our previous works (Hamelin et al., 2012). Although the disturbance observer is designed based on the linear dynamics only, it still works effectively in the presence of nonlinear behaviors, as shown in (M. J. Kim & Chung, 2015). For further studies on different types of disturbance observers, the interested readers are invited to follow some other design approaches discussed in (Mohammadi, Tavakoli, Marquez, & Hashemzadeh, 2013; Yun & Su, 2014). It is worth mentioning that, in order to improve the disturbance compensation, the variations of the link side inertia and the gravitational forces when the robot configuration changes can be computed and updated in real-time to the controller, as presented in (Alessandro De Luca et al., 2005).

3.4.3 Steady-state error analysis

By taking the Laplace transform of Eqs. (3.27) and (3.34), the tracking errors of the motor and the link positions are expressed in Eqs. (3.55) and (3.56), respectively.

$$e_m = \frac{1}{J_m\left(s^2 + K_m^v s + K_m^p\right)}\tilde{d}_m + \left(\frac{b_m}{J_m} - K_m^v\right)\frac{1}{\left(s^2 + K_m^v s + K_m^p\right)}\dot{\tilde{q}}_m \tag{3.55}$$

$$e_l = \frac{1}{J_l}\frac{k_r}{N_r\left(s^2 + K_l^v s + K_l^p\right)}e_m + \frac{1}{J_l\left(s^2 + K_l^v s + K_l^p\right)}\tilde{d}_l + \left(\frac{b_l}{J_l} - K_l^v\right)\frac{1}{\left(s^2 + K_l^v s + K_l^p\right)}\dot{\tilde{q}}_l \tag{3.56}$$

Substituting Eq. (3.55) into Eq. (3.56) yields the tracking error of the link position as a function of the disturbances and the state estimation errors as follows:

$$\begin{aligned} e_l = {} & \frac{1}{J_l\left(s^2 + K_l^v s + K_l^p\right)}\tilde{d}_l + \frac{1}{J_l}\frac{k_r}{N_r J_m\left(s^2 + K_l^v s + K_l^p\right)\left(s^2 + K_m^v s + K_m^p\right)}\tilde{d}_m \\ & + \frac{\left(\frac{b_l}{J_l} - K_l^v\right)}{\left(s^2 + K_l^v s + K_l^p\right)}\dot{\tilde{q}}_l + \frac{1}{J_l}\frac{k_r\left(\frac{b_m}{J_m} - K_m^v\right)}{N_r\left(s^2 + K_l^v s + K_l^p\right)\left(s^2 + K_m^v s + K_m^p\right)}\dot{\tilde{q}}_m \end{aligned} \tag{3.57}$$

Assuming the estimation errors of the disturbances ($\tilde{d}_l$ and $\tilde{d}_m$) vary slowly, the tracking error of the link position after all transients have decayed can be obtained by applying the final value theorem (Franklin, Powell, & Emami-Naeini, 2010) to Eq. (3.57) as follows:

$$\begin{aligned} e_l(\infty) = {} & \lim_{s\to 0} s\frac{\tilde{d}_l(\infty)}{s}\frac{1}{J_l\left(s^2 + K_l^v s + K_l^p\right)} + \lim_{s\to 0} s\frac{\tilde{d}_m(\infty)}{s}\frac{1}{J_l}\frac{k_r}{N_r J_m\left(s^2 + K_l^v s + K_l^p\right)\left(s^2 + K_m^v s + K_m^p\right)} \\ & + \lim_{s\to 0} s\frac{\dot{\tilde{q}}_l(\infty)}{s}\frac{\left(\frac{b_l}{J_l} - K_l^v\right)}{\left(s^2 + K_l^v s + K_l^p\right)} + \lim_{s\to 0} s\frac{\dot{\tilde{q}}_m(\infty)}{s}\frac{1}{J_l}\frac{k_r\left(\frac{b_m}{J_m} - K_m^v\right)}{N_r\left(s^2 + K_l^v s + K_l^p\right)\left(s^2 + K_m^v s + K_m^p\right)} \\ = {} & \frac{1}{J_l K_l^p}\tilde{d}_l(\infty) + \frac{k_r}{J_l K_l^p N_r}\frac{\tilde{d}_m(\infty)}{J_m K_m^p} + \left(\frac{b_l}{J_l} - K_l^v\right)\frac{\dot{\tilde{q}}_l(\infty)}{K_l^p} + \frac{k_r}{J_l K_l^p N_r}\left(\frac{b_m}{J_m} - K_m^v\right)\frac{\dot{\tilde{q}}_m(\infty)}{K_m^p} \end{aligned} \tag{3.58}$$

Note that (∞) indicates the steady-state at time $t = \infty$. The Eq. (3.58) implies that the tracking error of the link position at $t = \infty$ becomes very small when the disturbance errors ($\tilde{d}_l(\infty)$ and

$\tilde{d}_m(\infty)$) and the velocities estimation errors ($\dot{\tilde{q}}_l(\infty)$ and $\dot{\tilde{q}}_m(\infty)$) are small, and the proportional feedback control gains (K_l^p and K_m^p) are high (Franklin et al., 2010).

3.4.4 Closed-loop control bandwidth analysis

The transfer function from the disturbance estimation error to the state estimation error is derived from Eq. (3.48) as follows (Franklin et al., 2010; G. F. Franklin, J. David Powell, & Workman, 1997):

$$\underbrace{\boldsymbol{\Psi}(s)}_{\in \mathbb{R}^{4n\times 2n}} = \frac{\tilde{\mathbf{x}}}{\tilde{\boldsymbol{\eta}}} = \left[s\mathbf{I}_{4n} - (\mathbf{A}-\mathbf{LC})\right]^{-1}\boldsymbol{\Gamma}\mathbf{H} \tag{3.59}$$

where $\mathbf{I}_{4n} \in \mathbb{R}^{4n\times 4n}$ is a unity matrix.

Then, the tracking error of the link position as a function of the disturbances and the state estimation errors expressed in Eq. (3.57) can be rewritten as follows:

$$e_l = \Delta_1\tilde{\mathbf{d}} + \Delta_2\mathbf{C}_e\tilde{\mathbf{x}} \tag{3.60}$$

where, $\Delta_1 = \begin{bmatrix} \dfrac{1}{J_l\left(s^2 + K_l^v s + K_l^p\right)} & \dfrac{1}{J_l}\dfrac{k_r}{N_r J_m\left(s^2 + K_l^v s + K_l^p\right)\left(s^2 + K_m^v s + K_m^p\right)} \end{bmatrix} \in \mathbb{R}^{2n}$,

$$\Delta_2 = \begin{bmatrix} \dfrac{\left(\dfrac{b_l}{J_l} - K_l^v\right)}{\left(s^2 + K_l^v s + K_l^p\right)} & \dfrac{1}{I}\dfrac{k\left(\dfrac{b_m}{J_m} - K_m^v\right)}{N\left(s^2 + K_l^v s + K_l^p\right)\left(s^2 + K_m^v s + K_m^p\right)} \end{bmatrix} \in \mathbb{R}^{2n},$$

and $\mathbf{C}_e = \begin{bmatrix} 0 & 1 & 0 & 0 \\ 0 & 0 & 0 & 1 \end{bmatrix} \in \mathbb{R}^{2n\times 4n}$.

Using the link position tracking error expressed as $e_l = q_l^d - q_l$, the Eq. (3.60) can be rewritten

as:

$$q_l = q_l^d - \Delta_1 \tilde{\mathbf{d}} - \Delta_2 \mathbf{C}_e \tilde{\mathbf{x}} \tag{3.61}$$

Substituting Eq. (3.52) into Eq. (3.61) yields:

$$q_l = q_l^d - 2\Delta_1 \mathbf{H}\tilde{\boldsymbol{\eta}} - \left(\Delta_2 \mathbf{C}_e - \Delta_1 \boldsymbol{\Gamma}^{+}\mathbf{L}\mathbf{C}\right)\tilde{\mathbf{x}} \tag{3.62}$$

Substituting Eq. (3.59) into Eq. (3.62) gives:

$$q_l = q_l^d - \left[2\Delta_1 \mathbf{H} + \left(\Delta_2 \mathbf{C}_e - \Delta_1 \boldsymbol{\Gamma}^{+}\mathbf{L}\mathbf{C}\right)\boldsymbol{\Psi}(s)\right]\tilde{\boldsymbol{\eta}} \tag{3.63}$$

Then, substituting Eq. (3.47) into Eq. (3.63) gives to the following result:

$$q_l = q_l^d - \left[2\Delta_1 \mathbf{H} + \left(\Delta_2 \mathbf{C}_e - \Delta_1 \boldsymbol{\Gamma}^{+}\mathbf{L}\mathbf{C}\right)\boldsymbol{\Psi}(s)\right]\left(\mathbf{I}_{2n} - \mathbf{Q}(s)\right)\mathbf{d}_{eq} \tag{3.64}$$

It can be seen from Eq. (3.64) that the link position tracking error relies on the performance of the low-pass filter $\mathbf{Q}(s)$, of which the attenuation rate varies with regarding to the operation frequencies. In the frequency range such that $\mathbf{Q}(s) \approx \mathbf{I}_{2n}$ (where $\mathbf{I}_{2n}$ is an unity matrix), the Eq. (3.64) gives $q_l \approx q_l^d$. In these frequencies, the disturbance observer completely compensates for the disturbances and the model mismatches, leading to a perfect position tracking performance. Note that if there is no disturbance applied on the flexible joint model, i.e. $\mathbf{d}_{eq} = 0$, a perfect position tracking is also obtained in all frequencies, leading to an infinity control bandwidth.

In the frequency range such that $\mathbf{Q}(s) \approx \mathbf{0}$, the disturbance observer loop is completely disable, resulting in a degradation of the position tracking performance. When the disturbances are large, the lowest bandwidth of $\mathbf{Q}(s)$ can be used to determine the closed-loop control bandwidth. The higher the bandwidth of $\mathbf{Q}(s)$, the higher the closed-loop control bandwidth

achieved.

The bandwidth of the low-pass filter $\mathbf{Q}(s)$ is determined by its cut-off frequencies. It is normally no problem to increase the cut-off frequencies of $\mathbf{Q}(s)$ over the frequency of the link oscillation (ω_z). This is because the cut-off frequencies of $\mathbf{Q}(s)$ are restricted only by the sensor noises and the modelling errors, which normally dominate at high operation frequencies (Yun & Su, 2014). Considering the closed-loop control bandwidth provided by the rigid controller, which is half of the frequency of the link oscillation, the control bandwidth using the proposed controller can be significantly higher. The bandwidth improvement is verified using both numerical simulations and experiments in the next sections.

3.4.5 Closed-loop system stability analysis

By combining Eqs. (3.27) and (3.34), the closed-loop position tracking error can be expressed as:

$$\left[\dot{\boldsymbol{\xi}}\right]_{4n} = \underbrace{\begin{bmatrix}\mathbf{A}_c & \mathbf{Z}_c & \mathbf{H}_c\end{bmatrix}}_{\in \mathbb{R}^{4n\times(8n+\eta+r_m)}} \underbrace{\begin{bmatrix}\boldsymbol{\xi}\\ \tilde{\mathbf{x}}\\ \tilde{\boldsymbol{\eta}}\end{bmatrix}}_{\in \mathbb{R}^{8n+\eta+r_m}} \tag{3.65}$$

where $\boldsymbol{\xi} = \begin{bmatrix} e_l & \dot{e}_l & e_m & \dot{e}_m \end{bmatrix}^T \in \mathbb{R}^{4n}$ is the vector of the link and motor position tracking. Note that $n = 1$ for the single flexible joint model. The matrices $\mathbf{A}_c$, $\mathbf{Z}_c$, and $\mathbf{H}_c$ are given as follows:

$$\mathbf{A}_c = \begin{bmatrix} 0 & 1 & 0 & 0 \\ -K_l^p & -K_l^v & k_r J_l^{-1} N_r^{-1} & 0 \\ 0 & 0 & 0 & 1 \\ 0 & 0 & -K_m^p & -K_m^v \end{bmatrix} \in \mathbb{R}^{4n\times 4n},\ \mathbf{H}_c = \begin{bmatrix} \mathbf{0} & \mathbf{0} \\ 2J_l^{-1}\mathbf{H}_l & \mathbf{0} \\ \mathbf{0} & \mathbf{0} \\ \mathbf{0} & 2J_m^{-1}\mathbf{H}_m \end{bmatrix} \in \mathbb{R}^{4n\times(r_l+r_m)},$$

$$\mathbf{Z}_c = \mathbf{Z}_{c1} + \mathbf{Z}_{c2} \text{ with } \mathbf{Z}_{c1} = \begin{bmatrix} 0 & 0 & 0 & 0 \\ 0 & \left[b_l J_l^{-1} - K_l^v \right] & 0 & 0 \\ 0 & 0 & 0 & 0 \\ 0 & 0 & 0 & \left[b_m J_m^{-1} - K_m^v \right] \end{bmatrix} \in \mathbb{R}^{4n \times 4n} \text{ and}$$

$$\mathbf{Z}_{c2} = \begin{bmatrix} \mathbf{0} \\ -J_l^{-1} \mathbf{S}_l \boldsymbol{\Gamma}^+ \mathbf{L}\mathbf{C} \\ \mathbf{0} \\ -J_m^{-1} \mathbf{S}_m \boldsymbol{\Gamma}^+ \mathbf{L}\mathbf{C} \end{bmatrix} \in \mathbb{R}^{4n \times 4n}.$$

The Eq. (3.37) can be rearranged to achieve the following relationship:

$$\dot{\hat{\mathbf{x}}} - \mathbf{A}\hat{\mathbf{x}} - \mathbf{B}u = \mathbf{L}\mathbf{C}\tilde{\mathbf{x}} + \boldsymbol{\Gamma}\hat{\mathbf{d}} \tag{3.66}$$

Substituting Eq. (3.66) and the second equation of Eq. (3.45) into Eq. (3.39) yields the following relationship:

$$\mathbf{d}_{eq} = \boldsymbol{\Gamma}^+ (\mathbf{L}\mathbf{C}\tilde{\mathbf{x}} + \boldsymbol{\Gamma}\mathbf{H}\hat{\boldsymbol{\eta}}) \tag{3.67}$$

Substituting Eq. (3.67) into the first equation of Eq. (3.45) yields:

$$\begin{aligned} \dot{\hat{\boldsymbol{\eta}}} &= \mathbf{F}\hat{\boldsymbol{\eta}} + \mathbf{G}\boldsymbol{\Gamma}^+ (\mathbf{L}\mathbf{C}\tilde{\mathbf{x}} + \boldsymbol{\Gamma}\mathbf{H}\hat{\boldsymbol{\eta}}) \\ &= (\mathbf{F} + \mathbf{G}\mathbf{H})\hat{\boldsymbol{\eta}} + \mathbf{G}\boldsymbol{\Gamma}^+ \mathbf{L}\mathbf{C}\tilde{\mathbf{x}} \end{aligned} \tag{3.68}$$

Since $\tilde{\boldsymbol{\eta}} = \boldsymbol{\eta} - \hat{\boldsymbol{\eta}}$ then $\dot{\tilde{\boldsymbol{\eta}}} = \dot{\boldsymbol{\eta}} - \dot{\hat{\boldsymbol{\eta}}}$. Substituting Eq. (3.68) into the relation $\dot{\tilde{\boldsymbol{\eta}}} = \dot{\boldsymbol{\eta}} - \dot{\hat{\boldsymbol{\eta}}}$ yields:

$$\begin{aligned} \dot{\tilde{\boldsymbol{\eta}}} &= \dot{\boldsymbol{\eta}} - (\mathbf{F} + \mathbf{G}\mathbf{H})\hat{\boldsymbol{\eta}} - \mathbf{G}\boldsymbol{\Gamma}^+ \mathbf{L}\mathbf{C}\tilde{\mathbf{x}} \\ &= (\mathbf{F} + \mathbf{G}\mathbf{H})\tilde{\boldsymbol{\eta}} - \mathbf{G}\boldsymbol{\Gamma}^+ \mathbf{L}\mathbf{C}\tilde{\mathbf{x}} + \dot{\boldsymbol{\eta}} - (\mathbf{F} + \mathbf{G}\mathbf{H})\boldsymbol{\eta} \end{aligned} \tag{3.69}$$

By combining Eqs. (3.48), (3.65) and (3.69), the closed-loop dynamics using the proposed control can be expressed as follows:

$$\underbrace{\begin{bmatrix}\dot{\boldsymbol{\xi}}\\ \dot{\tilde{\mathbf{x}}}\\ \dot{\tilde{\boldsymbol{\eta}}}\end{bmatrix}}_{\in\mathbb{R}^{8n+\eta+r_m}} = \underbrace{\begin{bmatrix}\left[\mathbf{A}_c\right]_{4n\times 4n} & \left[\mathbf{Z}_c\right]_{4n\times 4n} & \left[\mathbf{H}_c\right]_{4n\times(r_l+r_m)}\\ \begin{bmatrix}\mathbf{0}\\ \mathbf{0}\end{bmatrix}_{(4n+r_l+r_m)\times 4n} & \underbrace{\begin{bmatrix}\mathbf{A}-\mathbf{LC} & \boldsymbol{\Gamma}\mathbf{H}\\ -\mathbf{G}\boldsymbol{\Gamma}^{+}\mathbf{LC} & \mathbf{F}+\mathbf{GH}\end{bmatrix}}_{\mathbf{A}_o\in\mathbb{R}^{(4n+\eta+r_m)\times(4n+\eta+r_m)}}\end{bmatrix}}_{\mathbf{A}_{cl}\in\mathbb{R}^{(8n+\eta+r_m)\times(8n+\eta+r_m)}}\begin{bmatrix}\boldsymbol{\xi}\\ \tilde{\mathbf{x}}\\ \tilde{\boldsymbol{\eta}}\end{bmatrix} + \underbrace{\begin{bmatrix}\mathbf{0}\\ \mathbf{0}\\ \dot{\boldsymbol{\eta}}-(\mathbf{F}+\mathbf{GH})\boldsymbol{\eta}\end{bmatrix}}_{\in\mathbb{R}^{8n+\eta+r_m}} \quad (3.70)$$

The matrix $\mathbf{A}_o$ are related to the stability of the disturbance-state observer while the matrix $\mathbf{A}_{cl}$ determines the stability of the whole closed-loop system. Since the low-pass filter $\mathbf{Q}(s)$ with cut-off frequencies tends toward zero, the matrices **H** and **G** tend to zero (Hamelin et al., 2012). Thus, the matrix $\mathbf{A}_o$ in Eq. (3.70) becomes block diagonal, resulting in decoupling of the eigenvalues of the disturbance observer and the state observer. An important observation is that $\mathbf{A}_{cl}$ is a block triangular matrix, thus the eigenvalues of the feedback controller are also decoupled from the eigenvalues of the disturbance-state observer (Hamelin et al., 2014; Hamelin et al., 2012), i.e. $\lambda_e\{\mathbf{A}_{cl}\} = \lambda_e\{\mathbf{A}_c\} \cup \lambda_e\{\mathbf{A}_o\}$. Due to the decoupled eigenvalues, the two-stage feedback controller and the disturbance-state observer can be designed independently. To guarantee the stable closed-loop, the stable eigenvalues of $\mathbf{A}_c$ and $\mathbf{A}_o$ are expected. The parameter of the matrix **L** of the state observer is determined by placing all poles of **(A–LC)** in the left haft of the *s*-plane.

3.4.6 Controller synthesis procedure

This section presents a procedure to determine the gains of the proposed controller. As discussed, due to the decoupled eigenvalues, the two-stage feedback controller and the disturbance-state observer can be designed independently. The controller design procedure is proposed as follows:

1. Assuming that the robot system is not subjected to disturbances and a full state feedback is available, determine of the value of λ_l and λ_m such that the matrix $\mathbf{A}_c$ satisfies the Routh-Hurwitz criterion. The highest possible values of λ_l and λ_m provide low position

tracking errors and minimize the link vibration while avoiding actuator torque saturation.

2. Set $\mathbf{Q}(s)$ to zero and then design the state observer by calculating matrix **L** of the state observer using the eigenvalue assignment of **(A–LC)**.

3. Increase the cut-off frequencies of the low-pass filter $\mathbf{Q}(s)$ from zero as long as the $\mathbf{A}_o$ is still stable and the desired performance is achieved.

3.5 Experiments

In this section, experiments are performed to validate the effectiveness of the proposed control approach.

3.5.1 Experiment setup

The experiments in this study is conducted using a single flexible joint test bench. The architecture of the joint is built following the design of the serial industrial robot entitled SCOMPI developed at Hydro-Quebec's Research Institute (see Figure 3.5). The test bench consists of a flexible joint, a rigid link, an additional load mass, an embedded current driver, and a control PC system. The joint uses a harmonic drive reducer (CSG-20 with a 160:1 gear ratio). The total moment induced by the link and the load are restricted such that it does not surpass the average torque limit of the harmonic drive reducer. The motor position is measured by a 13-bit resolution custom Timken magnetic encoder while the link position is measured by an 18-bit Netzer DS-58 absolute encoder.

The actuator is a synchronous permanent magnets frameless motor with the limitations of the continuous and the peak torque being respectively 0.53 Nm and 1.05 Nm. The control algorithm is realized using C++ language and executes on a control PC running a real-time Linux operating system. The sampling frequency is 1 kHz. The control PC communicates with the embedded current driver through the EtherCAT protocol.

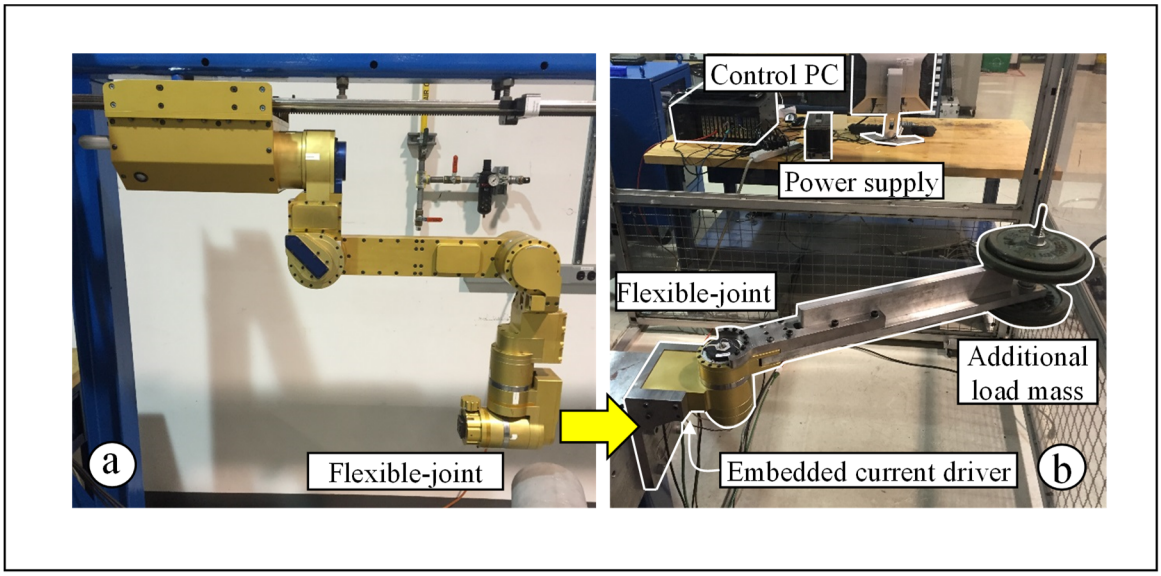

Figure 3.5 (a) The six-joint SCOMPI robot, (b) The single flexible joint test bench to test a flexible joint of the SCOMPI robot

The discrete controllers are used for experiments. For simplicity, the discrete controllers are obtained by discretizing the continuous controllers described in the previous sections using the backward difference method. Since the sampling frequency is fairly fast (1 kHz, which is about 50 times faster than the vibration frequency of most industrial flexible joint robots (normally less than 20 Hz)), control performances obtained by the discrete controllers may differ very little from that of the continuous controllers.

3.5.2 Identification of the single flexible joint robot

Since the proposed controller uses its feedback loop to cancel the joint dynamics, the parameters of the joint are very important information, which is likely to be accurately known. Using the transfer functions of the single flexible joint robot shown in Eqs. (3.10) and (3.11), the parameters can be identified by matching the simulated and measured frequency response curves, as shown in Figure 3.6.

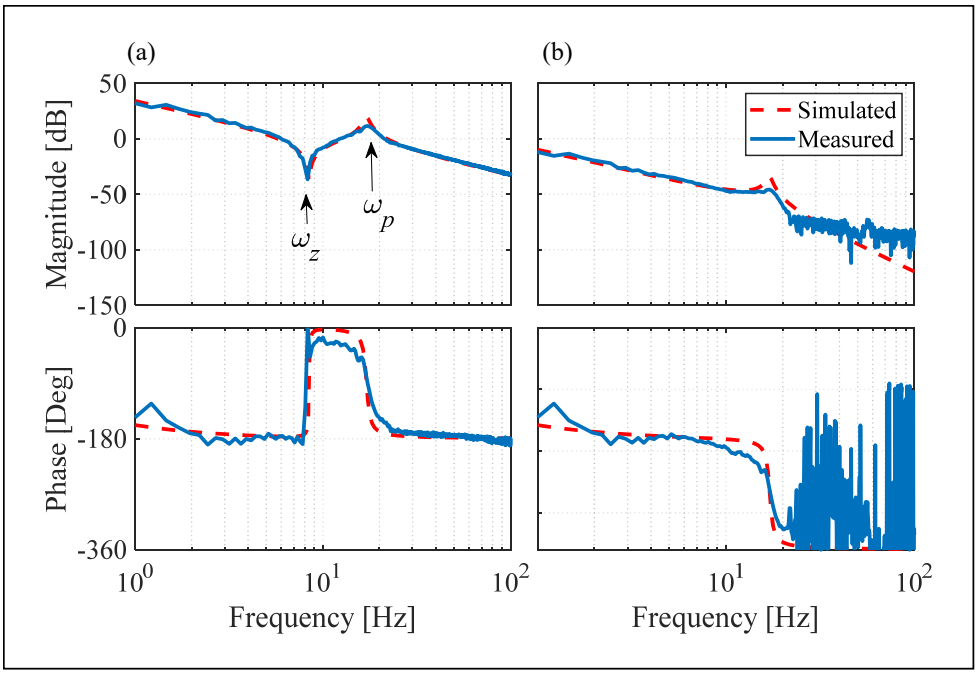

Figure 3.6 Comparison of the simulated and the measured open-loop frequency responses of the single flexible joint robot. (a) The motor position plant $q_m(s)/u(s)$ and (b) The link position plant $q_l(s)/u(s)$

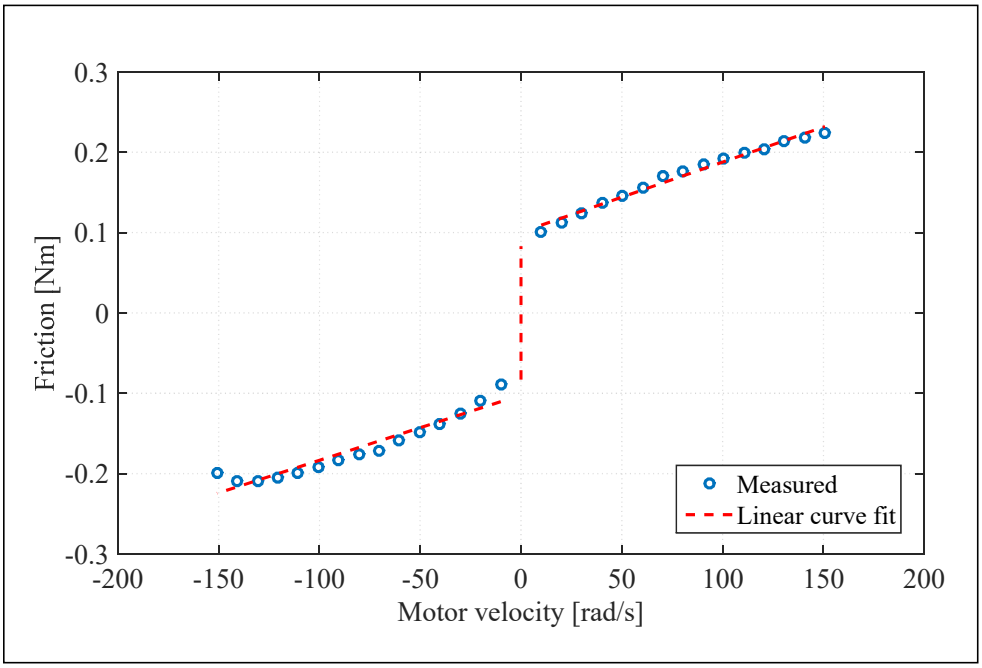

Figure 3.7 The experimental identification of the joint friction

Table 3.1 Single flexible joint robot parameters identified

Symbol	Quantity	Value
J_l	Total link side inertia	8.9 kgm^2
J_m	Motor inertia	1.12×10^{-4} kgm^2
N_r	Harmonic drive gear ratio	160
k_r	Joint stiffness	2.5×10^{4} Nm/rad
b_l	Joint viscous friction	6 Nms/rad
b_m	Motor viscous friction	9.5×10^{-4} Nms/rad
b_f	Motor Coulomb friction	8.6×10^{-2} Nm

The coefficient of the joint viscous friction can be verified using a friction-velocity diagram, in which the friction torque is presented as a function of the motor velocity, as shown in Figure 3.7. The coefficient of the slope is the motor viscous friction coefficient b_m while the torque magnitude at near-zero speed gives the motor Coulomb friction coefficient. A consistent value of the motor viscous friction coefficient has been found even it is characterized by frequency responses or by extracting from the friction-speed diagram.

The identified parameters of the single flexible joint are shown in Table 3.1. The undamped frequencies of the zeros and of the poles are ω_z = 8.435 Hz and ω_p = 17.085 Hz, respectively.

3.5.3 Controller gain selection

The two-stage feedback controller and the disturbance-state observer of the proposed enhanced two-stage feedback controller are configured following the procedure detailed in the section 3.4.6. The rigid control is designed according to the section 3.3.2. The controller gains are given in the following:

The control gains of the enhanced two-stage feedback controller are obtained by increasing λ_1

and λ_m such that good tracking performance of the link position and low vibration are achieved. The fluctuation or saturation on the motor torque is avoided. Practically, the values $\lambda_l = 9.5\,\text{Hz}$ and $\lambda_m = 12.7\,\text{Hz}$ are determined.

The matrix **L** of the state observer is obtained by placing the four poles of the matrix **(A–LC)** at the location **p** = [–400, –400, –600, –600]. For both the link and the motor sides of the disturbance observer, third-order critically damped low-pass filters are used, given the effectiveness of this filter in a robotic grinding application presented in (Hamelin et al., 2012). The low-pass filters have the form $Q_l(s) = \omega_{lc}^3 / (s + \omega_{lc})^3$. and $Q_m(s) = \omega_{mc}^3 / (s + \omega_{mc})^3$ for the link side and motor side, respectively. The low-pass filter cut-off frequencies of ω_{lc} = 100 rad/s and ω_{mc} = 200 rad/s are found experimentally to adequately reject disturbances and to maintain the control loop stability. Further increasing the cut-off frequencies may cause too much noise in the motor torque, resulting in even much more vibration on the link position.

The closed-loop stiffness of the rigid control is set using Eq. (3.23), i.e. $\omega_{n1} = 4.22\,\text{Hz}$ (26.5 rad/s), given that the minimum flexible mode frequency is ω_z = 8.435 Hz. Then the rigid controller gains are determined using Eq. (3.20) as $K_{p1} = 0.323\,\text{Nm/rad}$, $K_{d1} = 0.024\,\text{Nms/rad}$, and $K_{i1} = 1.07\,\text{Nm/rads}$.

3.5.4 Simulation and experimental results

This section presents the simulation and experimental study on the control performance of the single flexible joint robot using two control methods: the rigid control (RC) and the enhanced two-stage feedback controller (ESFB).

a. Closed-loop bandwidth

In this section presents a study on the control bandwidth. First, the closed-loop system is defined as the transfer function from the reference link position to the actual link position. The control bandwidth is then defined as a range from 0 Hz to ω^{BW} Hz, at which the magnitude of frequency response of the closed-loop transfer function crosses $\pm 3\text{dB}$:

$$\left| \frac{q_l(s)}{q_l^d(s)} \right|_{s=j\omega^{BW}} = \pm 3\text{dB} \tag{171}$$

where q_l and q_l^d are the actual link position and the reference link position, respectively.

First, assuming there are no disturbances induced on the single flexible joint model, the simulated frequency responses of the closed-loop systems using rigid control and using the proposed enhanced two-stage feedback control are shown in Figure 3.8. The simulation results show that the closed-loop system using rigid control has the control bandwidth of 4.8 Hz and a large vibration resonance occurs at the flexible mode frequency ω_z. On the other hand, the simulated control bandwidth of the closed-loop system using the enhanced two-stage feedback control is infinite, which is an expected result when no disturbance is applied (discussed in Section 3.4.4). The control bandwidth of the closed-loop system using the enhanced two-stage feedback control is reduced if the system is subjected to the disturbances such as external torques, modelling mismatches, nonlinear effects, quantization effects of encoders, or feedback signal delays. A numerical simulation is conducted to illustrate the effect of disturbances. Assuming 30% mismatch on the joint stiffness, the control bandwidth of the closed-loop system using the enhanced two-stage feedback control is reduced to 26.03 Hz, as shown in Figure 3.9. The hypothesis used in this simulation is reasonable given the fact that the harmonic drive reducer, the main source of the joint flexibility, has a nonlinear stiffness, which is normally varied up to 36% (HarmonicDrive, 2009).

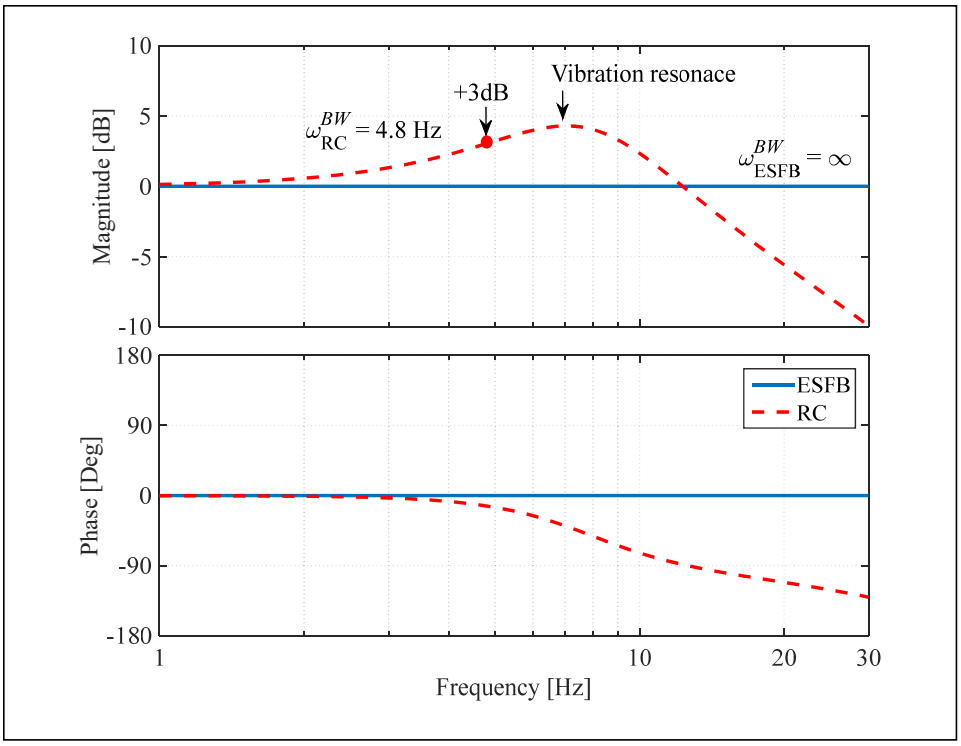

Figure 3.8 Simulation: the closed-loop frequency responses using rigid control (RC) and using enhanced two-stage feedback control (ESFB) assuming no disturbances

As shown in Figure 3.9, the frequency response of the closed-loop using the enhanced two-stage feedback control is approximately unity for the frequencies less than the cut-off frequency of the low-pass filter of the disturbance observer on the link side Q_l (about 15.9 Hz). Within this frequency range, the disturbance observer significantly compensates the disturbances of the single flexible joint model. For frequencies higher than the cut-off frequency of the low-pass filter Q_l, the position tracking performance of the link position starts to be decreased due to the disturbances that are not compensated. This result verifies the importance of the low-pass filter of the disturbance observer in the motion control performance, as discussed in the section 3.4.4.

Although the control performance is reduced due to the presence of disturbances, the performance of the proposed enhanced two-stage feedback control is always better than the

rigid control. Figure 3.9 shows that the closed-loop using the enhanced two-stage feedback control has the control bandwidth of 26.03 Hz, which is significantly higher than that using the rigid control (3.8 Hz).

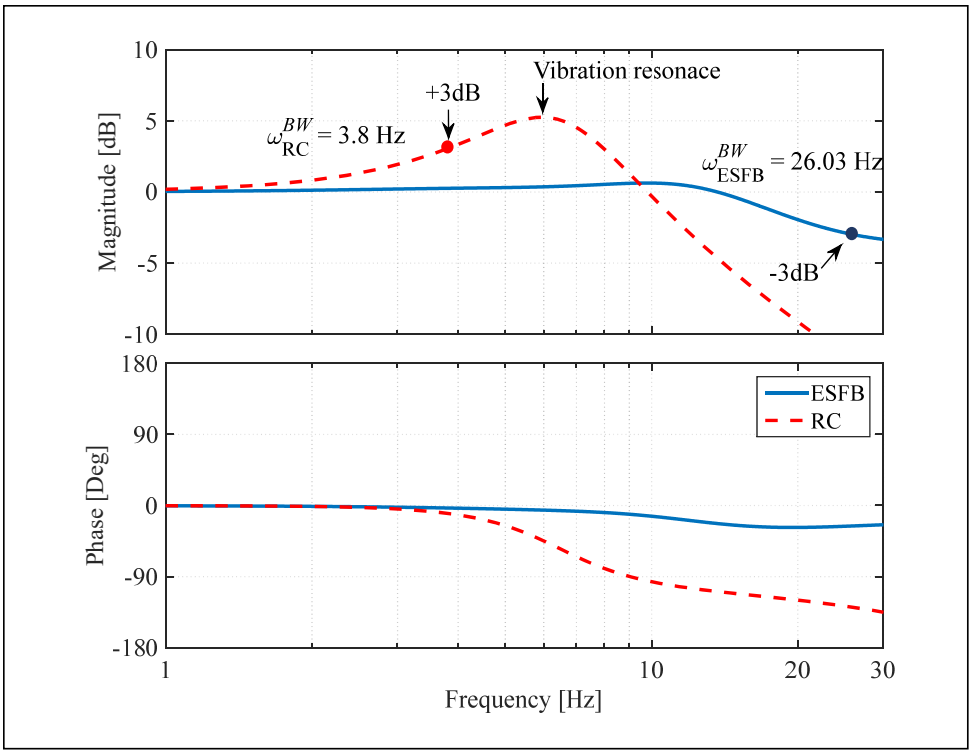

Figure 3.9 Simulation: the closed-loop frequency responses using rigid control (RC) and using enhanced two-stage feedback control (ESFB) assuming 30% uncertainty on joint stiffness

Figure 3.10 shows the experimental frequency responses of the closed-loop system using the rigid control and using the enhanced two-stage feedback control. Note that, due to the limitations of motor current and encoder resolutions, the test bench in this study just allows to measure the closed-loop frequency responses up to 20 Hz. Since there is a significant resonance in the response of the closed-loop using rigid control up to about 5 dB, the control bandwidth with rigid control is determined at the frequency response magnitude crossing +3 dB. Figure 3.10 shows that the control bandwidth with rigid control is about 5.5 Hz. In contrast to the rigid

control, the closed-loop response with the enhanced two-stage feedback control has almost no resonance at ω_z (8.435 Hz), resulting in very low link vibration. Therefore, the closed-loop bandwidth can be determined as the frequency response magnitude crossing -3dB. As shown in Figure 3.10, the bandwidth of the closed-loop using the enhanced two-stage feedback is about 16 Hz, which is almost twice the first flexible mode frequency (ω_z = 8.435 Hz) and is about three times that of the rigid control. Due to the high achievable closed-loop bandwidth, the enhanced two-stage feedback allows the link to accurately track link position references at frequencies that are impossible with the rigid control. In addition, the phase lag is effectively reduced using the enhanced two-stage feedback control, as presented in the phase diagram (the bottom figure of Figure 3.10).

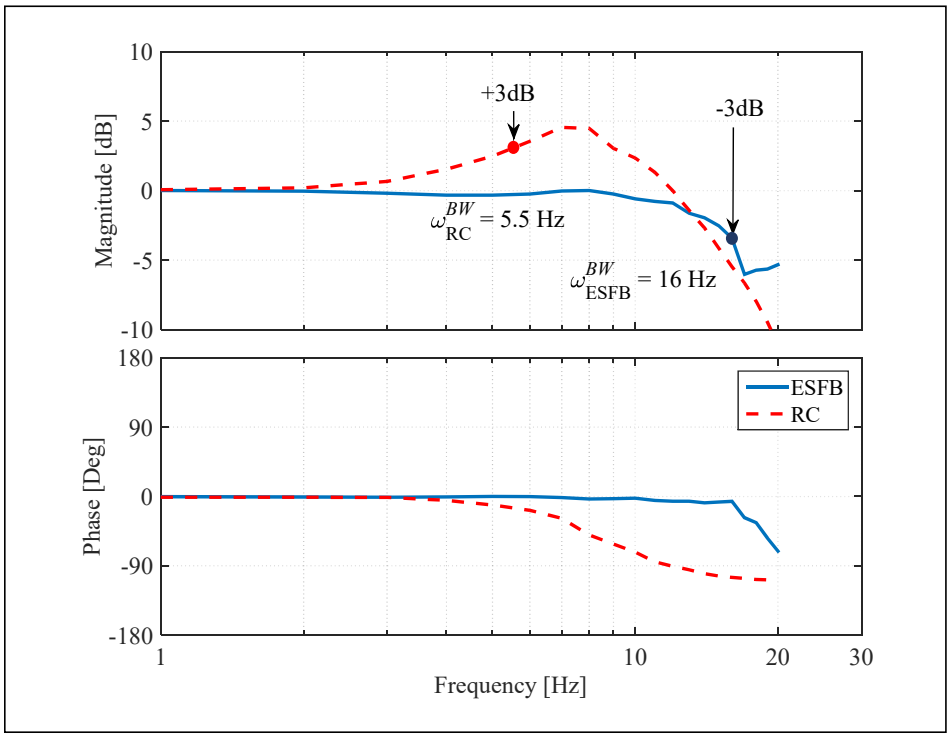

Figure 3.10 Experiment: the closed-loop frequency responses using rigid control (RC) and using enhanced two-stage feedback control (ESFB)

The bandwidth of rigid control obtained from the experimental closed-loop frequency response

(Figure 3.10) confirms the rigid control design method proposed in (Craig, 1989), where the frequency ω_{n1} is recommended to be half of the flexible mode frequency.

It is almost impossible to crank up the frequency ω_{n1} of the rigid control above half of the flexible mode frequency ω_z without deteriorating the transient response performance. High frequency ω_{n1} causes significant link vibration and motor torque noise. By decreasing the frequency ω_{n1} below half of the flexible mode frequency ω_z, the link vibration of the closed-loop using rigid control can be slightly reduced. However, the vibration resonance peak of the closed-loop using rigid control is always far above that using the enhanced two-stage stage feedback control. In addition, low frequency ω_{n1} leads to a significant deterioration of the disturbance rejection and the position tracking in low frequencies.

b. Step response

This section presents the control performance with the step reference signal. Although smooth references are normally available in control processes, the controllers are also expected to provide good control performance with non-smooth inputs, such as step signals. In this study, a step with magnitude of 0.1 rad is used to test all controllers.

As shown in Figure 3.11, the enhanced two-stage feedback clearly outperforms the rigid control. The settling time is defined as the time for the tracking error to fall within 2% of the final value. The settling time of the link using the enhanced two-stage stage feedback control is 0.22 s, which is about twice faster than that using rigid control (0.41 s). The link with enhanced two-stage feedback has a little slower rise time (0.11 s) compared to that with rigid control (0.09s). Although the rigid control provides a faster rise time, it comes up with a large overshoot (28.49%) while the enhanced two-stage feedback gives a critical damping link response. The link overshoot of the enhanced two-stage feedback is 0.11%, which is almost negligible. During the first 0.1s, the link responses using the enhanced two-stage feedback control and the rigid control are equivalent due to actuator saturation (see the bottom figure of

Figure 3.11).

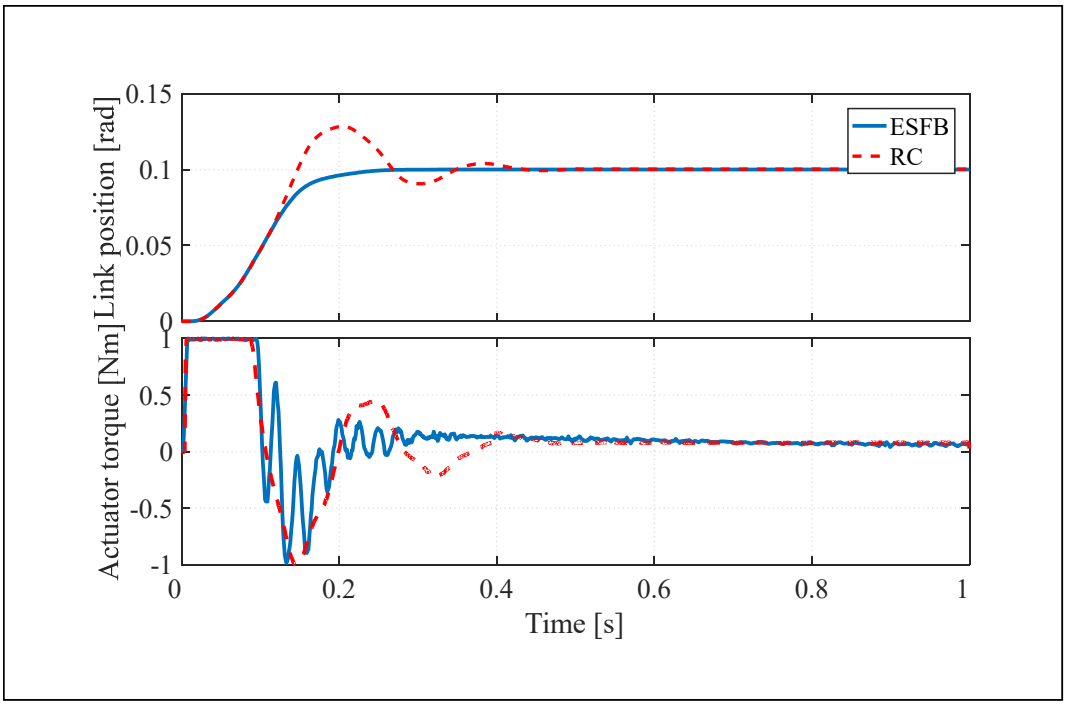

Figure 3.11 Experiment: the link step response

c. Kinematic error compensation

In this section, the link vibration due to kinematic error of the harmonic drive reducer is studied. The kinematic error is one of the most important concerns when using harmonic drive reducer for robotic joints. The kinematic error causes an inaccuracy of the robot kinematic by introducing a deviation between the expected and the actual positions of the harmonic drive reducer output. It is a periodic positioning error, which may excite the natural frequencies of the robot manipulator. The dominant frequency of the kinematic error is twice frequency of the wave generator (Cheng-Huei, Chun-Chih, & Masayoshi, 2008). Therefore, to examine how the flexible joint dynamics is excited by the kinematic error, the frequency of the wave generator is set to about half of the first flexible mode frequency (ω_z). The reference motor

position is one complete rotation in the counter-clockwise direction with the frequency f_m = 4 Hz (240 rpm).

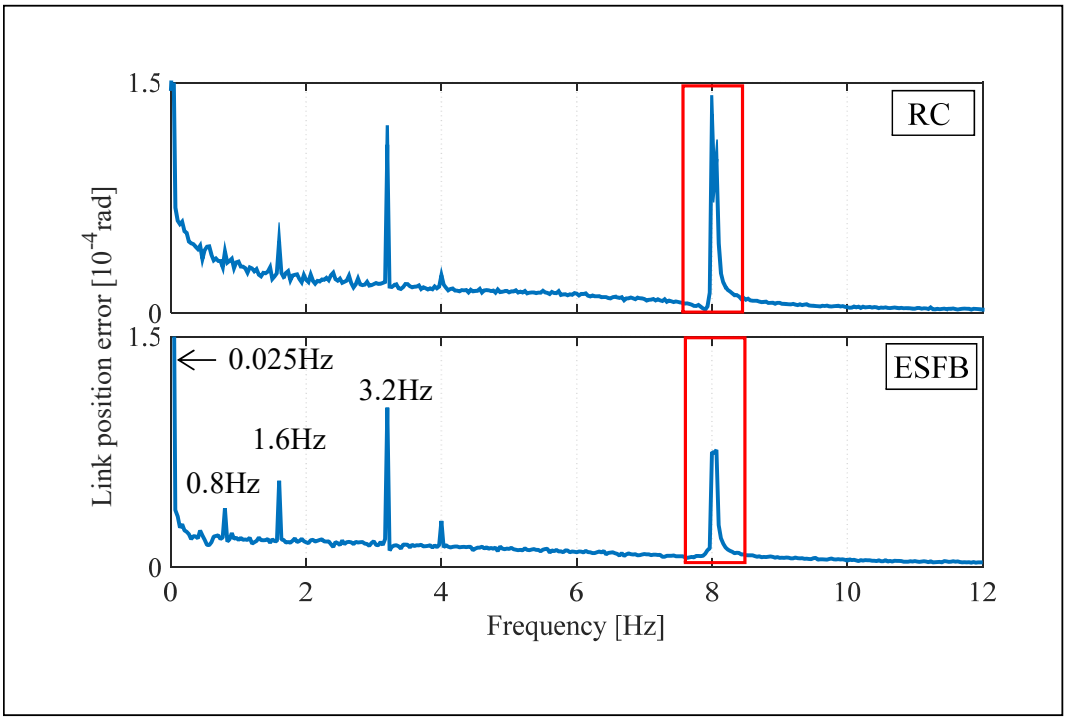

Figure 3.12 Experiment: the link vibration due to kinematic error of the harmonic drive reducer

Figure 3.12 shows the fast Fourier transform of the link position tracking error using the rigid control and the proposed enhanced two-stage feedback control. The vibration resonance at 8 Hz due to the kinematic error with the rigid control is about 1.4×10^{-4} rad. The vibration resonance due to the kinematic error with the enhanced two-stage feedback control is effectively reduced by 50% , with a lower peak of about 0.75×10^{-4} rad. There is synchronized vibrations occurred at $32\times f_l$ (0.8 Hz), at $64\times f_l$ (1.6 Hz), and at $128\times f_l$ (3.2 Hz) where f_l is the frequency of the link rotation, i.e. $f_l = f_m / N_r$ (= 0.025 Hz) with $N_r = 160$. These induced harmonics may be caused by quantization effect when computing the motor velocity by the backward derivative method from the motor position, given that the ratio between the

resolutions of the encoders on the link side and on the motor side is 32:1 (see section 3.5.1).

The performance of the rigid control and the enhanced two-stage stage feedback control in terms of the step response, the closed-loop control bandwidth and the kinematic error compensation are summarized in Table 3.2.

Table 3.2 Experimental comparison of control performance in terms of step response, control bandwidth and kinematic error compensation

	Step response			Bandwidth	Kinematic error peak (at about ω_{n1})
	Over-shoot	Rise time	Settling time		
RC	28.49%	0.09 s	0.41 s	0 ~ 5.5 Hz	1.4×10^{-4} rad
ESFB	0.11%	0.11 s	0.22 s	0 ~ 16 Hz	0.75×10^{-4} rad

d. Comparison of the proposed enhanced two-stage feedback control with the two-stage feedback controller

This section presents a control performance comparison of the proposed enhanced two-stage feedback control (disturbance-state observer turned on) with the two-stage feedback control (disturbance-state observer turned off), which is denoted as SFB. The comparison is to emphasize the important of the disturbance-state observer. The gains of the two-stage feedback control and the parameters of the disturbance-state observer are given in Section 3.5.3. Figure 3.13 shows the step response of the link position using the proposed the enhanced two-stage feedback control and using the two-stage feedback control.

The disturbance observer and state observer may improve the motion control performance of the flexible joint robot in different ways. The disturbance observer helps the feedback controller to track the link reference position faster with less overshoot (see Figure 3.13). The contribution of the state observer on the performance of the enhanced two-stage feedback

control in terms of link position tracking is not very clear. In other words, the link position tracking performance is almost unchanged with the state observer enabled or disabled. However, the state observer clearly helps to reduce the noise of the motor torque. Since the enhanced two-stage feedback control uses the link velocity in its computational process, the low-noise link velocity estimated by the state observer (see Figure 3.14) leads to a reduction of the motor torque noise, as shown in Figure 3.15. The link velocity error and the motor torque with the proposed enhanced two-stage feedback control are always inside the bounded areas (denoted by dashed lines) created by the control performance of the two-stage feedback control. In practice, with the two-stage feedback control, during the tests, the motor torque noise can be heard and could eventually damage the test bench. These experimental results again motivate the use of the state observer for the proposed controller.

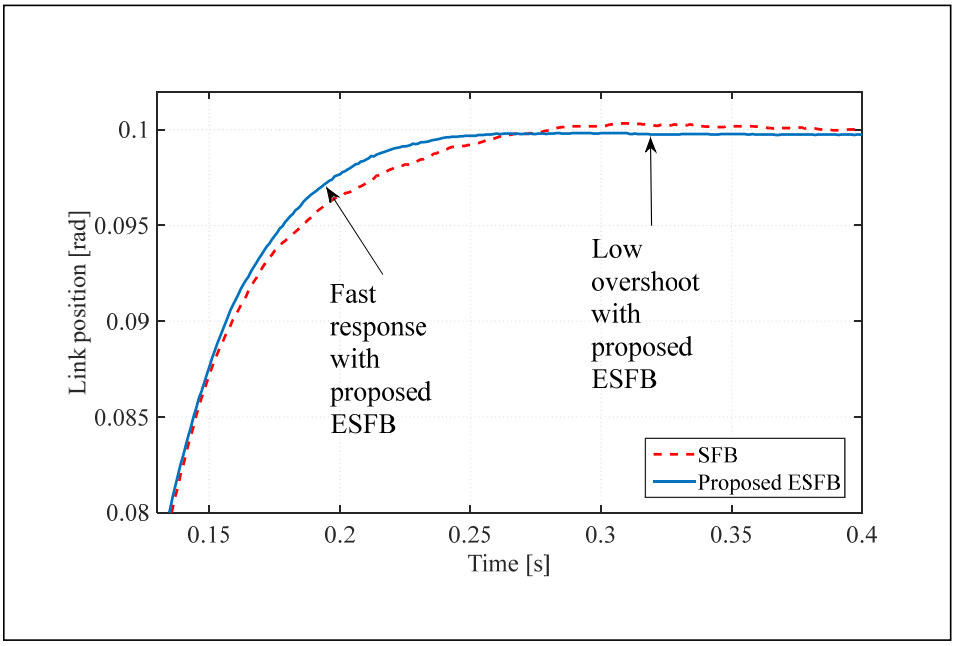

Figure 3.13 Experiment: the link step responses using the enhanced two-stage feedback control (ESFB) and using the two-stage feedback control (SFB)

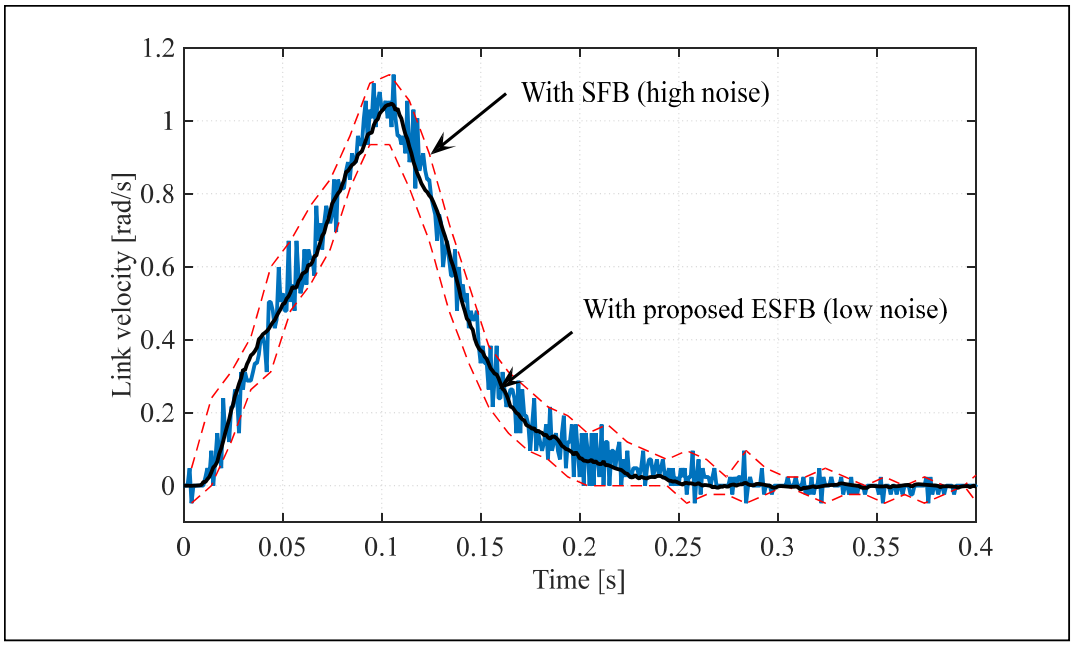

Figure 3.14 Experiment: the link velocities of the step response experiment with the proposed enhanced two-stage feedback control (ESFB) and with the two-stage feedback control (SFB)

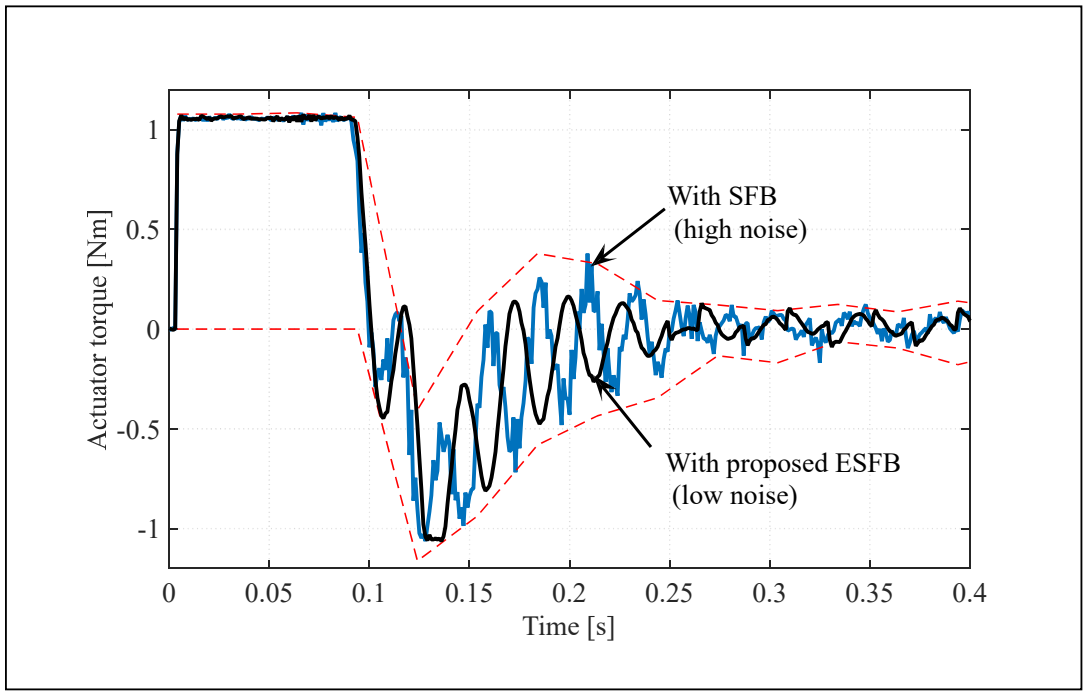

Figure 3.15 Experiment: the motor torques of the step response experiment with the proposed enhanced two-stage feedback control (ESFB) and with the two-stage feedback control (SFB)

3.6 Summary

This chapter presented the enhanced two-stage feedback to improve motion control performance of the single flexible joint robot. The main contributions of this study can be listed as follows:

1) It introduces the two-stage feedback control with partitioned controllers on both motor and link side controller.
2) It introduces the enhanced two-stage feedback controller, which is an integration of the two-stage feedback control with the disturbance-state observer. The disturbance on both motor side and link side dynamics of the single flexible joint robot are compensated.
3) It presents the simulation and experimental studies to validate the control approaches. A rigid control is implemented to provide a baseline of the control performance of recent industrial robots. It shows that the proposed enhanced two-stage feedback control extends the control bandwidth by two times the first flexible mode frequency and by three times the rigid control. With the step reference, the proposed enhanced two-stage feedback control accurately displaces the link of the single flexible joint robot. There is almost no overshoot and the settling time is two times faster than that of the rigid control. The vibration due to the kinematic error is reduced by 50%. The disturbance-state observer effectively compensates the disturbances and reduces the acoustic noise.

CHAPTER 4

VIBRATION CONTROL OF MULTIPLE FLEXIBLE JOINT ROBOTS USING A DISCRETE-TIME TWO-STAGE CONTROLLER BASED ON TIME VARYING INPUT SHAPING AND DELAY COMPENSATION

This chapter presents a two-stage controller to reduce vibration of a multiple flexible joint robot. The proposed controller can be retrofitted into existing robots, for which access to motor torque command is unavailable. A decentralized flexible model is introduced, in which the lumped coupling stiffness is taken into account. In the first-stage, an input shaping feedforward shapes the rigid closed-loop dynamics into a desired dynamics that does not produce link vibrations. Robotic dynamic computation based on a recursive Newton-Euler Algorithm is conducted to update the feedforward link inertia parameter during robot motion. A second-stage is added to increase disturbance rejection. A generalized Smith predictor is developed to compensate for delay and feedback sensor filtering. A simple methodology is presented to adjust the control loop gains. A discrete energy separation algorithm allows identifying the flexible dynamics parameters from the closed-loop temporal response. Numerical simulations and experiments on a six-joint robot manipulator confirm that the proposed controller improves control performances in terms of bandwidth, vibration attenuation, and disturbance rejection. This chapter is based on an article titled *"Vibration control of flexible joint robots using a discrete-time two-stage controller based on time-varying input shaping and delay compensation"* submitted to Robotics and Autonomous Systems in December 2019 (Pham, Hazel, Hamelin, & Liu, 2019).

4.1 Introduction

As discussed in the previous chapter, the performance of industrial robot is limited due to the presence of structural flexibilities. It is impossible or very difficult to build rigid manipulators, especially in the case of serial robots. Unavoidable flexibilities may emerge from gear boxes, links, joint bearings, and other mechanical components of the robot. Regardless of size, most

serial robots are quite flexible, with the first resonance in a low frequency range of about 10 Hz (Doria, Cocuzza, Comand, Bottin, & Rossi, 2019). Due to this flexibility, controllers based on rigid model assumption are no longer sufficient for precise positioning applications.

A classical PD controller can be adapted for flexible cases, which is discussed in (Tomei, 1991a). Although the control structure can be reused, the controller gains must be limited to avoid exciting vibration modes, which result in a low control bandwidth. Another approach is to employ a flexible joint model to design advanced controllers. Effective control methods include feedforward-feedback (Lessard et al., 2014), passivity-based (Albu-Schäffer, Ott, & Hirzinger, 2007), elastic structure preserving (Keppler, Lakatos, Ott, & Albu-Schäffer, 2018), feedback linearization (Nanos & Papadopoulos, 2015), back-stepping (Bang et al., 2010; Lin & Goldenberg, 1995), disturbance observer based (Yun, Su, Kim, & Kim, 2013), and iterative learning control (W. Chen & Tomizuka, 2014; C. Wang, Minghui, Wang, & Tomizuka, 2016). Implementations of these methods may require access to motor torque command, and, in some cases, complex control schemes. Successful adaptations of these methods for industrial robots still require more work in order to address various constraints. The first major one of many such constraints is that most industrial robots comprise built-in joint motion controllers, which only allow gains modification. The access to motor torque command is not provided. Some commercial industrial robots even allow only pose reference correction via the implementation of additional software packages, such as the Externally Guided Motion (EGM) of ABB robots (Zhang et al., 2018), Dynamic Path Modification of Fanuc robots (Gharaaty, Shu, Joubair, Xie, & Bonev, 2018; Shu, Gharaaty, Xie, Joubair, & Bonev, 2018), or Robot Sensor Interface (RSI) of Kuka robots (Shi, Zhang, Qu, & Liu, 2016). Another constraint is the fact that delays and quantization noises may be present on the feedback signals, which significantly deteriorate control performance if they are not considered.

With the above constraints considered, input shaping is an effective technique for realizing high-level controllers. It ensures vibration attenuation via a trajectory optimization procedure alone. Once the vibration problem is handled by input shaping, feedback control gains can be increased to extend the bandwidth. In an early development by Smith in (J. Y. Smith, Kozak,

& Singhose, 2002), which was later covered in extensive study by Singhose (Singhose, 2009), various types of finite impulse response input shapers (FIRIS) were developed, including zero-vibration (ZV), zero-vibration-derivative (ZVD), and extra insensitive (EI). While FIRIS may provide adequate vibration attenuation performance, the order of the discrete-time FIRIS filter transfer function may be high, resulting in long delays. In order to avoid this problem, infinite impulse response input shaping (IIRIS) based on an inverse model could be used instead. In the latter, vibration is attenuated based on the pole/zero cancellation technique, which requires a good knowledge of the dynamic model.

Dynamic models of robots have been fully covered in many research studies, such as (Lightcap & Banks, 2010; Sariyildiz et al., 2016; Yun et al., 2013). Multiple joint robot models are very complex, even if they only include flexible joints. Such models must thus be simplified into a series of decentralized flexible joint sub-models, in which the joint is represented by the motor mass and the link mass, connected via a reducer (Houman Dallali et al., 2015; H. Dallali, Medrano-Cerda, Kashiri, Tsagarakis, & Caldwell, 2014; Paine et al., 2015). The decentralized flexible joint model can be used to design joint level controllers. Such model, however, is unable to fully reflect reality behavior since it does not take into account the flexibility of many other parts of robots such as links and bearings. Not modelling these components may lead to severe stability and robustness problems, especially when fast motions are required. It is desirable to develop a single flexible joint model, in which coupling dynamics with other parts of the robot are taken into account.

In addition to vibration control, disturbance rejection is also important. An effective way to improve the robustness and disturbance rejection of controlled systems is to introduce a second control stage in the process, such as the one studied by Morales (Morales et al., 2012). In such cases, link-side feedback delays and quantization become a major issue. It should be mentioned that a disturbance-state observer could be used to estimate feedback signals. The estimated feedback signals do not have delay and noise. However, such an observer requires sufficient knowledge of the complicated dynamic model of the robot arm (Bang et al., 2010; Pham, Hamelin, Hazel, & Liu, 2019). A simple yet effective method is to implement filters in the

feedback path to damp out any sensor noise, but this introduces more delay, which may further reduce stability margins.

In this chapter, we focus on a combination of a two-stage control with an input shaping feedforward for reducing vibration of serial robots. The proposed algorithm can be retrofitted straight into existing industrial robots with built-in joint controllers. This study extends previous works as follows:

1) It extends the classical decentralized joint model by taking into account a lumped stiffness resulting from a dominant coupling mode.
2) It provides a two-stage controller including an input shaping feedforward with time-varying updating in the first-stage and a generalized Smith predictor to compensate for delay and feedback sensor filtering in the second-stage.
3) It provides experimental results on an actual six-joint industrial robot.

This chapter is organized as follows. Section 4.2 details the flexible robot decentralized modelling. Section 4.3 presents the conventional rigid control and the proposed control approach, along with a detailed stability and sensitivity analysis. Section 4.4 presents the experimental results validating the effectiveness of the proposed approach.

4.2 System modelling

This section presents the modelling of the flexible robot in the presence of a high coupling effect.

4.2.1 Flexible joint robot modelling background

A dynamic model of a flexible joint robot was fully developed using the Lagrange formulation and Spong's assumption as follows:

$$\mathbf{M}_l(\mathbf{q}_l)\ddot{\mathbf{q}}_l + \mathbf{C}(\mathbf{q}_l,\dot{\mathbf{q}}_l)\dot{\mathbf{q}}_l + \mathbf{B}_l\dot{\mathbf{q}}_l + \mathbf{g}(\mathbf{q}_l) = \boldsymbol{\tau}_j \tag{4.1}$$

$$\mathbf{J}_m\ddot{\mathbf{q}}_m + \mathbf{B}_m\dot{\mathbf{q}}_m + \mathbf{B}_f \operatorname{sgn}(\dot{\mathbf{q}}_m) + \mathbf{N}_r^{-1}\boldsymbol{\tau}_j = \mathbf{u} \tag{4.2}$$

where $\mathbf{q}_l$ and $\mathbf{q}_m$ are the link and motor position vectors, $\mathbf{M}_l(\mathbf{q}_l)$ is the link inertia matrix, $\mathbf{C}(\mathbf{q}_l,\dot{\mathbf{q}}_l)$ is the Coriolis and centrifugal forces matrix, $\mathbf{B}_l$ is the joint damping diagonal matrix, $\mathbf{g}(\mathbf{q}_l)$ is the gravitational forces vector, $\mathbf{N}_r$ is the gear ratio diagonal matrix, $\mathbf{J}_m$ is the motor inertia diagonal matrix, $\mathbf{B}_m$ and $\mathbf{B}_f$ are the diagonal matrices of motor viscous friction and motor Coulomb friction, respectively, sgn(□) is the sign function, $\boldsymbol{\tau}_j = \mathbf{k}_r\left(\mathbf{N}_r^{-1}\mathbf{q}_m - \mathbf{q}_l\right)$ is the joint torque induced by the joint flexibility, $\mathbf{k}_r$ is the reducer stiffness diagonal matrix, and $\mathbf{u}$ is the actuator torque vector.

The flexible joint robot model in Eqs. (4.1) and (4.2) can be simplified into a conventional decentralized model, in which the robot is regarded as a series of single flexible joints. All nonlinear terms including $\mathbf{C}(\mathbf{q}_l,\dot{\mathbf{q}}_l)$, $\mathbf{g}(\mathbf{q}_l)$, $\mathbf{B}_f$, and coupling inertias (off-diagonal elements of $\mathbf{M}_l(\mathbf{q}_l)$) are ignored. Each joint model consists of a motor mass and a link mass, connected via a reducer, as shown in Figure 4.1.

An important assumption of the conventional decentralized model is that only the reducer itself is considered flexible. The connection between reducer and the link is rigid. The encoder placed at the reducer output can capture the link motion. It means there is no distortion between the reducer output position q_r and the link position q_l. Dynamic equations of flexible joint using decentralized model (CDM) are expressed in Eqs. (4.3) and (4.4), respectively.

Motor position:

$$J_m\ddot{q}_m + b_m\dot{q}_m + \frac{k_r}{N_r}\left(\frac{1}{N_r}q_m - q_l\right) = u \tag{4.3}$$

Link position or reducer output position:

$$J_l\ddot{q}_l + b_l\dot{q}_l + k_r\left(q_l - \frac{q_m}{N_r}\right) = 0 \tag{4.4}$$

Some modelling issues of the conventional decentralized model occur. While the conventional decentralized model assumes there is no distortion between the reducer output position q_r and the link position q_l, i.e. $q_l = q_r$, experimental results show a contradicting result. A considerable difference between these two signals was observed experimentally, as shown in Figure 4.2. Note that the link position is measured by a laser tracker and converted into joint angle for comparison while the reducer output position is captured by the encoder. The joint is controlled to follow a trapezoidal trajectory.

Distortion of experimental and simulation frequency responses of the closed-loop flexible joint is presented in Figure 4.3. The closed-loop transfer function is defined from the reference to the reducer output position. The experimental frequency response has a resonance and an anti-resonance while the simulation frequency response using the conventional decentralized model has only a resonance.

Although the reducer stiffness can be modified to allow closely matching of the simulated and measured frequencies of the resonance, it is very hard to explain why the modified reducer stiffness is much lower than the value from the manufacture specification. In addition, for any value of the reducer stiffness set for the simulations, the resonance amplitudes are still different and the anti-resonance are not modelled.

The modelling error using the conventional decentralized may be because the conventional model ignores the presence of the coupling effect between robot joints and the flexibilities of many other mechanical parts of robot manipulators. A flexible robot model which includes coupling, but is simpler than the model expressed by Eqs. (4.1) and (4.2) is desirable for practical implementations.

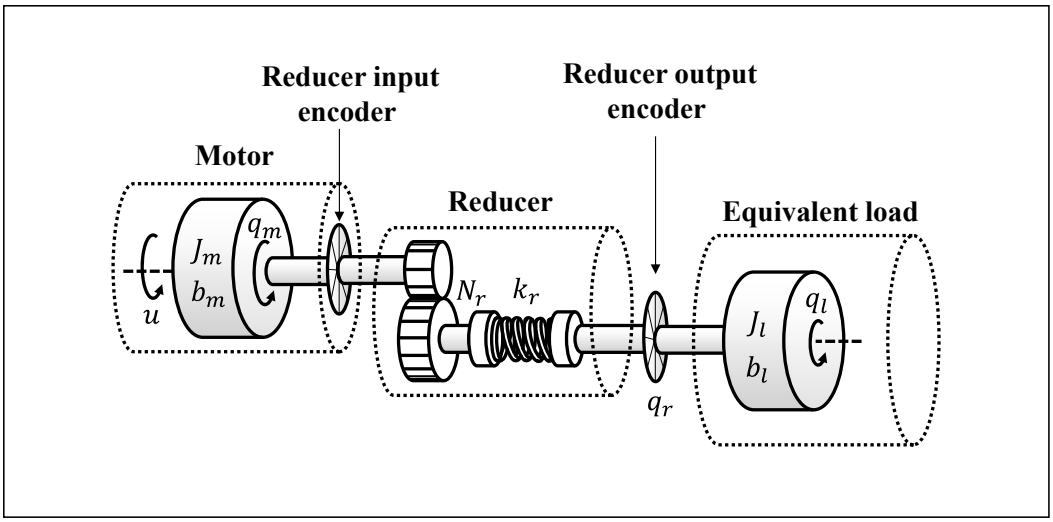

Figure 4.1 Conventional decentralized model of a flexible joint. The joint model consists of a motor mass and a link mass, connected via a reducer, which is the only element considered to be flexible

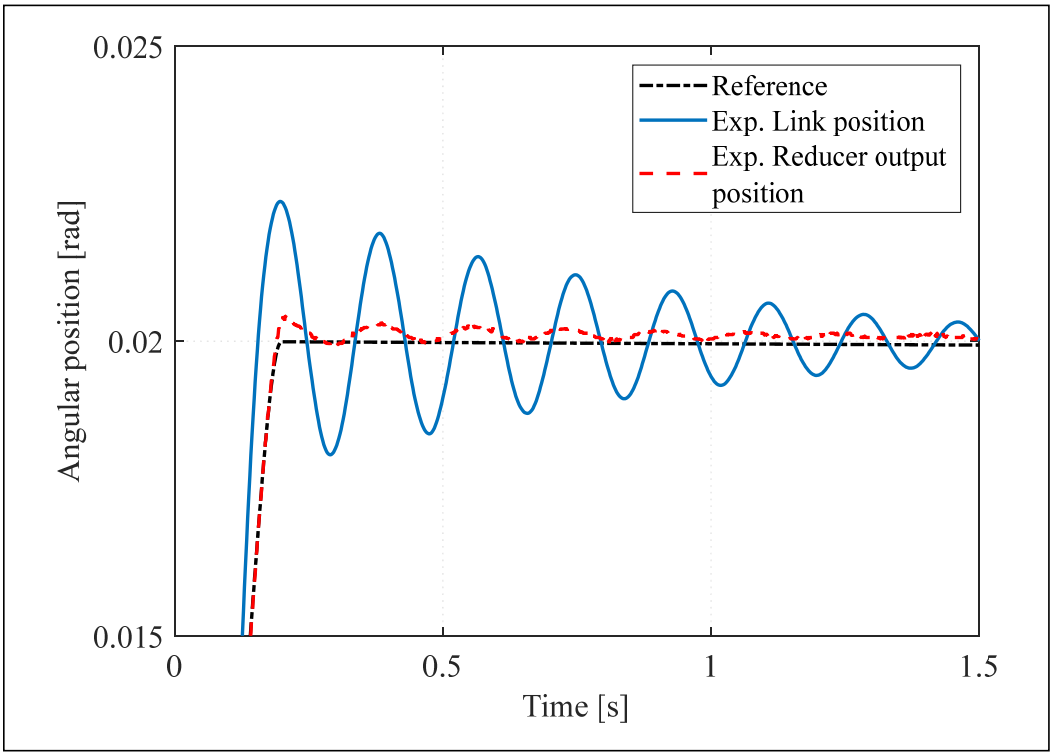

Figure 4.2 Experimental results of vibrations of the link and the reducer output position. It is unable to simulate the distortion between the link positon and the reducer output position using conventional decentralized flexible joint model

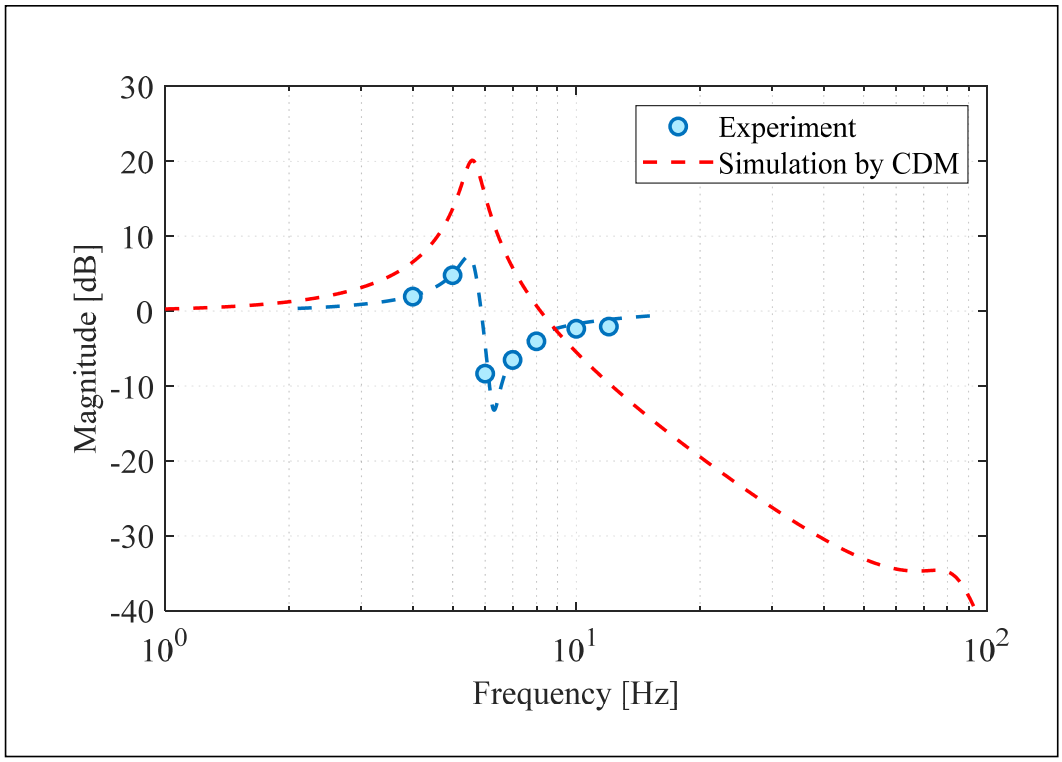

Figure 4.3 Closed-loop frequency response of a single flexible joint. The experimental frequency response has a resonance and an anti-resonance while the simulation frequency response using the conventional decentralized model (CDM) has only a resonance. Varying the reducer stiffness only allows the simulation using CDM matching the frequency of the resonance

4.2.2 Proposed flexible joint model

A flexible joint model that takes into account the coupling effect is proposed in this section. A schematic diagram of the flexible joint is depicted in Figure 4.4 (note that this model describes robots with two encoders for each joint). The major difference between the conventional flexible joint model and the proposed flexible joint model is that while the conventional flexible joint model ignores the coupling, the proposed flexible joint model introduces a new flexible coupling element, with stiffness k_c, between the reducer and the link inertia. The presence of the coupling stiffness allows the proposed flexible joint model to reflect (i) the

reduction of the overall stiffness between the motor mass and the link mass, and (ii) the distortion between the reducer output position and the link position.

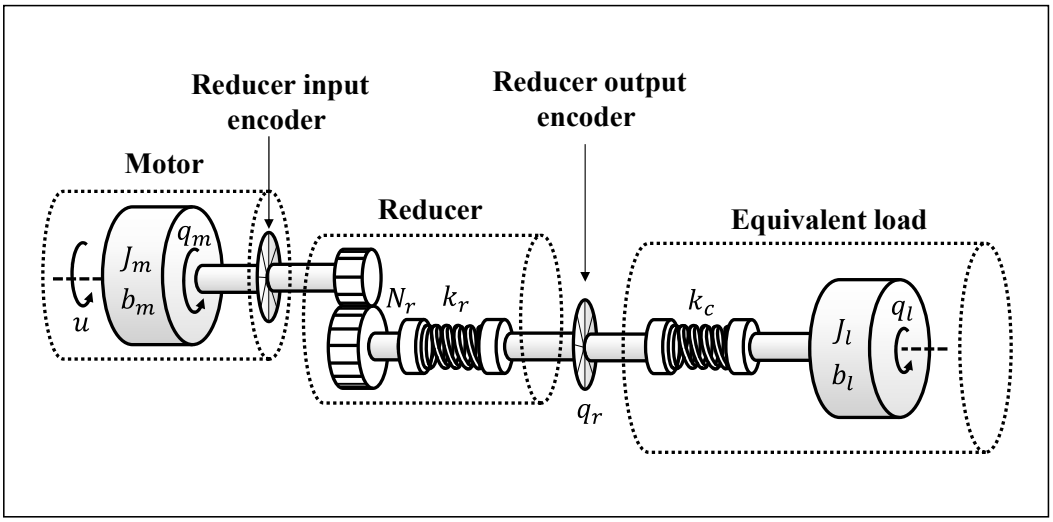

Figure 4.4 Proposed schematic diagram of a flexible joint model. The motor position q_m and the reducer output position q_r can be measured directly by encoders

The system's dynamic equations are given as follows:

Reducer input position or motor position:

$$J_m\ddot{q}_m + b_m\dot{q}_m + \frac{k_r}{N_r}\left(\frac{1}{N_r}q_m - q_r\right) + d_m = u \tag{4.5}$$

Reducer output position:

$$k_c\left(q_r - q_l\right) + k_r\left(q_r - \frac{1}{N_r}q_m\right) = 0 \tag{4.6}$$

Link position:

$$J_l\ddot{q}_l + b_l\dot{q}_l + k_c\left(q_l - q_r\right) + d_l = 0 \tag{4.7}$$

where q_m is the motor position, q_r is the reducer output position, q_l is the link position, J_m is the motor inertia, J_l is the link inertia, b_l is the link side viscous friction coefficient, b_m is the motor side viscous friction coefficient, k_r is the reducer stiffness, k_c is the coupling stiffness, and N_r is the reducer gear ratio. The actuator torque applied to the motor is denoted by u, while d_l and d_m are the link and motor side lumped disturbances, respectively.

The effective joint stiffness k_j is defined as the serial combination of the reducer stiffness k_r and the coupling stiffness k_c.

$$k_j = \frac{k_r k_c}{\left(k_r + k_c\right)} \tag{4.8}$$

In analyzing Eq. (4.8), a finite value of k_c implies that $k_c / \left(k_r + k_c\right) < 1$, leading to an overall stiffness reduction, that is $k_j < k_r$.

The transfer functions from the actuator torque to the motor position and to the link position are given in Eqs. (4.9) and (4.10), respectively.

$$\begin{aligned} M(s) &= \frac{q_m(s)}{u(s)} \\ &= \frac{J_l s^2 + b_l s + k_j}{J_l J_m s^4 + (J_l b_m + J_m b_l)s^3 + \left(J_l k_j N_r^{-2} + b_m b_l + k_j J_m\right)s^2 + \left(k_j b_m + k_j b_l N_r^{-2}\right)s} \end{aligned} \tag{4.9}$$

$$\begin{aligned} L(s) &= \frac{q_l(s)}{u(s)} \\ &= \frac{N_r^{-1} k_j}{J_l J_m s^4 + (J_l b_m + J_m b_l)s^3 + \left(J_l k_j N_r^{-2} + b_m b_l + k_j J_m\right)s^2 + \left(k_j b_m + k_j b_l N_r^{-2}\right)s} \end{aligned} \tag{4.10}$$

The function $L(s)$ also represents the transfer function from the link disturbance d_l to the motor position q_m. The undamped anti-resonance frequency ω_z and the resonance frequency ω_p of the flexible joint are given:

$$\omega_z = \sqrt{\frac{k_j}{J_l}} \tag{4.11}$$

$$\omega_p = \sqrt{\frac{k_j}{J_l} + \frac{k_j}{J_m N_r^2}} \tag{4.12}$$

These two frequencies are depicted in the bode plots of a typical coupled flexible joint shown in Figure 4.5. By dividing Eq. (4.9) by Eq. (4.10), the transfer function from the motor position to the link position can be derived as follows:

$$R(s) = \frac{q_l(s)}{q_m(s)} = \frac{k_j N_r^{-1}}{J_l s^2 + b_l s + k_j} \tag{4.13}$$

Note that the anti-resonance ω_z is also the natural frequency of the reducer transfer function $R(s)$ (Ellis, 2004). Taking the Laplace transform for Eq. (4.7), the coupling transfer function from link position q_l to reduce output position q_r is as follows:

$$K(s) = \frac{q_r(s)}{q_l(s)} = \frac{J_l}{k_c} s^2 + \frac{b_l}{k_c} s + 1 \tag{4.14}$$

From the Eq. (4.6), q_r can also be computed from q_m, and q_l, which can be written as follows:

$$q_r = \frac{k_c}{k_r + k_c} q_l + \frac{k_r N_r^{-1}}{k_r + k_c} q_m \tag{4.15}$$

It is worth mentioning that due to the presence of the coupling stiffness, the link position q_l

and the reducer output position q_r are dynamically related through the transfer function $K(s)$, as shown in Eq. (4.14).

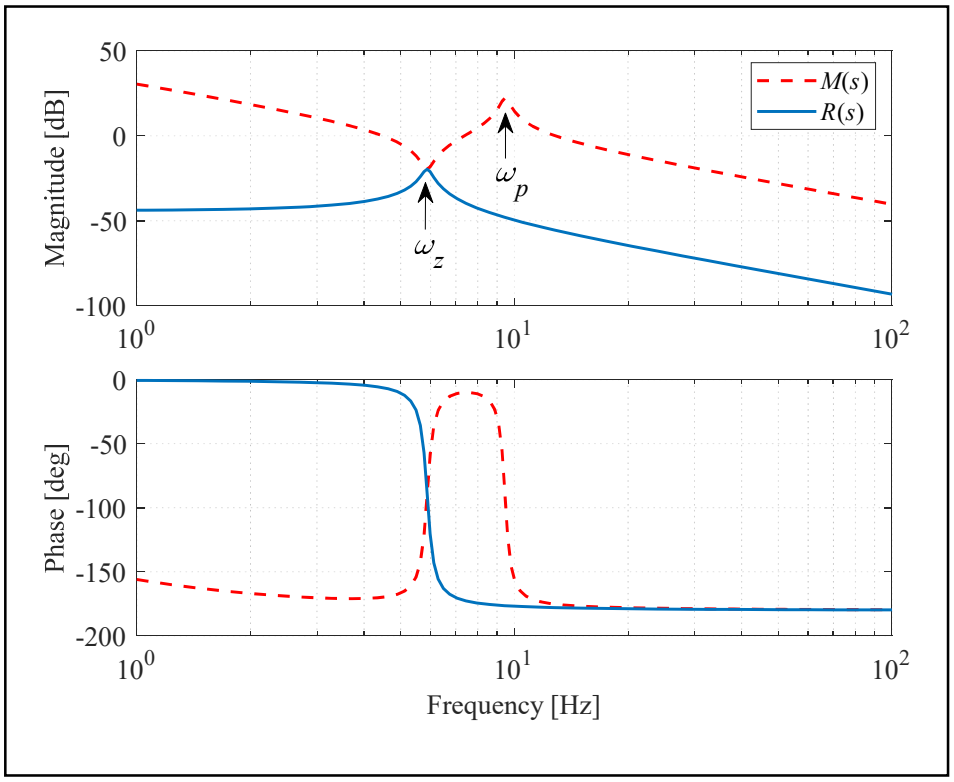

Figure 4.5 Frequency responses of the proposed flexible joint model. $M(s)$ is the transfer function from the motor torque to the motor position and $R(s)$ is the transfer function from the motor position to the link position

4.3 Controller design

Industrial robots usually have built-in joint motion controllers. Since the architecture of the built-in controller is unchangeable, it is preferable to modify the overall control performance by adding an input shaping and an outer feedback stage. For this reason, the two-stage controller is presented. The first-stage includes the built-in rigid controller, a feedforward input

shaping, and a time-varying updating dynamics. The main goal of the first-stage feedforward is to attenuate the vibration due to the joint flexibility, while the time-varying updating dynamics serves to adjust the feedforward transfer function according to robot configurations. The second-stage includes a generalized Smith predictor, a PID compensator, and a feedback low-pass filter. The intent of the second-stage is to improve the disturbance rejection performance. Figure 4.6 gives an overview of the block diagram of the closed-loop system using the two-stage controller.

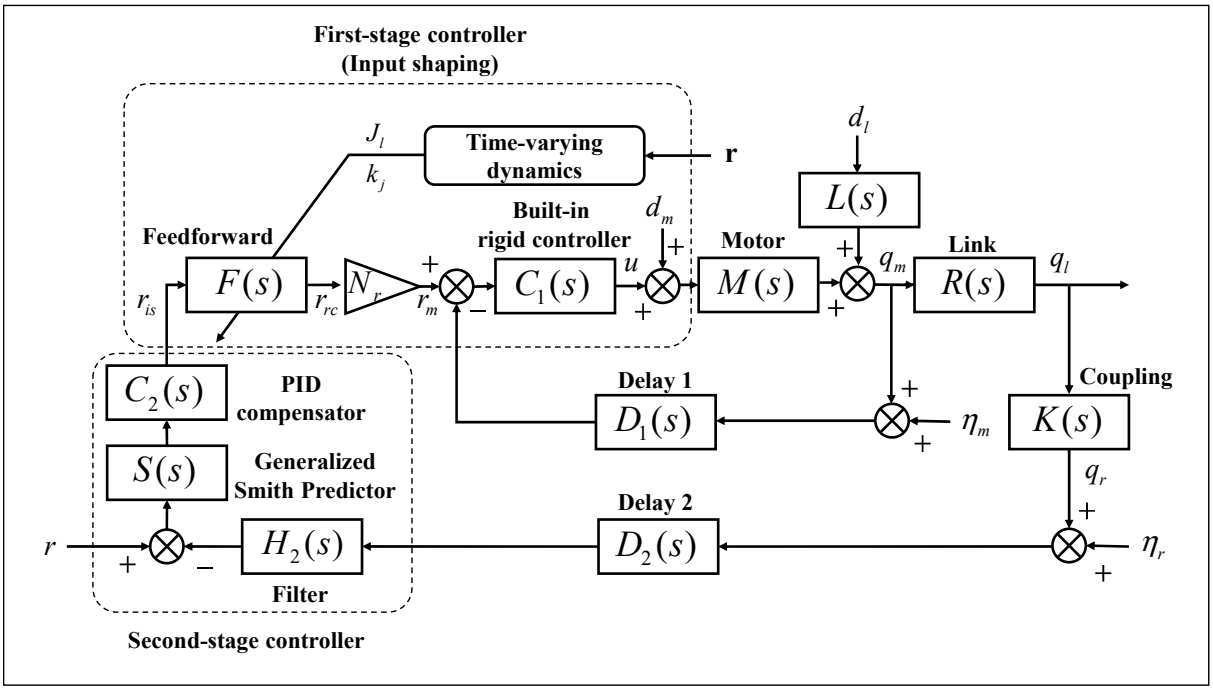

Figure 4.6 Block diagram of the proposed two-stage controller. $M(s)$, $R(s)$, $L(s)$, and $K(s)$ represent time-varying joint dynamics, depending on robot configurations

The references of the first-stage and of the second-stage are denoted as r_{is} and r, respectively. The reference of the rigid control loop is r_{rc}, while that of the motor is r_m. The reference of the second-stage r represents the desired position of the joint, which is smooth up to the

second derivation. The sensor noise on the motor side is η_m and that on the link side is η_r. The components of the two-stage controller are detailed in the rest of this section.

4.3.1 First-stage conventional built-in rigid controller

Because of the flexibility of the joints, the motor and the link positions are not simply coupled through the gear ratio, but through the joint dynamic model. Depending on whether the feedback is from the motor or from the reducer output, controllers can be classified as collocated or non-collocated, respectively. Most built-in joint controller use the collocated scheme. This scheme takes advantage of the phase characteristic of the motor transfer function (see Figure 4.5), thus facilitating the control. A non-collocated controller using reducer output feedback encounters more difficulties since the phase of the link transfer function drops quickly to -180 degrees at its anti-resonance frequency.

The classical proportional and derivative (PD) control is one of the simplest methods to realize a collocated controller. Based on a rigid body assumption, the PD gains (K_{p1} and K_{d1}) can be set as follows:

$$K_{p1} = J_e \omega_{n1}^2 \text{ and } K_{d1} = 2 J_e \zeta_1 \omega_{n1} \tag{4.16}$$

where $J_e = J_m + J_l N_r^{-1}$ is the effective inertia seen on the motor side and ζ_1 and ω_{n1} are respectively the damping ratio and the natural frequency of the closed-loop rigid joint.

When the rigid controller is applied to the flexible joint, the joint motion may excite the un-modelled flexible dynamics if the closed-loop bandwidth is close to the natural frequency of the un-modelled dynamics (Zinn et al., 2003). Therefore, the closed-loop natural frequency ω_{n1} can be adjusted as a function of the flexible joint natural frequency as follows:

$$\omega_{n1} = \lambda_1 \omega_z \tag{4.17}$$

The natural frequency ω_{n1} is now proportional to the flexible dynamic natural frequency ω_z via the parameter λ_1. The parameter λ_1 should be adjusted to compromise between the link vibration and control bandwidth. To avoid exciting the flexible dynamics, $\zeta_1 = 1$ and $\lambda_1 = 0.5$ are often suggested (Craig, 1989).

In order to reduce the steady-state error when controlling the flexible joint, an integral gain K_{i1} can be added. Assuming a critical damping of the PID transfer function, the integral gain can be set with respect to the proportional and derivative gains as follows:

$$K_{i1} = \frac{K_{p1}^2}{4K_{d1}} \tag{4.18}$$

The continuous-time PID rigid compensator transfer function is shown in Eq. (4.19):

$$C_1(s) = \frac{K_{d1}s^2 + K_{p1}s + K_{i1}}{s} \tag{4.19}$$

4.3.2 First-stage input shaping feedforward

The role of the input shaping feedforward is to shape the first-stage trajectory such that it cancels its own vibrations, leading to closed-loop dynamics that do not produce link vibrations. Instead of being directly designed in the discrete domain, the feedforward is designed from the continuous model of the rigid closed-loop transfer function. This approach is favored as to take advantage of the available closed-form solution for the continuous-time closed-loop model, thus avoiding order reduction problems that are common with numerical methods. However, obtaining the accurate continuous closed form may be challenging in the presence of delays. In the following, the design of the input shaping feedforward is presented, taking into account the delay in the first-stage feedback loop. Discussions on issues relating to the conversion from the continuous space to the discrete space are left for section 4.3.7.

The transfer function of the continuous-time first-stage, with rigid control only, can be expressed as follows:

$$G_1(s) := \frac{q_l(s)}{r_{rc}(s)} = N_r \frac{C_1(s)M(s)}{1+C_1(s)M(s)D_1(s)} R(s) \tag{4.20}$$

where $C_1(s)$ is the PID compensator and $D_1(s)$ is the delay in the feedback loop expressed as:

$$D_1(s) = e^{-T_{d1}s} \tag{4.21}$$

with T_{d1} being the delay of the loop feedback path.

There are many ways to approximate the delay by rational functions. Among these approaches, the Padé approximant is the most frequently used method. A key factor in the implementation of the Padé approximant is order selection. In fact, the higher the order, the higher the group delay bandwidth achieved. However, a high order Padé approximant results in a high order closed-loop model, which may complicate the proposed approach. Therefore, a second-order approximation is considered, which provides unity gain and linear phase up to about 20% of the Nyquist frequency. The rational continuous-time transfer function of the delay derived using second order Padé approximant (Pekař & Kureckova, 2011) is as follows:

$$D_1(s) \approx \frac{12-6\left(T_{d1}s\right)+\left(T_{d1}s\right)^2}{12+6\left(T_{d1}s\right)+\left(T_{d1}s\right)^2} \tag{4.22}$$

The feedback delay introduces a conjugate pole pair at high frequencies and slightly changes the closed-loop transfer function dynamics at low frequencies.

By manipulating transfer functions, Eq. (4.20) can be rewritten in rational form as follows:

$$G_1(s) = \frac{b_0 + b_1 s + b_2 s^2 + b_3 s^3 + b_4 s^4}{a_0 + a_1 s + a_2 s^2 + a_3 s^3 + a_4 s^4 + a_5 s^5 + a_6 s^6 + a_7 s^7} \tag{4.23}$$

where the coefficients are given as:

$$b_0 = 12k_j K_{i1},$$

$$b_1 = 12k_j K_{p1} + 6T_{d1} K_{i1} k_j,$$

$$b_2 = K_{i1} k_j T_{d1}^2 + 6k_j K_{p1} T_{d1} + 12K_{d1} k_j,$$

$$b_3 = k_j K_{p1} T_{d1}^2 + 6K_{d1} k_j T_{d1},$$

$$b_4 = k_j K_{d1} T_{d1}^2,$$

$$a_0 = 12k_j K_{i1},$$

$$a_1 = K_{i1}\left(12b_l - 6k_j T_{d1}\right) + 12k_j K_{p1},$$

$$a_2 = K_{p1}\left(12b_l - 6T_{d1} k_j\right) + 12b_m k_j + 12K_{d1} k_j + K_{i1}\left(k_j T_{d1}^2 - 6b_l T_{d1} + 12J_l\right) + 12b_l k_j N_j^{-2},$$

$$a_3 = K_{d1}\left(12b_l - 6T_{d1} k_j\right) + 12J_m k_j + 6T_{d1}\left(b_m k_j + b_l k_j N_j^{-2}\right) + 12b_l b_m + K_{p1}\left(k_j T_{d1}^2 - 6b_l T_{d1} + 12J_l\right) + K_{i1}\left(b_l T_{d1}^2 - 6J_l T_d\right) + 12J_l k_j N_j^{-2},$$

$$a_4 = 12J_l b_m + 12J_m b_l + 6T_{d1}\left(J_m k_j + b_l b_m + J_l k_j N_j^{-2}\right) + K_{d1}\left(k_j T_{d1}^2 - 6b_l T_{d1} + 12J_l\right) + T_{d1}^2\left(b_m k_j + b_l k_j N_j^{-2}\right) + K_{p1}\left(b_l T_{d1}^2 - 6J_l T_{d1}\right) + J_l K_{i1} T_{d1}^2,$$

$$a_5 = 6T_{d1}\left(J_l b_m + J_m b_l\right) + T_{d1}^2\left(J_m k_j + b_l b_m + J_l k_j N_j^{-2}\right) + K_{d1}\left(b_l T_{d1}^2 - 6J_l T_{d1}\right) + 12J_l J_m + J_l K_{p1} T_{d1}^2,$$

$$a_6 = T_{d1}^2\left(J_l b_m + J_m b_l\right) + 6J_l J_m T_{d1} + J_l K_{d1} T_{d1}^2,$$

$$a_7 = J_l J_m T_{d1}^2$$

The continuous-time first-stage, with rigid control only, as defined by Eq. (4.23), can be expressed in terms of its poles and zeros as follows:

$$G_1(s) = K_G \frac{\prod_{j=1}^{2}\left(s - z_j\right)\prod_{j=1}^{2}\left(s - \overline{z}_j\right)}{\prod_{j=1}^{5}\left(s - p_j\right)\prod_{j=1}^{2}\left(s - \overline{p}_j\right)} \tag{4.24}$$

where K_G is a gain factor, z_j and p_j are zeros and poles corresponding to low frequency dynamics near ω_z while $\bar{z}_j$ and $\bar{p}_j$ are zeros and poles corresponding to high frequency dynamics due to the presence of delays. With a digital motion controller, the delay is typically never greater than a few sampling time and high frequency dynamics is well separated from the low frequency dynamics. It is worth mentioning that when separating the dynamics, no conjugate pole and zero pair is broken. This is to guarantee that complex conjugates can be combined into a quadratic form such that the transfer function coefficients are always real. The gain factor K_G is computed to preserve the static gain of $G_1(s)$ in rational form as shown in (4.23).

The feedforward $F(s)$ is proposed based on a combination of three parts as follows:

$$F(s) = K_{Fs} \frac{\prod_{j=1}^{5}(s - p_j)}{\prod_{j=1}^{2}(s - z_j)} \frac{1}{\prod_{j=1}^{3}(s - \sigma_j)} \tag{4.25}$$

The first part of $F(s)$ is the gain factor K_{Fs}, which is computed such that $F(s)$ has unity static gain. The second part is the dominant inverse of $G_1(s)$, which includes poles p_j and zeros z_j corresponding to low frequency dynamics. The last part is an all pole low-pass filter with poles located at σ_j.

Since the dominant inverse of $G_1(s)$ has 5 zeros and 2 poles, the low-pass filter should have at least 3 poles to balance the number of pole and zero of the feedforward transfer function $F(s)$.

4.3.3 First-stage time-varying dynamics

In order to properly attenuate the flexible joint vibrations, it is very important that the zeros of

the first-stage feedforward transfer function cancel the dynamic poles of the first-stage rigid control loop. The natural frequency of the low frequency dynamic poles depends mainly on the effective joint stiffness, the motor inertia and the link inertia. As the robot's tool moves along an arbitrary path, the link inertias, and to a less extent, the joint coupling stiffness, vary. To maintain vibration attenuation, the feedforward transfer function needs to be time varied with new coefficients that match the time-dependent link inertia and coupling stiffness.

Given a robot configuration defined by the vector of reference joint position $\mathbf{r}$, the link effective inertias are computed very efficiently by using a recursive Newton-Euler formulation (Featherstone & Orin, 2000). Each joint's link inertia is computed by successive application of the inverse dynamics with the joint velocities set to zero, and with the joint accelerations set to zero or a unit vector.

In order to compute inertial forces acting on the links, it is necessary to compute the linear and rotational accelerations of the center of mass of each link at a given instant. This computation is done iteratively starting with the link j and moving successively link by link outward to last link n.

$$\begin{cases} \dot{\omega}_i = R_i^T \left(\dot{\omega}_{i-1} + \ddot{q}_i Z_{i-1} \right) & \text{if revolute} \\ \dot{\omega}_i = R_i^T \dot{\omega}_{i-1} & \text{if prismatic} \end{cases} \tag{4.26}$$

$$\begin{cases} \dot{v}_i = R_i^T \dot{v}_{i-1} + \dot{\omega}_i \times P_{i-1,i} & \text{if revolute} \\ \dot{v}_i = R_i^T \left(\dot{v}_{i-1} + \ddot{q}_i Z_{i-1} \right) + \dot{\omega}_i \times P_{i-1,i} & \text{if prismatic} \end{cases} \tag{4.27}$$

$$\dot{v}_{ci} = \dot{v}_i + \dot{\omega}_i \times P_{i,ci} \tag{4.28}$$

where $\dot{\omega}_i$ and $\dot{v}_i$ are the rotational and linear accelerations of link i, R_i is the rotation matrix from link i to $i-1$, $\ddot{q}_i$ is the joint i rotational acceleration, $P_{i-1,i}$ is the origin of link i in link $i-1$ coordinates and $P_{i,ci}$ is link i center of mass in link i coordinates. To compute link j accelerations, we set $\dot{\omega}_{j-1} = \dot{v}_{j-1} = 0$.

Having computed the accelerations, we can apply the Newton-Euler equations to compute the

inertial force and torque acting at the center of mass of each link and the joint torques being applied to each link. The Newton-Euler equations are evaluated link by link starting from last link n and working inward toward link j.

Inward iterations $i:\ n \to j$

$$\begin{aligned} f_i &= R_{i+1} f_{i+1} + m_i \dot{v}_c \\ n_i &= R_{i+1} n_{i+1} + I_i \dot{\omega}_i - f_i \times \left(P_{i-1,i} + P_{i,ci} \right) + R_{i+1} f_{i+1} \times P_{i,ci} \end{aligned} \tag{4.29}$$

where f_i and n_i are the force and torque exerted on link i by link $i-1$, m_i is the mass of link i and I_i is the inertia tensor of link i at its center of mass. Note that f_{n+1} and n_{n+1} are set to zero.

The torque τ_j on joint j is found by taking the Z component of the torque applied by its neighbor:

$$\begin{cases} \tau_j = \left(R_j^T n_j \right)^T Z_{j-1} & \text{if revolute} \\ \tau_j = \left(R_j^T f_j \right)^T Z_{j-1} & \text{if prismatic} \end{cases} \tag{4.30}$$

The link j inertia J_j is then obtained by dividing the joint torque by the joint acceleration used at the beginning of the procedure, i.e. $J_j = \tau_j / \ddot{q}_j$.

The coupling stiffness k_c can be estimated using an empirical function. For simplicity, a first-order model is used, where the coupling stiffness is expressed as a function of the link inertia.

At every sampling time, the link inertia and coupling stiffness are computed and the first-stage closed-loop, with rigid control only, $G_1(s)$ is updated. Then, the feedforward is recomputed based on the procedure expressed by Eqs. (4.23) to (4.25).

4.3.4 Second-stage PID compensator

The continuous PID compensator of the second-stage can be presented as:

$$C_2(s) = \frac{K_{d2}s^2 + K_{p2}s + K_{i2}}{s} = K_2 \frac{s^2 + 2\zeta_2\omega_{n2}s + \omega_{n2}^2}{s} \tag{4.31}$$

where ω_{n2} and ζ_2 are the angular natural frequency and the damping ratio of the numerator polynomial, and K_{p2}, K_{i2}, K_{d2} are the second-stage PID gains. The parameters K_2, ω_{n2} and ζ_2 can be expressed as follows:

$$K_2 = K_{d2},\ \omega_{n2} = \sqrt{\frac{K_{i2}}{K_{d2}}},\ \zeta_2 = \frac{K_{p2}}{2\sqrt{K_{i2}K_{d2}}} \tag{4.32}$$

By setting $\zeta_2 = 1$ to obtain critical damping responses (shortest settling time without oscillation), $\omega_{n2} = \lambda_2\omega_c$ where λ_2 is a dimensionless parameter and ω_c is the geometrical mean between ω_z and ω_P defined in (4.33), the responsiveness of the second-stage is tuned only with the gain K_{d2}. The gain K_{d2} is considered as a global gain that corresponds to the overall control performance trade-off between the response time and the overshoot.

$$\omega_c = \sqrt{\omega_z\omega_p} \tag{4.33}$$

4.3.5 Second-stage feedback filter

One aspect that must not be neglected for the second-stage loop is noise sensitivity. Two factors contribute to increase the noise sensitivity at high frequencies. Firstly, the quantization error of the second-stage position sensor can excite the delay poles of the first-stage. Secondly, the coupling transfer function $K(s)$ from the link position to the reducer output position sensor features a zero at the coupling natural frequency and amplifies the high frequency content.

These two factors severely restrict the stability margin and the load rejection of the second-stage. One way to alleviate the problem is to insert a low-pass filter in the feedback path. The filter $H_2(s)$ is designed using a n^{th}-order Butterworth filter since it provides maximum flatness of the frequency response and a high-frequency roll-off of $20n$ dB/decade. The order and cut-off frequency are selected to provide enough attenuation at the frequency of the delay poles, while leaving the flexible joint dynamics frequencies undisturbed.

The transfer function of the Butterworth filter with a unit cut-off frequency is:

$$\left|H_2(j\omega)\right| = \frac{1}{\sqrt{1+\omega^{2n}}} \tag{4.34}$$

The *n* poles of the filter lie on a unit circle at equally spaced point, and symmetric around the negative real axis. The *k*-th pole is specified by

$$s_k = e^{\frac{j(2k+n-1)\pi}{2n}} \quad \text{with } k = 1, 2, 3, \ldots, n \tag{4.35}$$

4.3.6 Second-stage generalized Smith predictor

A low-pass filter must be inserted into the second-stage loop feedback path to prevent the sensor noise from exciting the first-stage delay poles. One disadvantage of feedback filtering is the additional phase lag that is introduced. This phase lag and the loop delay reduce the gain margin.

The Smith predictor (J. M. Smith, 1957) can be considered as the first predictor-based control for linear systems with time delay. For our application, the group delay of the low-pass filter at low frequency is typically much higher than the time delay. This leads us to generalize the predictor concept to an arbitrary feedback transfer function.

First, the first-stage with input shaping feedforward seen at the reducer output position output can be computed as follows:

$$P_1(s) = \frac{q_r(s)}{r_{is}(s)} = F(s)G_1(s)K(s) \tag{4.36}$$

The transfer function $P_1(s)$ can be regarded as the plant for the second-stage. If no filter and delay are placed in the feedback path, the second-stage closed loop transfer function is:

$$G(s) = \frac{C_2(s)P_1(s)}{1 + C_2(s)P_1(s)} \tag{4.37}$$

where $C_2(s)$ is a satisfactory PID compensator.

In the presence of feedback filter and delay, the second-stage closed-loop transfer function becomes:

$$\hat{G}(s) = \frac{\hat{C}_2(s)P_1(s)}{1 + \hat{C}_2(s)P_1(s)H_2(s)D_2(s)} \tag{4.38}$$

where $\hat{C}_2(s)$ is a compensator to be defined.

The objective is to design a compensator $\hat{C}_2(s)$ such that the second-stage closed-loop transfer function remains unchanged in the presence of a feedback filter and delay as follows:

$$\hat{G}(s) = G(s) \tag{4.39}$$

Substituting Eqs. (4.37) and (4.38) into Eq. (4.39), and solving for $\hat{C}_2(s)$ gives:

$$\hat{C}_2(s) = C_2(s)\underbrace{\frac{1}{1 + C_2(s)P_1(s)\left[1 - H_2(s)D_2(s)\right]}}_{S(s)} \tag{4.40}$$

The transfer function $\hat{C}_2(s)$ is the combination of $C_2(s)$ and the transfer function $S(s)$, which is the so-called generalized Smith predictor.

4.3.7 Discrete-time implementation

In the previous sections, the proposed controller is designed in the continuous-time domain. However, most industrial robots use digital controllers to perform joint position control. Therefore, for implementation purpose, a discretization of the control approach needs to be conducted.

When converting the feedforward transfer function from the continuous domain to the discrete domain, it is then of paramount importance to preserve the frequency response near the flexible joint dynamics frequencies. For that purpose, the bilinear transform with frequency warping is used. The pre-warping frequency of continuous poles and zeros is performed at a central frequency ω_c, which is the geometrical mean between ω_z and ω_p of the $M(s)$ transfer function, as shown in Eq. (4.33). This ω_c is very close to the crossover frequency of the motor transfer function $M(s)$ for unity gain. The frequency ω_c is pre-warped into an analog angular frequency Ω_c as follows:

$$\Omega_c = \frac{2}{T_s}\tan\left(\frac{\omega_c T_s}{2}\right) \tag{4.41}$$

where T_s is the sampling time.

For each pole and zero of the continuous-time feedforward transfer function $F(s)$, the following pre-warp frequency transformation is applied:

$$s \leftarrow \frac{s}{\Omega_c} \tag{4.42}$$

The bilinear transform is used to map the continuous-time domain to the discrete-time domain as follows:

$$z = \frac{2 + sT_s}{2 - sT_s} \tag{4.43}$$

The discrete-time feedforward transfer function can be written as follows:

$$F(z) = K_{Fz} \frac{\prod_{j=1}^{5} (z - z_j)}{\prod_{j=1}^{5} (z - p_j)} \tag{4.44}$$

where K_{Fz} is the gain factor, which is obtained by matching the magnitude of the analog and discrete transfer function at ω_c, and z_j and p_j are zeros and poles of the discrete-time transfer function computed by applying Eq. (4.43) to the continuous-time zeros and poles.

The bilinear approximation with frequency warping is used to obtain the discrete versions of all continuous transfer functions that are needed for the implementation of the control method, except for the PID compensators. Although bilinear approximation with frequency warping is widely used to preserve the frequency response, it cannot be used to obtain a discrete PID transfer function. If bilinear approximation is used, it leads to two poles on the unit circle and thus a marginally stable transfer function. The backward difference approximation is used to discretize the PID compensator instead. Substituting the backward difference approximation $s = (z-1)/T_s z$ into Eq. (4.19) yields:

$$C_1(z) = \frac{\left(K_{p1} + K_{i1}T_s + K_{d1}/T_s\right) - \left(K_{p1} + 2K_{d1}/T_s\right)z^{-1} + \left(K_{d1}/T_s\right)z^{-2}}{1 - z^{-1}} \tag{4.45}$$

where T_s is the sampling time.

At low frequencies, the discrete transfer function matches well the continuous transfer function, but at frequencies above 10% of the sampling frequency it stops following its continuous counterpart, and a large phase distortion is observed. For instance, at high frequencies, the derivative term is dominant and the phase of the continuous transfer function is close to 90 degrees and the group delay is zero. For the discrete version, at the Nyquist frequency, the phase becomes zero and the group delay is not zero.

Due to the phase mismatch between continuous and discrete rigid controllers, the continuous closed-loop transfer function $G_1(s)$ overestimates the frequency of the delay poles, resulting in an overestimated gain margin.

To remedy this situation, a simple but effective approach is to tweak the feedback delay value such that the frequencies of delay poles in the continuous and discrete models are matched. To this end, the feedback delay in the continuous rigid control loop $G_1(s)$ is defined as:

$$T_{d1} = T_{fb1} + T_w \tag{4.46}$$

where T_{fb1} is the actual motor feedback delay and T_w is the compensated distortion delay computed from the group delay of the $C_1(z)$ at $\omega = \pi / T_s$, as shown in (4.47):

$$T_w = -\frac{d}{d\omega} \angle C_1\left(e^{j\omega T_s}\right) \text{ at } \omega = \frac{\pi}{T_s} \tag{4.47}$$

An example is given to illustrate the effect of PID phase distortion on the first-stage rigid control. Parameters used for the simulation are $J_l = 10.74\,\text{kgm}^2$, $J_m = 2.65\times10^{-4}\,\text{kgm}^2$, $k_j = 14.66\times10^3$ Nm/rad, $k_r = 12\times10^4$ Nm/rad, $k_c = 14.65\times10^3$ Nm/rad, $N_r = 160$, $b_l = 24.74$ Nms/rad, $b_m = 9.46\times10^{-4}$ Nms/rad, $\lambda_1 = 2.3$, and $T_{fb1} = 2$ ms.

As shown in Figure 4.7, at Nyquist frequency, there is a difference of 0.4849 ms between the

group delays of continuous and discrete PID controllers, which is about half of the sampling time of 1ms. This difference causes frequency modelling errors of the closed-loop system, as shown in Figure 4.8. Note that a discrete closed loop $G_1(z)$ is directly computed using discrete versions of the flexible joint dynamic model and integer delay. An actual delay frequency of 84.36 Hz is computed from the discrete closed loop $G_1(z)$. Without the distortion compensation, the continuous model provides a delay frequency of 100.38 Hz, which is overestimated by about 19%. With the distortion compensation, i.e. $T_w = 0.4849$ ms, the continuous model provides a delay frequency of 86.63 Hz, which is only about a 2.7% mismatch versus the delay frequency computed from the discrete-time model.

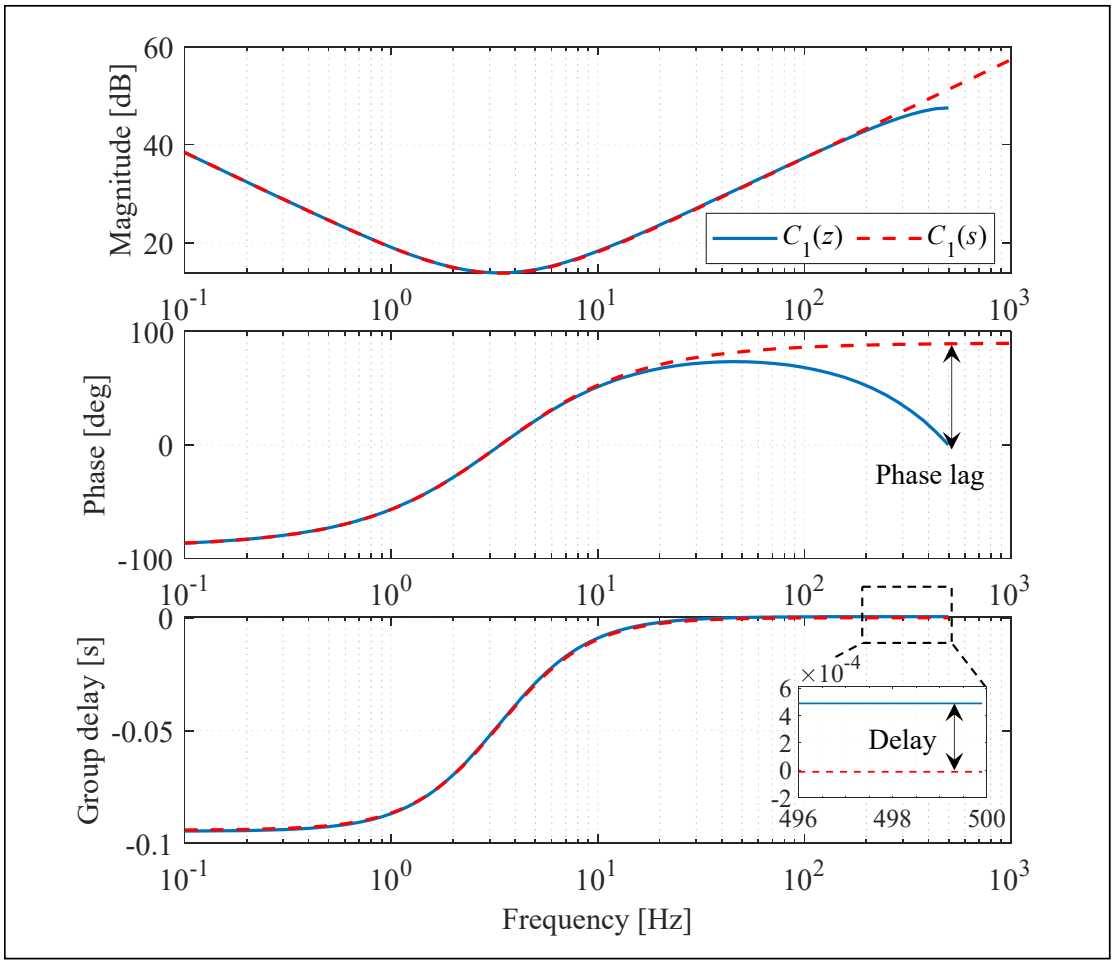

Figure 4.7 Phase lag and delay induced by discrete PID distortion at high frequencies

It should be mentioned that although the discrete version of the closed-loop $G_1(z)$ is available, it should not be used to design the feedforward. This is because the numerical computation of $G_1(z)$ may require order reduction, which introduces difficulties for pole-zero selection and time-varying dynamics of the feedforward.

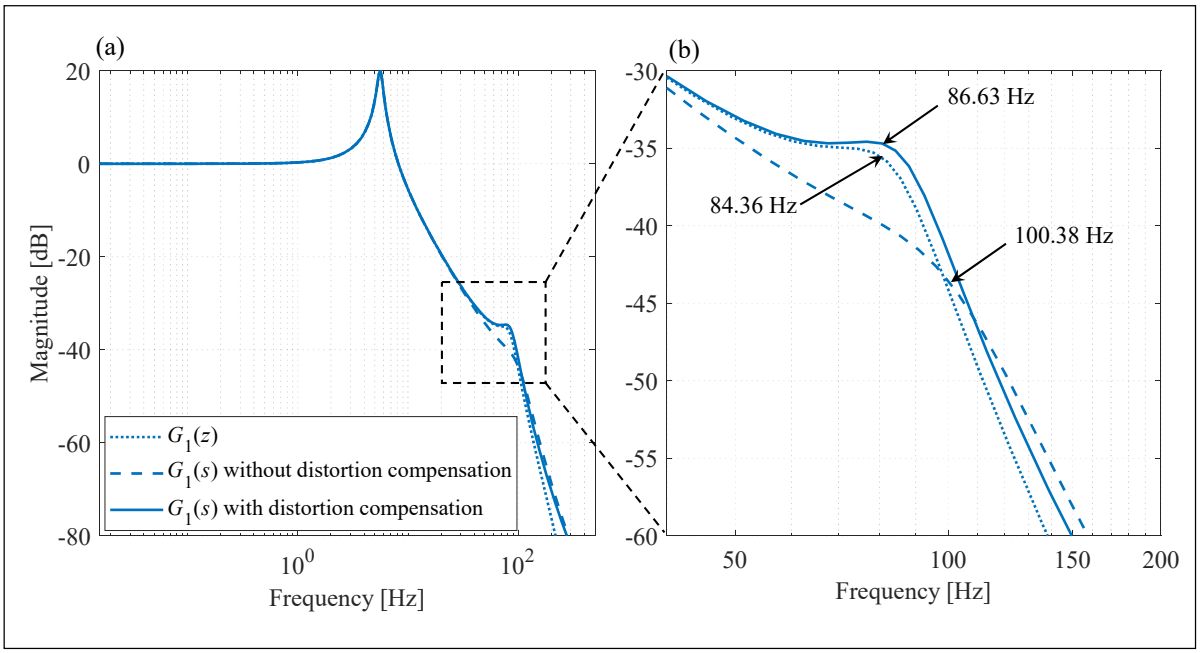

Figure 4.8 (a) Frequency response of the closed-loop G_1 with and without PID distortion compensation; (b) Zoomed-in of selected portion according to delay frequency

4.3.8 Stability analysis

The advantage of increasing the gain parameter λ_1 of the PID compensator C_1 is that it improves the rejection of disturbances, such as external torques or nonlinear frictions. However, λ_1 should not be increased up to the point where flexible dynamics of the link are excited. With input shaping control, the parameter λ_1 can be boosted up since the link vibration is attenuated by the feedforward. Now, there are two other factors that bound the magnitude of λ_1. The first is the level of confidence in the model parameters. The presence of model

mismatches, which is very common in practice, can deteriorate the feedforward performance if a too high λ_1 is selected. Consequently, the higher the model confidence, the higher the gain can be set. The second factor is the feedback delay, which introduces a conjugate pole pair at high frequencies (see Eq. (4.24)). The feedback delay sets a limit on gains, above which the closed loop becomes unstable. The value of the parameter λ_1 that results in an unstable system can be numerically found by solving the closed loop characteristic equation of $G_1(z)$ as follows:

$$1+C_1(z)M(z)D_1(z)=0 \tag{4.48}$$

A simulation study is realized to illustrate the stability of $G_1(z)$ with respect to the parameter λ_1. Parameters used for the simulation are similar to those in section 4.3.7, with the parameter λ_1 varying from 1.9 to 3.7, and the low-pass filter inside the feedforward being a third-order Butterworth low-pass filter with a cutoff frequency at the crossover frequency of 7.45 Hz.

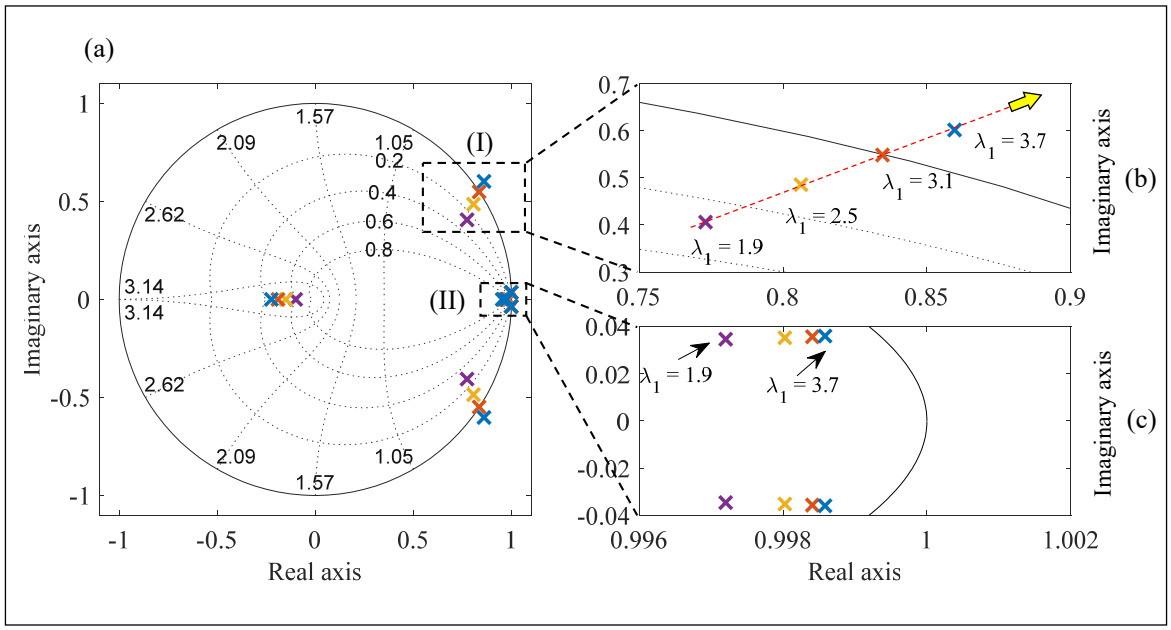

Figure 4.9 (a) Pole locus of closed-loop model $G_1(z)$ with increasing λ_1, (b) Zoomed-in of region I: delays dynamics, (c) Zoomed-in of region II: flexible joint dynamics

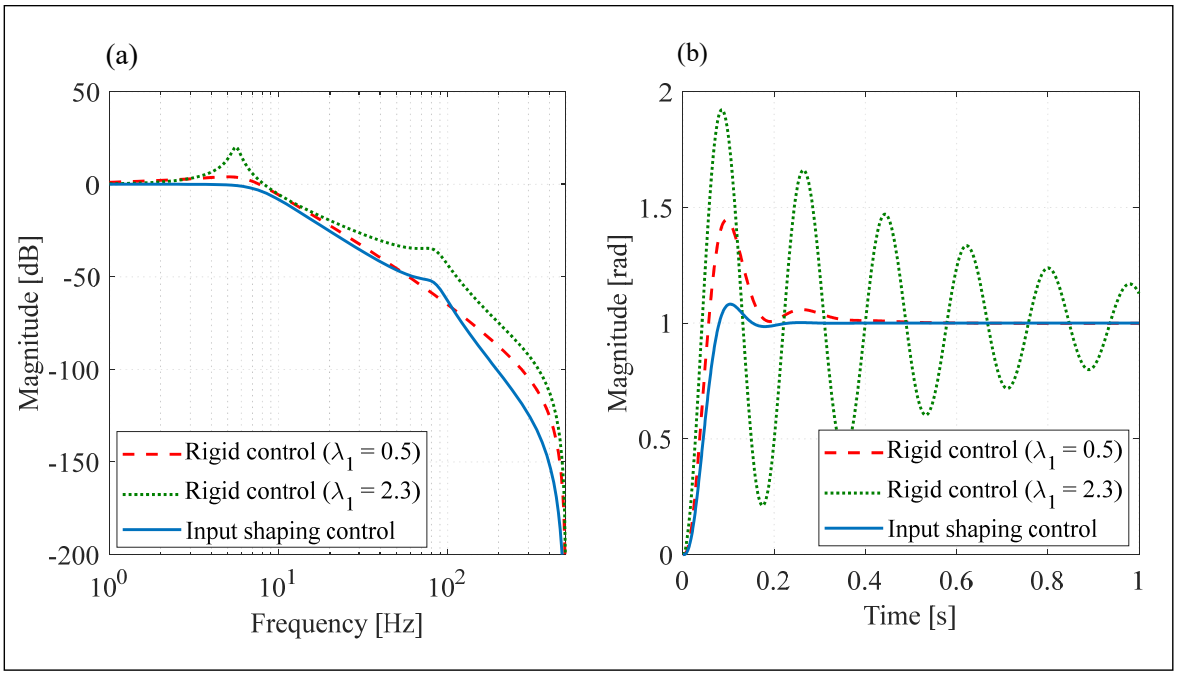

Figure 4.10 (a) Frequency response and (b) step response of the first-stage rigid control versus the first-stage input shaping feedforward control

The pole locus of the first-stage, with rigid control only, is depicted in Figure 4.9. Increasing λ_1 may cause flexible joint poles to approach the unit circle (see Figure 4.9 (c)) and cause delay poles to be out of the unit circle (see Figure 4.9 (b)). In addition, the motor torque gets noisier when delay poles move towards the unit circle. This noise develops even much faster when the motor position encoder quantization error is taken into account. Therefore, to maintain a margin for model mismatches and to avoid torque fluctuation or even saturation, λ_1 should not exceed 75% of the value that leads the closed loop to instability. A typical response of the first-stage rigid control (with $\lambda_1 = 0.5$ and $\lambda_1 = 2.3$) versus the input shaping control is shown in Figure 4.10. Note that the input shaping control refers to the first-stage with rigid control (with $\lambda_1 = 2.3$) and input shaping feedforward enabled. It can clearly be seen that the first-stage rigid control with higher value of λ_1 reduces rising time, but induces large vibrations. The input shaping control significantly reduces the vibration.

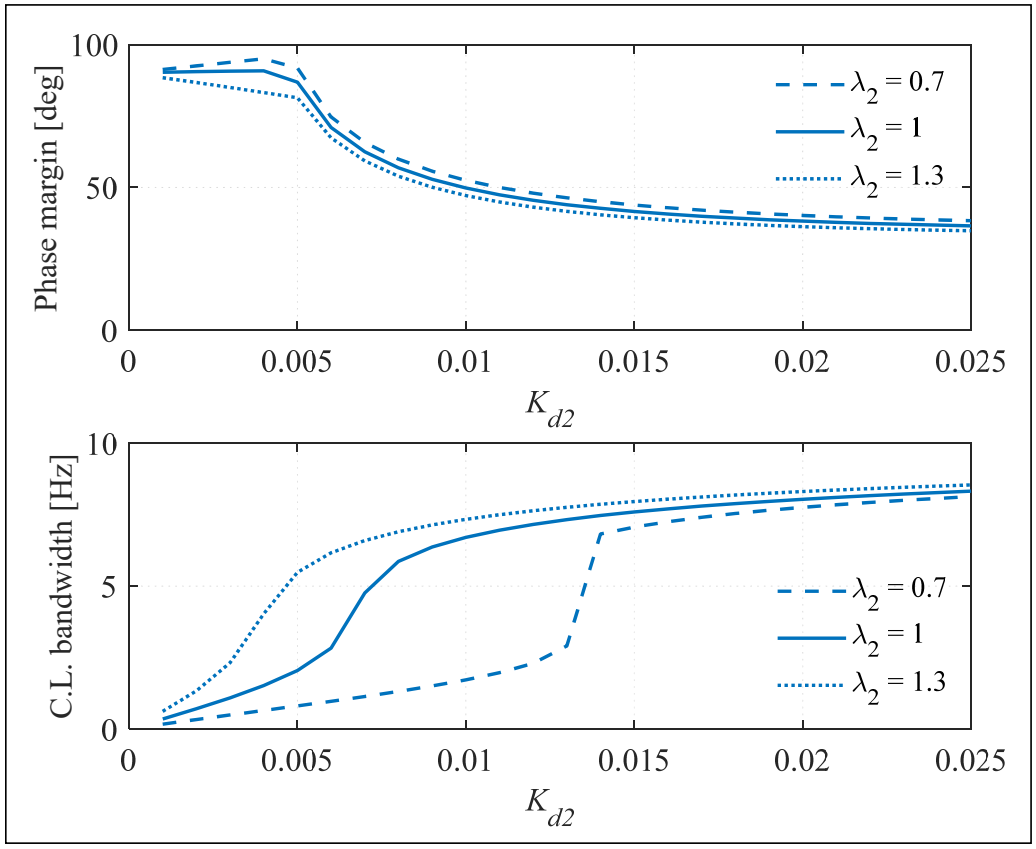

Figure 4.11 Phase margin and closed-loop bandwidth of the two-stage control with increasing K_{d2}

The stability of the second-stage is determined based on an analysis of the second-stage open loop defined as:

$$O_2(z) = C_2(z)S(z)P_1(z) \tag{4.49}$$

where $P_1(z)$ is the plant for the second-stage, which is computed by discretizing $P_1(s)$ in Eq. (4.36). A typical trend of the phase margin and closed-loop 3db bandwidth with increasing global gain K_{d2} with different λ_2 is shown in Figure 4.11. Increasing λ_2 leads to a higher control bandwidth, but a lower phase margin. The value $\lambda_2 = 1$ is recommended, which

compromises between the bandwidth and the phase margin. To avoid inducing too much vibration in the link response, K_{d2} should be selected to obtain a phase margin of at least 70 degrees.

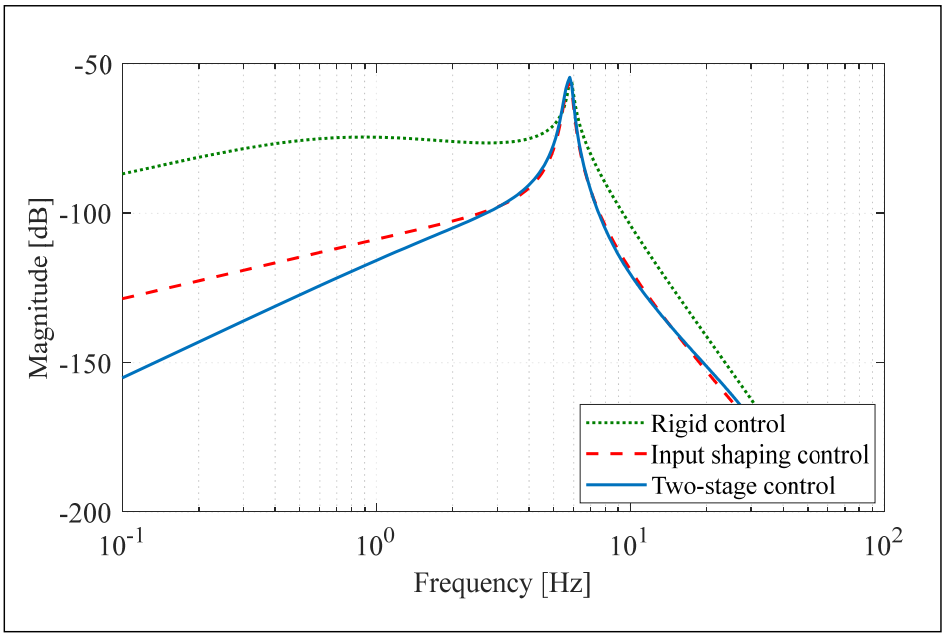

Figure 4.12 Load disturbance rejection with three controllers: Rigid control, Input shaping control, and Two-stage control

An important quality of the proposed controller is its capacity to reject torque disturbance at the link inertia. The load disturbance transfer function is defined from the link torque disturbance d_l to the link position q_l. Figure 4.12 shows the simulated frequency responses of the load disturbance transfer function for three control approaches: Rigid control (with $\lambda_1 = 0.5$), Input shaping control (with $\lambda_1 = 2.3$) and Two-stage control (with $\lambda_1 = 2.3$ and $K_{d2} = 0.0075$). It is clearly seen that the proposed input shaping control and two-stage control provide a much higher disturbance rejection at low frequencies. This is due to the use of a higher gain in the first-stage and the addition of the second-stage.

However, the input shaping control, and even the two-stage control do not provide any more disturbance rejection near resonance frequency. This implies that torque disturbances with frequency content near resonance frequency generate vibrations. This is a shortcoming of the input shaping approach. Such disturbances may arise from external forces at the effector, or from internal coupling inertial, Coriolis and centrifugal torques.

Another important quality of the proposed controller is the reducing of high frequency sensor noise effects. The noise reduction is evaluated using the noise sensitivity function, which is defined from the second-stage feedback noise η_r to the motor torque u . Figure 4.13 shows the frequency response of the sensitivity functions of the system using the two-stage control with the second-stage (fourth order Butterworth) low-pass filter enabled and disabled.

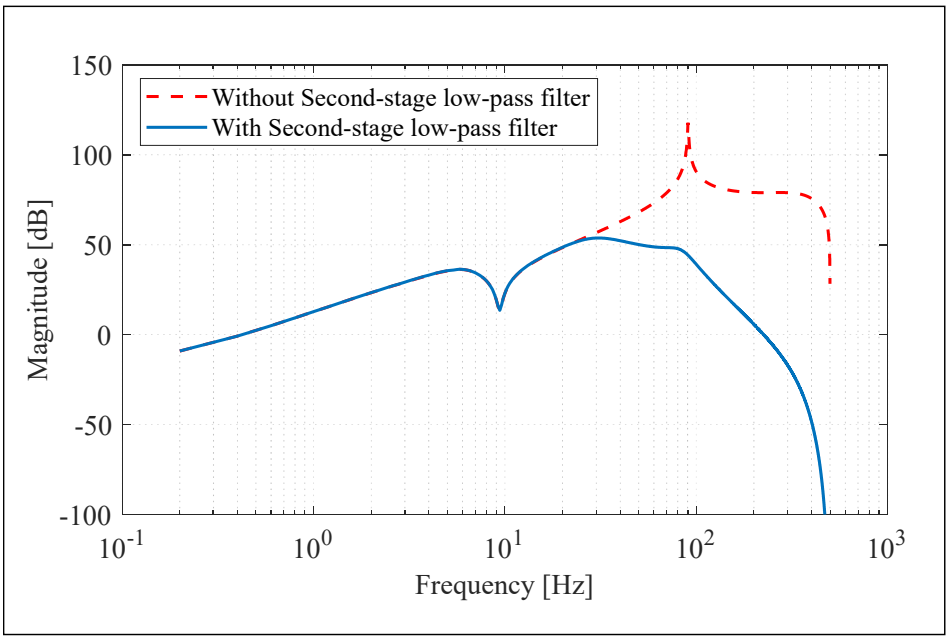

Figure 4.13 Frequency responses of the sensitivity function of the system using Two-stage control with and without the second-stage low-pass filter

As shown in Figure 4.13, for the frequencies less than the low-pass filter cut-off frequency (25 Hz), the sensitivity functions with the low-pass filter enabled or disabled are similar. However,

for higher frequencies, without the second stage low-pass filter, the sensor noise is significantly amplified at the resonance of 84.36 Hz due to the delay dynamics. This noise, if not compensated, may cause the fluctuation or even the saturation of the motor torque. With the second stage low-pass filter enabled, the control performance is much improved since the resonance is effectively attenuated by 70 dB and the magnitude near the Nyquist frequency is reduced by about 150 dB.

4.3.9 Model mismatch sensitivity analysis

In this section, we consider the more general case in which model mismatches exist. In practice, it is very difficult or almost impossible to obtain exact dynamic models due to the inadequacy of linear time-invariant modelling, nonlinear effects, or time-varying robot configurations. A general requirement of a control system is that it should provide a certain level of robustness, even in the presence of modelling errors.

The following observations are drawn from the analysis of the control performance:

1) The performance of the input shaping control is highly dependent on how well the link resonance frequency is modelled. This frequency is obtained from a conjugate pole pair of the seventh-order closed-loop G_1. The frequency of these poles is sensitive to the effective joint stiffness k_j and link inertia J_l. Since the link inertia J_l can be obtained quite accurately, the modelling error of k_j becomes the main source of oscillation frequency modelling uncertainty.

2) Modelling errors of damping have a smaller effect on vibration control performance than that from frequency modelling error. Large errors in the damping coefficients do not produce very big differences in the link response with feedforward.

To illustrate the effect of the stiffness mismatch, numerical simulations are performed. The parameters used for the simulations are similar to those in the section 3.8, with modelling errors added. Figure 4.14 shows the link position response of the input shaping control with effective joint stiffness modelling errors varying within ±20%. This large error induces a lump and a bump in the frequency responses near the link resonance frequency, which deteriorates the tracking performance. However, input shaping control still improves the tracking performance and vibration rejection as compared to the use of the first-stage rigid control alone (see Figure 4.10), even in the presence of large modelling errors.

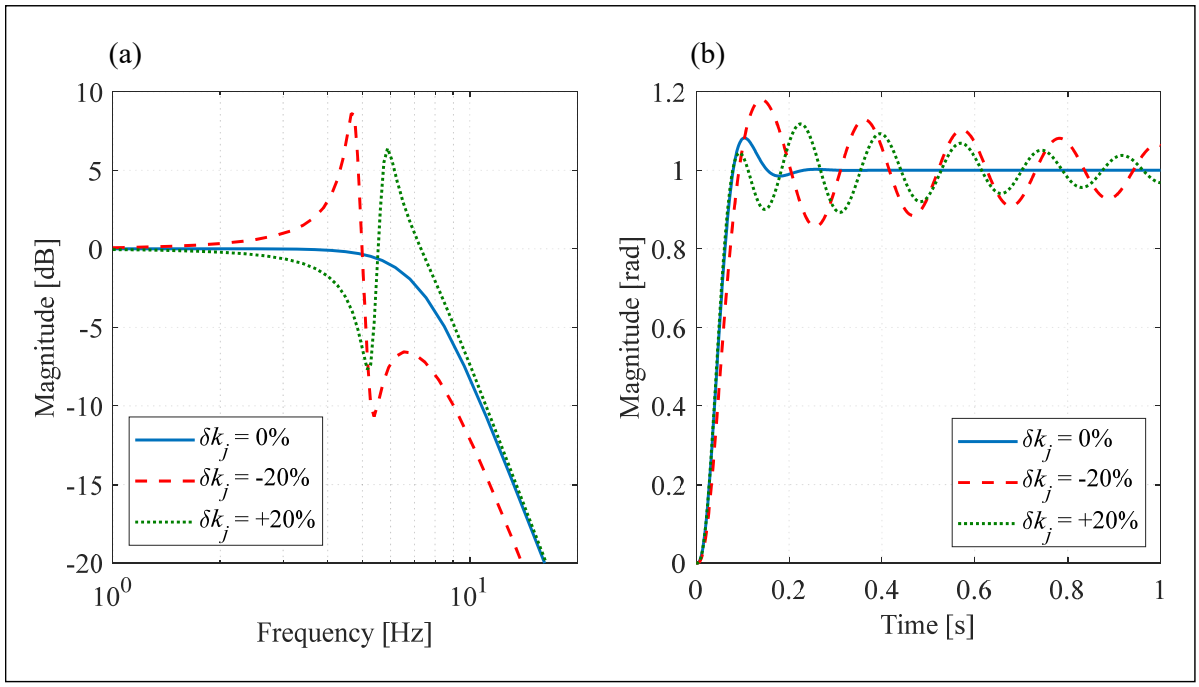

Figure 4.14 (a) Frequency response and (b) step response of the first-stage feedforward control with large modelling errors

Figure 4.15 shows the phase margin and 3dB closed-loop bandwidth of the two-stage control with large modelling errors, with up to a ±20% mismatch of effective joint stiffness k_j. It can

clearly be seen that the system is still stable, but the phase margin and closed-loop bandwidth may vary significantly if a high K_{d2} is selected.

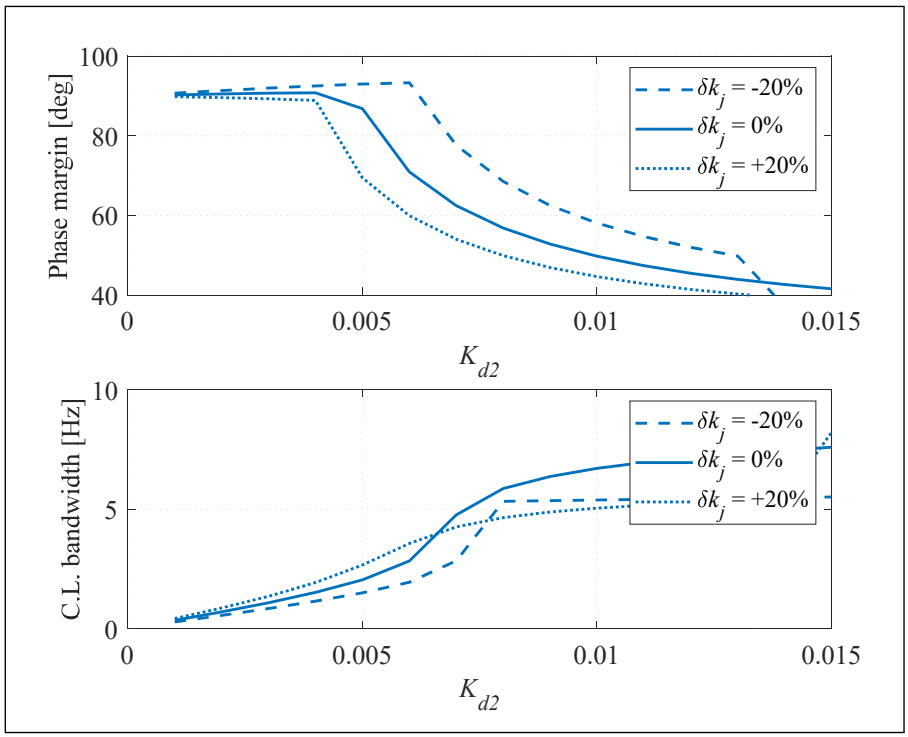

Figure 4.15 Phase margin and closed-loop bandwidth of two-stage control with large modelling errors

4.3.10 Parameter identification technique

Since the feedforward is designed using the inverse closed-loop model, all parameters that appear in the differential equations of the closed-loop $G_1(s)$ need to be known. These parameters include flexible joint parameters J_l, J_m, b_l, b_m, k_r, k_j, and N_r.

Based on the mass distribution and density of every part of the manipulator from the CAD model, a recursive Newton-Euler allows computing the link effective inertia J_l with regard to robot configurations. The CAD model can also be used to obtain the motor inertia J_m. The reducer stiffness k_r and gear ratio N_r can be obtained from component specifications. The motor friction b_m can be obtained from specifications of motor bearings and motor iron losses, and the link friction b_l can be estimated from the reducer efficiency.

Theoretically, rigid controller gains (K_{p1}, K_{i1}, and K_{d1}) are known precisely. However, if the proposed control approach is retrofitted into existing robots, it should be ensured that built-in rigid control gains are available.

Once the above parameters are obtained, the effective joint stiffness k_j is identified. If the torque command is available, the motor open-loop transfer function can be obtained. Then, the joint stiffness k_j can be identified by fitting open-loop frequency response curves (S. Oh & Kong, 2017; Pham, Hamelin, et al., 2019). Note that to obtain frequency responses accurately, excitations should be performed at many different frequencies. If only the access to the reference profile is available, as is the case for industrial robots with built-in joint controllers, the effective joint stiffness k_j cannot be easily extracted from closed-loop frequency responses. Therefore, a method to identify the effective joint stiffness k_j using temporal responses is needed. Compared to identification using frequency responses, the identification using temporal responses presents the advantage of being very fast since only one test is required.

A discrete energy separator algorithm (DESA) is used to find the instantaneous frequency and envelope of a temporal response signal (Maragos, Kaiser, & Quatieri, 1993). Before applying DESA, the signal goes through a band-pass filter to retain the frequency content near the estimated resonance frequency. A fourth order Butterworth filter with a 4 Hz bandwidth gives good results.

To separate the induced vibration from reference transient harmonics, an instantaneous frequency and envelope can be found by applying DESA to the time inverse response data. The instantaneous frequency can be extracted as shown in (4.50):

$$\hat{\Omega}(n) = \hat{\omega}(n)T_s = \arccos\left(1 - \frac{\Psi[\bar{y}(n)] + \Psi[\bar{y}(n+1)]}{4\Psi[\bar{x}(n)]}\right) \tag{4.50}$$

where $\hat{\omega}(n)$ is the instantaneous angular frequency, $\bar{x}(n)$ is the band-pass filtered time inverse temporal response signal, $\bar{y}(n) = \bar{x}(n) - \bar{x}(n-1)$, n is the sample index, and Ψ is the discrete-time Teager energy operator defined as:

$$\Psi[x_n] = \frac{x_n^2 - x_{n-1}x_{n+1}}{T_s} \tag{4.51}$$

where T_s is the sampling time, and x is the input signal.

A fourth order low-pass Butterworth filter is used for smoothing the instantaneous frequency signal. The low-pass filter cutoff frequency is set to twice the value of the band-pass filter bandwidth. The vibration frequency $\bar{\omega}$ can be found as the mean of the low-pass filtered $\hat{\omega}(n)$ about its steady state. If the obtained vibration frequency differs too much from the initial estimate used to set the band-pass filter central frequency, the identification procedure can be repeated with an updated central frequency estimate. Figure 4.16 shows a frequency identification example using a time inverse temporal response signal. For 1000 samples during the vibration decay period, the standard deviation using the original signal is 0.54 Hz. It is difficult to obtain a stable frequency average since the instantaneous frequency varies significantly (see Figure 4.16(a), bottom figure). When the time inverse signal is used (see Figure 4.16(b), bottom figure), the instantaneous frequency stabilizes quickly and the standard deviation is reduced by 56% to only 0.24 Hz.

Then, a numerical optimization procedure based on the Secant method is conducted to find the effective joint stiffness k_j such that the closed-loop model $G_1(s)$ can provide the identified

vibration frequency. The effective joint stiffness based on previous iterations as shown in (4.52)

$$k_j(i+2) = k_j(i+1) - \Delta\omega(i+1)\frac{k_j(i+1) - k_j(i)}{\Delta\omega(i+1) - \Delta\omega(i)} \tag{4.52}$$

where $\Delta\omega = \omega_{G_1} - \bar{\omega}$ with ω_{G_1} is the frequency of the conjugate poles of G_1 according to the flexible joint vibration, $\bar{\omega}$ is the identified vibration frequency, and i is number of iteration. Once k_j is identified, the coupling stiffness k_c can be computed using (4.8).

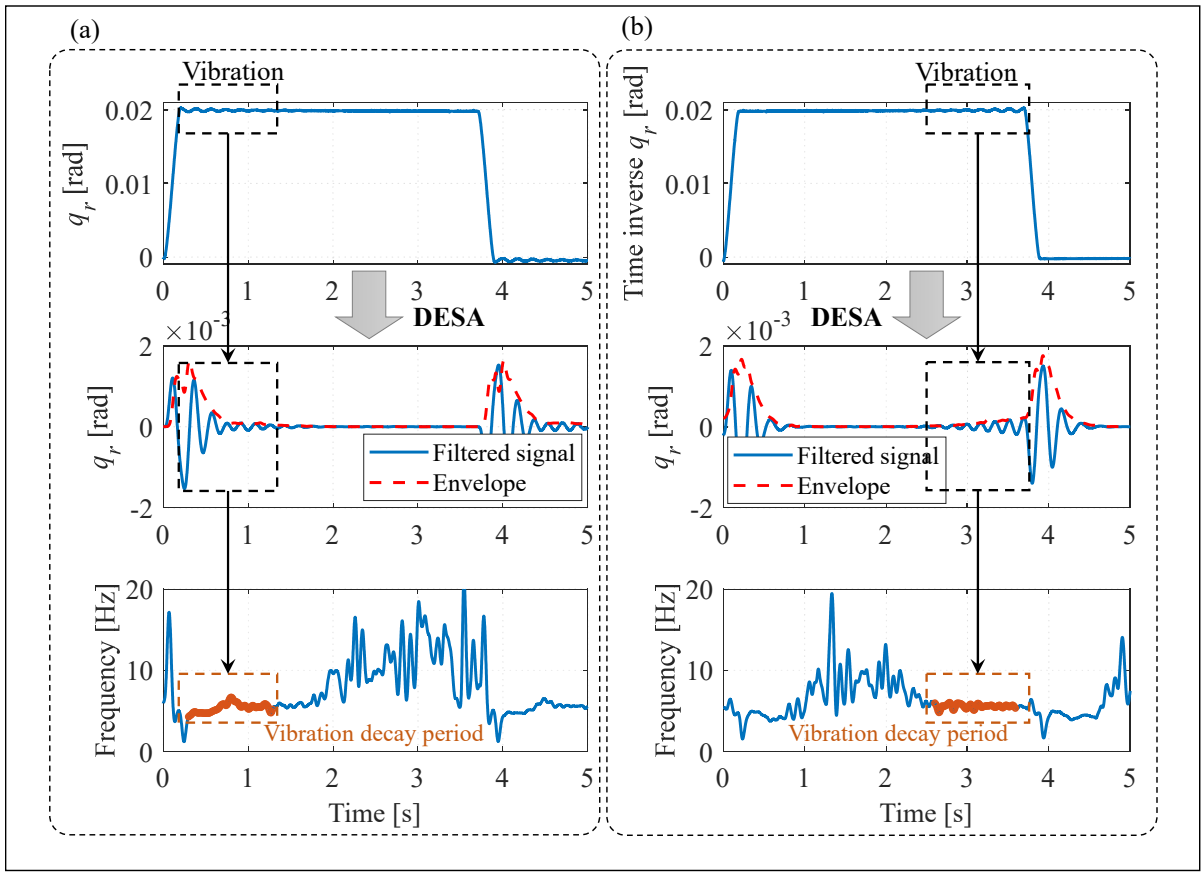

Figure 4.16 Frequency identification from experimental data: (a) Identified from the original signal, (b) Identified from the time inverse signal

In the following, the identification of delays is presented. The identification of feedback time delay requires access to motor torque measurement, which can be estimated from the motor current signal. A discrete numerical simulation of the first-stage, with rigid control only, is conducted. A high value of λ_1 is selected such that the delay pole is excited. Then, the simulation feedback delay is tuned to allow closely matching of simulated and measured FFT of the motor torques. The delays from motor side and link side measurements are assumed to be equal, since these two signals come from the same motion drive.

4.3.11 Multiple joint synchronization

It is not necessary to apply the proposed input shaping techniques to each joint first-stage controller. Typically, only the joints near the base of the kinematic chain need the first-stage input shaping since they exhibit significant vibrations in their response. For instance, the link inertia of the joints becomes smaller as the joint approaches the end of the kinematic chain. This results in higher dynamics frequencies and lower vibration amplitudes. Eventually, the vibration level is smaller than the resolution of the link position sensor, at which point it is no longer required, or feasible, to compensate for it. In that case, a second-stage is still desirable, but without the first-stage feedforward.

The position control of an individual joint from a decentralized perspective has been considered to this point. Nevertheless, to achieve precise Cartesian position control, it is important that all joint positions be synchronized. When enabled, the input shaping feedforward adds a non-negligible group delay to the low frequency response of the first-stage controller. This creates a distortion of the desired trajectory in the Cartesian space if not compensated.

We propose to use an all-pass fractional delay filter in place of the feedforward when the feedforward is not required. The fractional delay is adjusted as the average static group delay of all the input shaping feedforward transfer functions.

Such a digital all-pass filter, with exactly flat magnitude response, can be directly designed in the Z-plane as follows:

$$H(z) = \frac{z^{-n} D\left(z^{-1}\right)}{D(z)} \tag{4.53}$$

with $$D(z) = 1 + a_1 z^{-1} + a_2 z^{-2} + \ldots + a_n z^{-n}$$

where n is the order of the filter and $D(z)$ is the denominator polynomial with real value coefficients a_k, and the numerator polynomial is a reverse version of the denominator. The Thiran method (Thiran, 1971) is used to obtain a maximally flat group delay. The following design formula is used to compute the polynomial coefficients:

$$a_k = (-1)^k \frac{N!}{(N-k)!k!} \prod_{n=0}^{N} \frac{d+n}{d+k+n} \tag{4.54}$$

where D is the fractional delay and $d = D - N$ is the real value delay parameter. The denominator polynomial has all roots inside the unit circle for $d > -1$. Typically, a fourth order is enough to provide flat group delay inside the closed-loop bandwidth.

4.4 Experiment

In this section, experiments are conducted to validate the effectiveness of the proposed control approach.

4.4.1 Experimental setup

The experimental test bench is an industrial six-joint serial robot system named SCOMPI currently under development at Hydro-Québec's Research Institute, as shown in Figure 4.17. It includes a track-based robot manipulator, a controller, and a teach pendant. A grinding tool

is mounted on the robot end effector. The robot is installed on a vertical track.

Each joint actuator uses a synchronous permanent magnets motor controlled by an embedded Elmo whistle motion drive. The motor torques is amplified by a harmonic drive reducer. Joint angular positions are captured by a custom Timken magnetic encoder with 13-bit resolution on the motor and a Netzer DS-58 absolute encoder with 18-bit resolution on the reducer output.

The high-level control algorithm is implemented in C++ and runs under a real-time Linux operating system with a loop cycle time of 1 ms. The robot controller communicates with the embedded motion drives via the EtherCAT protocol. The main specifications of the robot are given in Table 4.1 to Table 4.3.

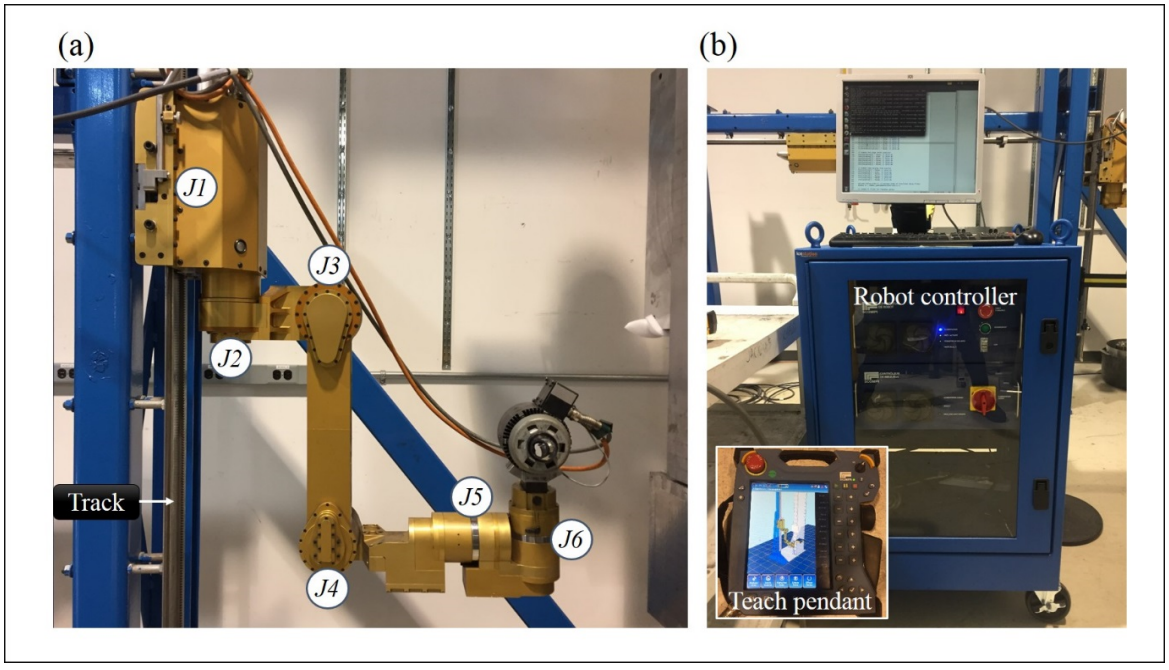

Figure 4.17 Experimental testbed: (a) the industrial six-joint SCOMPI robot manipulator with embedded joint controllers; (b) the robot controller and the teach pendant

Table 4.1 Joint specifications

	Joint 1	Joint 2	Joint 3	Joint 4	Joint 5	Joint 6
N_r	51	160	160	160	160	160
J_m [10^{-4}kgm^2]	1.71	2.65	2.42	1.26	0.91	0.86
J_l [kgm^2]	4.27	2.87 - 10.74	3.65 - 6.70	1.33 - 1.35	4.316	2.53
k_j [kNm/rad]	N/A	7.49 - 14.66	18.33 - 21.36	3.34 - 8.34	N/A	N/A
k_r [kNm/rad]	25	120	120	57	29	29
b_m [10^{-4} Nms/rad]	9.46	9.46	9.46	9.46	5.90	5.90
b_l [Nms/rad]	2.73	24.74	5.67	9.37	8.74	8.74

Table 4.2 Mass distribution

	Link 1	Link 2	Link 3	Link 4	Link 5	Link 6	Tool
m [kg]	19.0	5.723	5.166	4.425	3.302	1.022	4.026
Pc_x [m]	0.021	-0.054	-0.138	0.011	0	-0.004	-0.002
Pc_y [m]	0.031	0.003	0	0.012	-0.026	0.039	0.005
Pc_z [m]	-0.226	0.014	-0.019	0.161	-0.022	0	0
I_{xx} [kgm^2]	0	0.010	0.008	0.044	0.012	0.001	0.007
I_{yy} [kgm^2]	0	0.044	0.160	0.044	0.006	0.001	0.007
I_{zz} [kgm^2]	0	0.043	0.160	0.008	0.008	0.012	0.008
I_{xy} [kgm^2]	0	0.003	0	0	0	0	0
I_{xz} [kgm^2]	19.0	5.723	5.166	4.425	3.302	1.022	4.026
I_{yz} [kgm^2]	0.021	-0.054	-0.138	0.011	0	-0.004	-0.002

m : mass Pc : Center of mass I : Moment of inertia at the center of mass

Table 4.3 Denavit-Hartenberg parameters

	Joint 1	Joint 2	Joint 3	Joint 4	Joint 5	Joint 6
q_i [deg]	90°	q_2	q_3	q_4	q_5	q_6
α_i [deg]	0°	90°	0°	90°	90°	–90°
a_i [m]	0	0.192	0.042	0	0	0
d_i [m]	q_1	0	0	0	0.38	0

The robotic arm is a chain of links vibrating at different levels. The joints with indices 2-4 are about the base of the kinematic chain carrying the high load, and are subjected to large vibrations. Therefore, joints with indices 2-4 are equipped with full components of the proposed two-stage controller. Other joints use only the second-stage control without input shaping feedforward on the first-stage. This is because the joints with indices 5-6 are at the end of the kinematic chain, which are subjected to lower amplitude vibration. Joint 1 is a prismatic joint that is less prone to vibrations, and as such, the input shaping control should not be applied.

For experimental and simulation studies, reference trapezoidal trajectories which are continuous up to the second-order derivative are employed. The amplitude and rise time are adjusted to avoid saturating the motor torque. Three controllers are implemented including the rigid control (first-stage with the rigid control only), the input shaping control (first-stage with the input shaping feedforward), and the two-stage control (with input shaping feedforward at the first-stage).

The built-in Elmo motion drive uses a P/PI controller. In order to directly implement the proposed approach, the P/PI is transformed into a standard PID controller. The transformation and more details about the P/PI controller are given in Appendix I. Note that the velocity feedforward signal $\dot{r}_m$ is obtained by feeding the reference velocity $\dot{r}$ and feedback velocity $\dot{q}_r$ through the second-stage and feedforward transfer functions. The feedback velocity $\dot{q}_r$ is

numerically computed from q_r using backward difference. Experimental values of motor position q_m and reducer output position q_r are obtained from encoders, while those of link position q_l are measured with a laser tracker.

4.4.2 Parameter identification

Two robot configurations are used to identify robot parameters, as shown in Figure 4.18. The first is a fully extended pose, where the end effector is far from the track. The second is a fully folded pose, where the end effector is close to the track. These two configurations can be considered as a bound for trajectories of the SCOMPI robot. Since joint 2 is subjected to large vibrations, its identification procedure is detailed in the following.

Applying DESA for a time inverse temporal response of the reducer output position, the vibration frequency is 5.54 Hz and 7.97 Hz at the fully extended pose and at the fully folded pose, respectively. Then, the numerical optimization is launched to find the effective stiffness at each pose. As shown in Figure 4.19, after about 4 iterations, the effective stiffness converges to its optimized value. The effective stiffness at the fully extended pose and at the fully folded pose are 14.66 kNm/rad and 7.49 kNm/rad, respectively.

The feedback delay is then identified. Varying the motor feedback delay in the simulation causes significant changes of the motor torque at high frequencies. The delay time is found by matching the simulated and measured spectrum of the motor torques, as shown in Figure 4.20. The presence of a 2 ms delay is identified, which induces a resonance of about 93.57 Hz. A delay of 1 ms causes no significant oscillation peak after 10 Hz, while a delay of 3 ms causes instability. Good agreement between the motor torques from the simulation and the experiment are obtained in both flexible dynamic frequencies (0 to 10 Hz) and delay frequencies (about 94 Hz), as shown in Figure 4.21. Finally, the identified robot parameters are shown in Table 4.1.

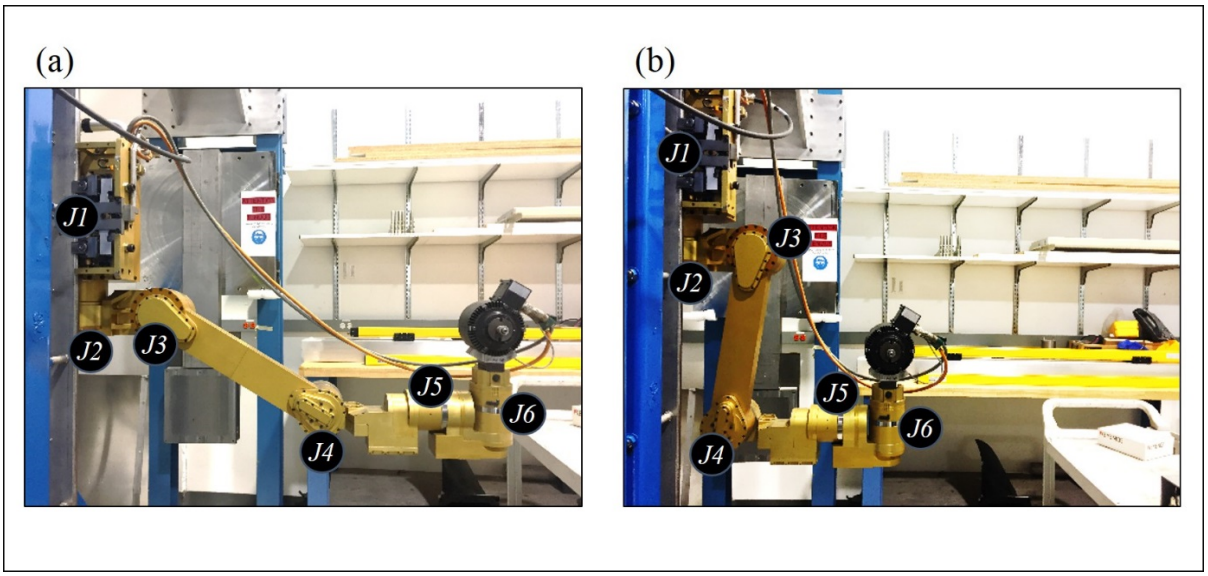

Figure 4.18 Robot configurations used for identification: (a) Fully extended pose and (b) Fully folded pose

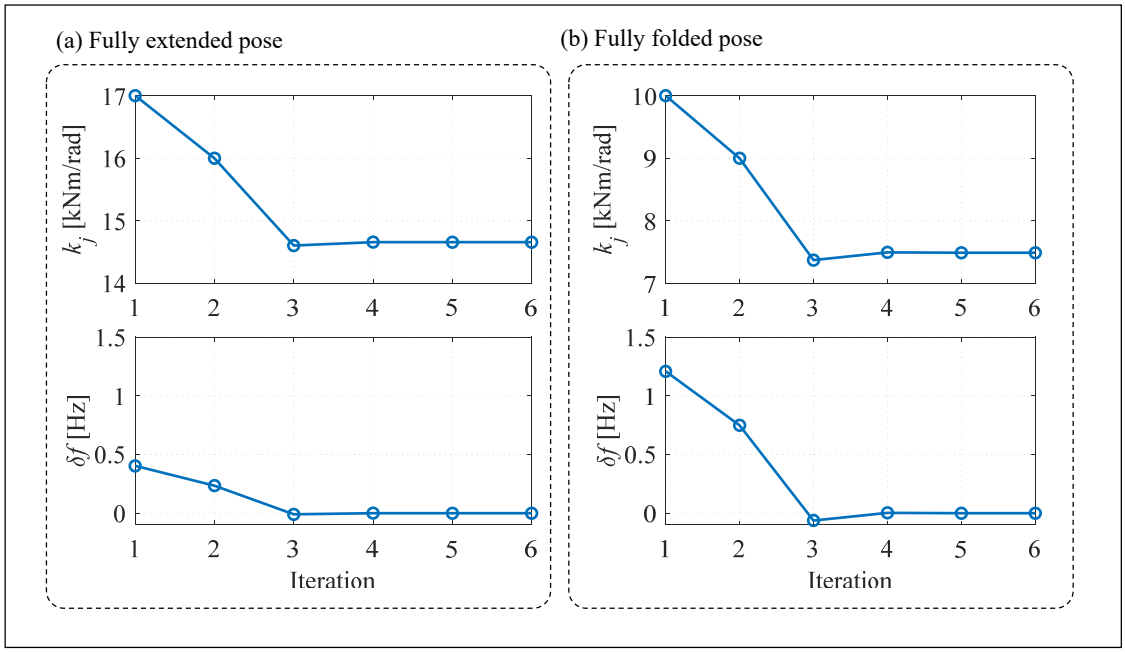

Figure 4.19 Identification of the effective joint 2 stiffness

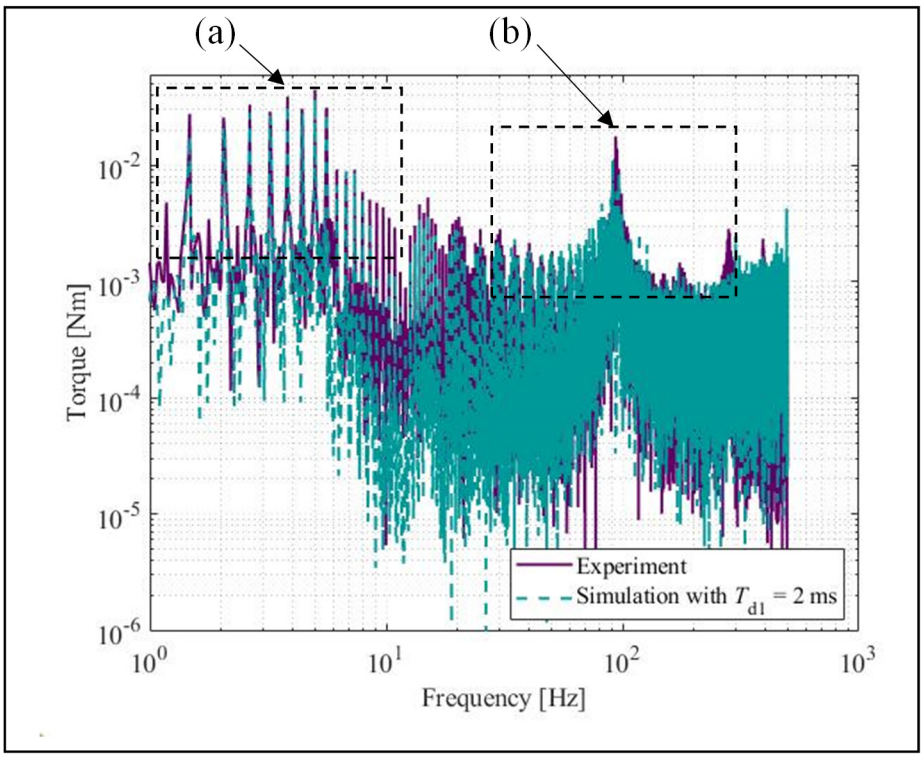

Figure 4.20 Comparison of experiment and simulation motor torque spectrums. (a) Flexible joint dynamics and (b) Delay dynamics

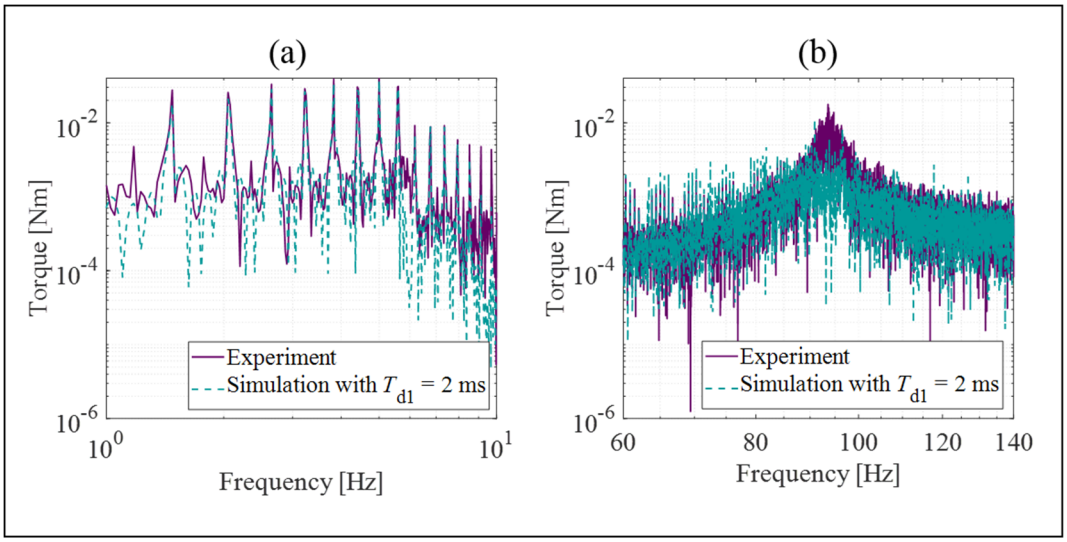

Figure 4.21 Zoomed-in of the regions (a) and (b) shown in Figure 4.20

4.4.3 Validation of the first-stage control performance

In this section, the rigid control and input shaping control are implemented. Using a reference trapezoidal trajectory, temporal responses of the reducer output position and motor torques using these two control approaches are obtained. Following that, the control performances are compared.

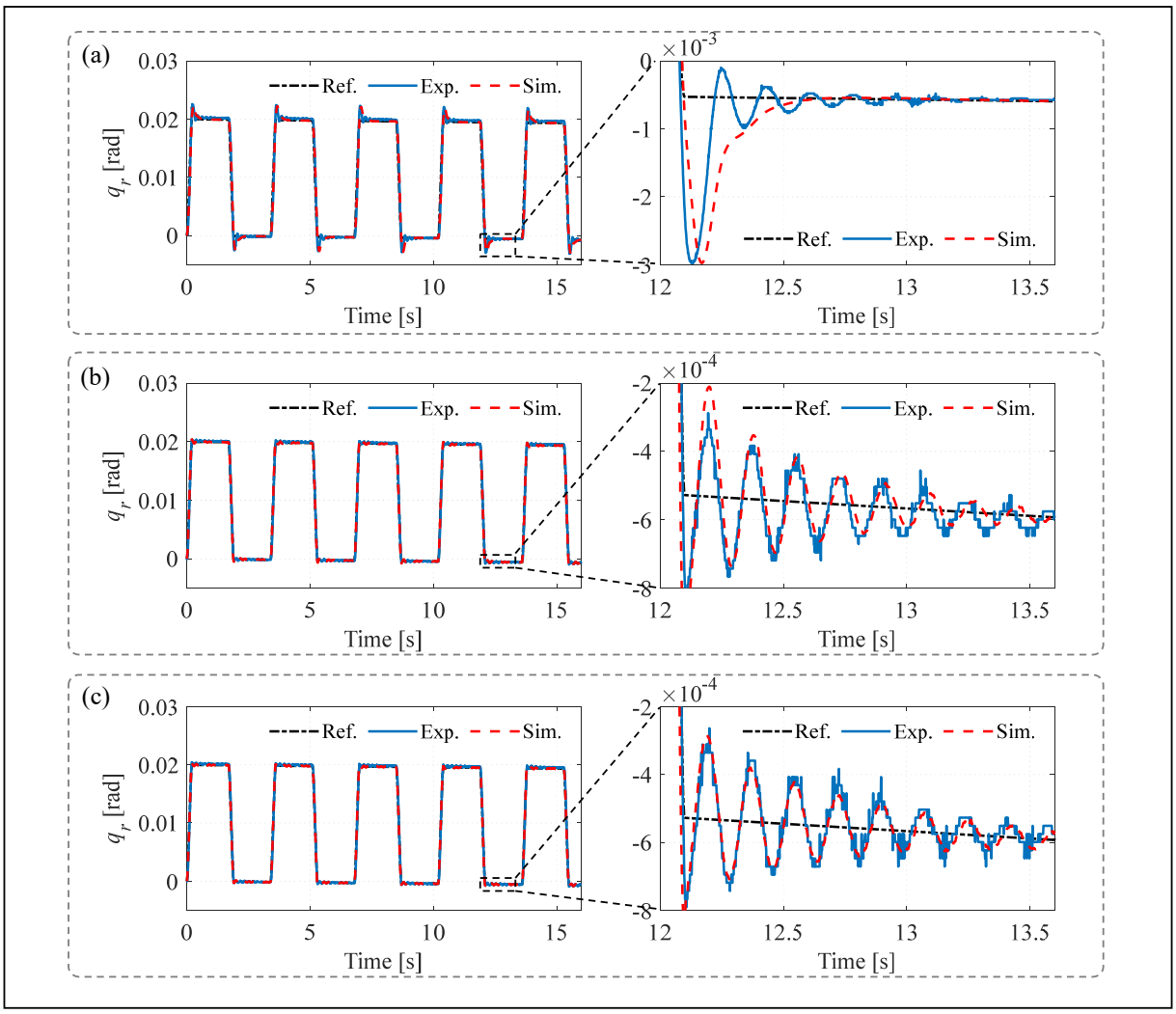

Figure 4.22 Experimental and simulation temporal responses of reducer output position q_r [rad] with rigid control. Rigid controller gains corresponding to (a) $\lambda_1 = 0.5$, (b) $\lambda_1 = 2.3$, and (c) $\lambda_1 = 2.8$

Rigid controller gains are set using parameters at the fully extended configuration. The parameter λ_{max} of 3.1 which results in an unstable system can be numerically found by solving the closed loop characteristic equation shown in Eq. (4.48). Figure 4.22 shows the temporal response of the reduce output position with RC gains set to $\lambda_1 = 0.5$, $\lambda_1 = 2.3$ (equals 75% of λ_{max}), and $\lambda_1 = 2.8$ (equals 90% of λ_{max}). The lowest rigid controller gains corresponding to $\lambda_1 = 0.5$ causes the highest overshoot, but less vibration. When λ_1 increases from 2.3 to 2.8, vibration changes slightly, as is shown in Figure 4.22(b) and Figure 4.22(c). However, the motor torque gets noisy quickly since the delay poles are excited. As shown in Figure 4.23, the peak according to the delay (at about 94 Hz) gets bigger as λ_1 is increased.

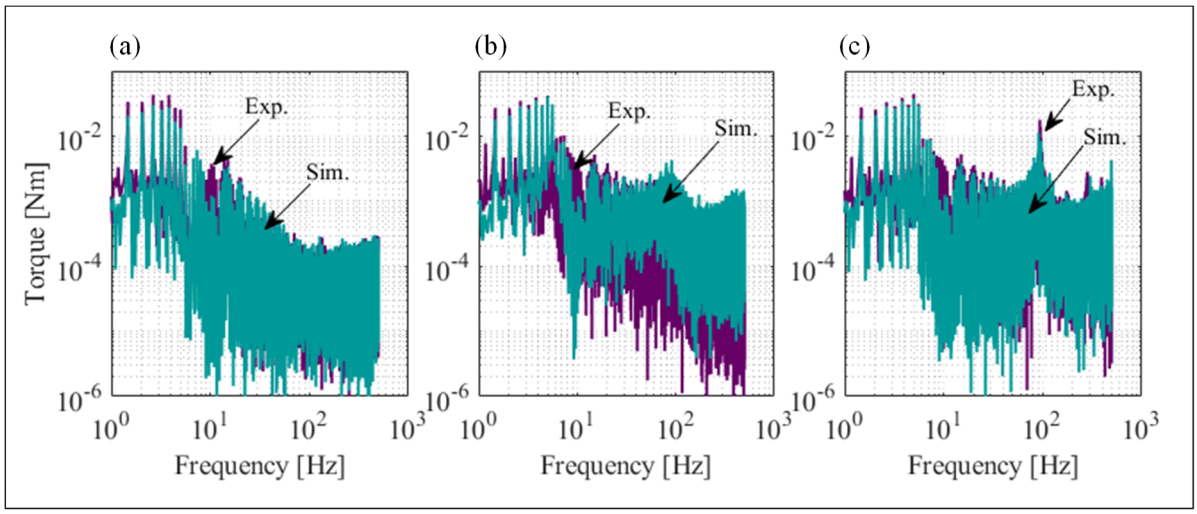

Figure 4.23 Experimental and simulation motor torque spectrum with rigid controller gains corresponding to (a) $\lambda_1 = 0.5$, (b) $\lambda_1 = 2.3$, and (c) $\lambda_1 = 2.8$

Discrepancies between experimental and simulation results can be found in Figure 4.22(a). The experimental reducer output position oscillates a little bit more than that in the simulation model. These results can be expected given the fact that the RC gains are low ($\lambda_1 = 0.5$), causing low rejections of unmodelled disturbances, such as nonlinear frictions. In general, good agreement between experimental and simulation results of the reducer output position are presented in Figure 4.22. The spectrums of the motor torque from simulation and

experiment are also similar, especially in terms of the matching of the frequency of the delay dynamics, as shown in Figure 4.23 (c).

The reducer output position using the input shaping control is shown in Figure 4.24. The vibration is significantly attenuated. Steady-state error due to gravity and calibration can be seen on one side of the response, as shown in Figure 4.24(b). A remaining overshoot, in the reducer output position response, is caused by an underdamped conjugate pair poles of the Butterworth low-pass filter inside the feedforward. Other low-pass filter, such as critical damped and Bessel, types can be used to avoid inducing that overshoot. However, these two filters provide less attenuation at high frequency.

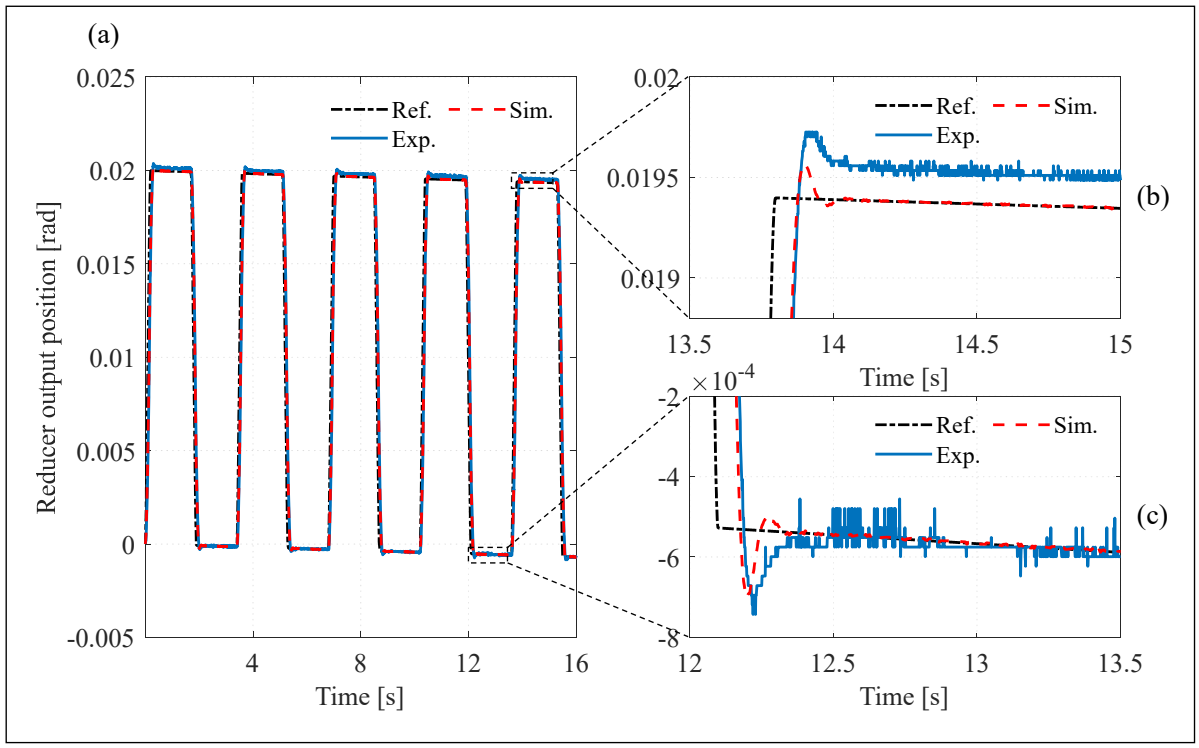

Figure 4.24 Experimental and simulation temporal responses of reducer output position with input shaping control

4.4.4 Validation of the second-stage control performance

The motion tracking performance of the two-stage controller with a second-stage generalized Smith predictor (GSP) disabled or enabled is shown in Figure 4.25. The PID compensator of

the second-stage is designed using $K_{d2} = 0.0075$. It is clearly seen that the GSP plays an important role in reducing vibration and allows cranking up the control gains. With the same K_{d2}, vibration is always reduced with GSP enabled.

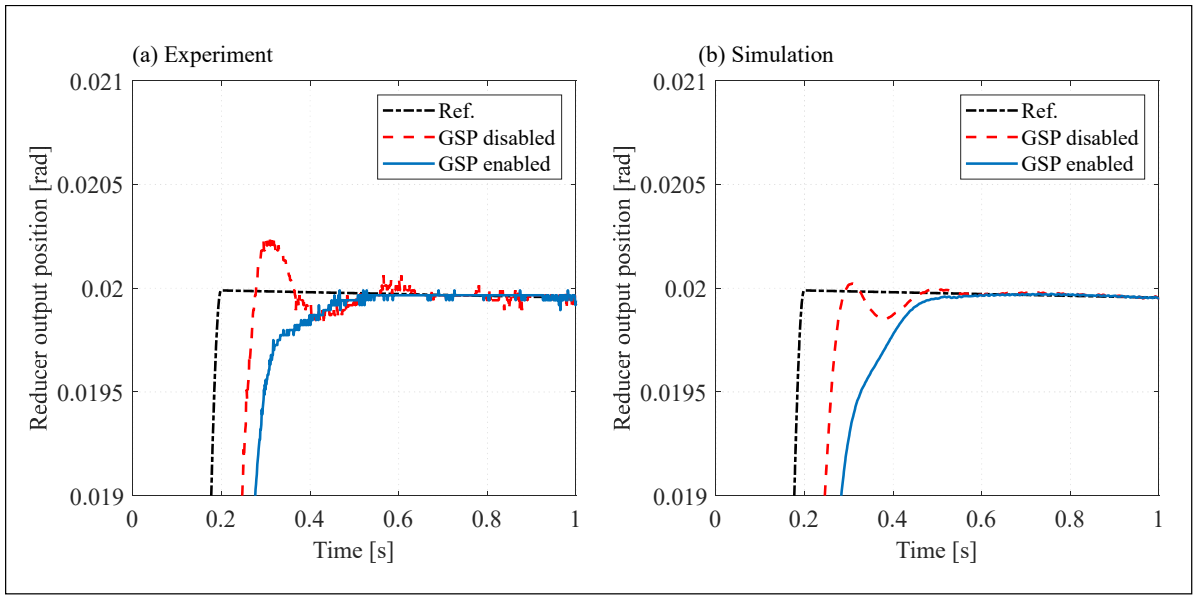

Figure 4.25 Experimental and simulation temporal responses of reducer output position using two-stage controller with GSP disabled or enabled

Figure 4.26 shows the torque frequency spectrum of the two-stage controller with the second-stage feedback filter enabled and disabled. With the feedback filter enabled, high amplitude harmonics of the motor torque near the delay frequency are significantly reduced. Without the feedback filter, the motor torques gets very noisy and are almost saturated.

Comparisons of the temporal responses using three controllers are given in Figure 4.27. The rigid control is designed with $\lambda_1 = 2.3$. The two-stage controller reduces both the vibration and disturbances. The response with the input shaping control and two-stage control reaches steady state in 0.4 secs, while that with rigid control keeps oscillating up to 1.4 secs. The steady-state error at the reducer output position is also eliminated with the two-stage controller, as shown in Figure 4.27 (b).

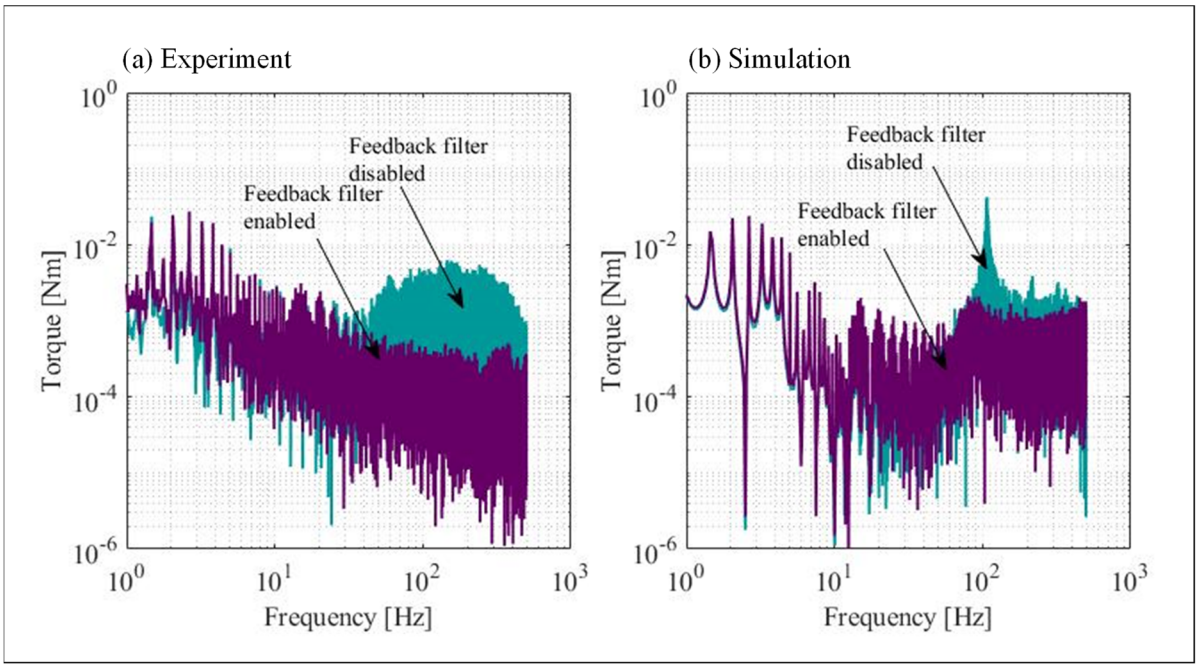

Figure 4.26 Experimental and simulation torque spectrum of two-stage controller with the feedback filter enabled and disabled

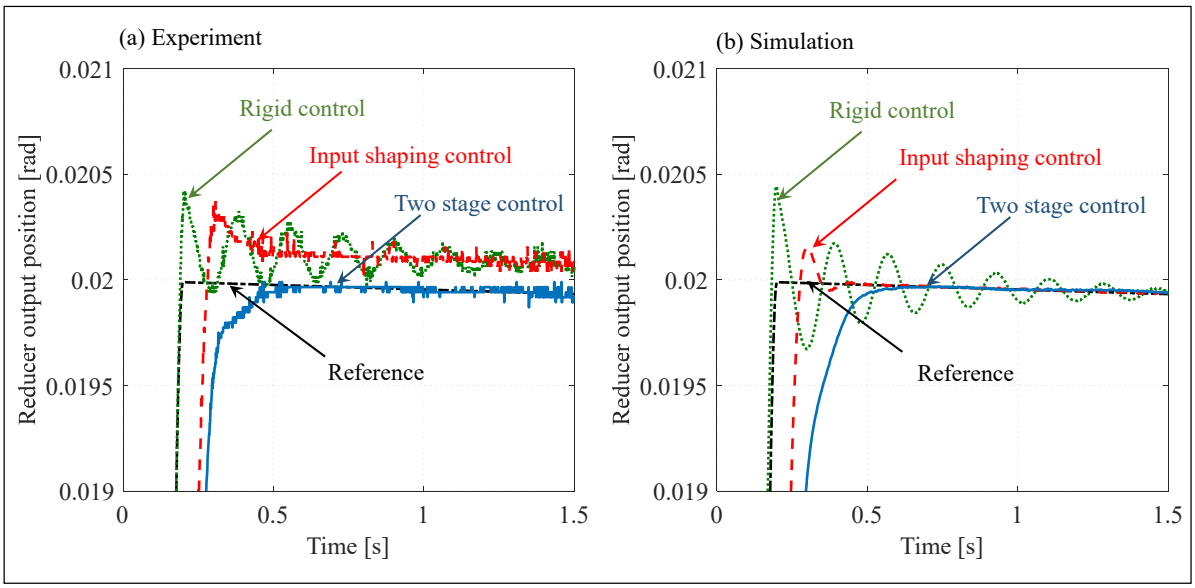

Figure 4.27 Experimental and simulation temporal responses with three controllers: Rigid control, Input shaping control, and Two-stage control: (a) Experiment, (b) Simulation

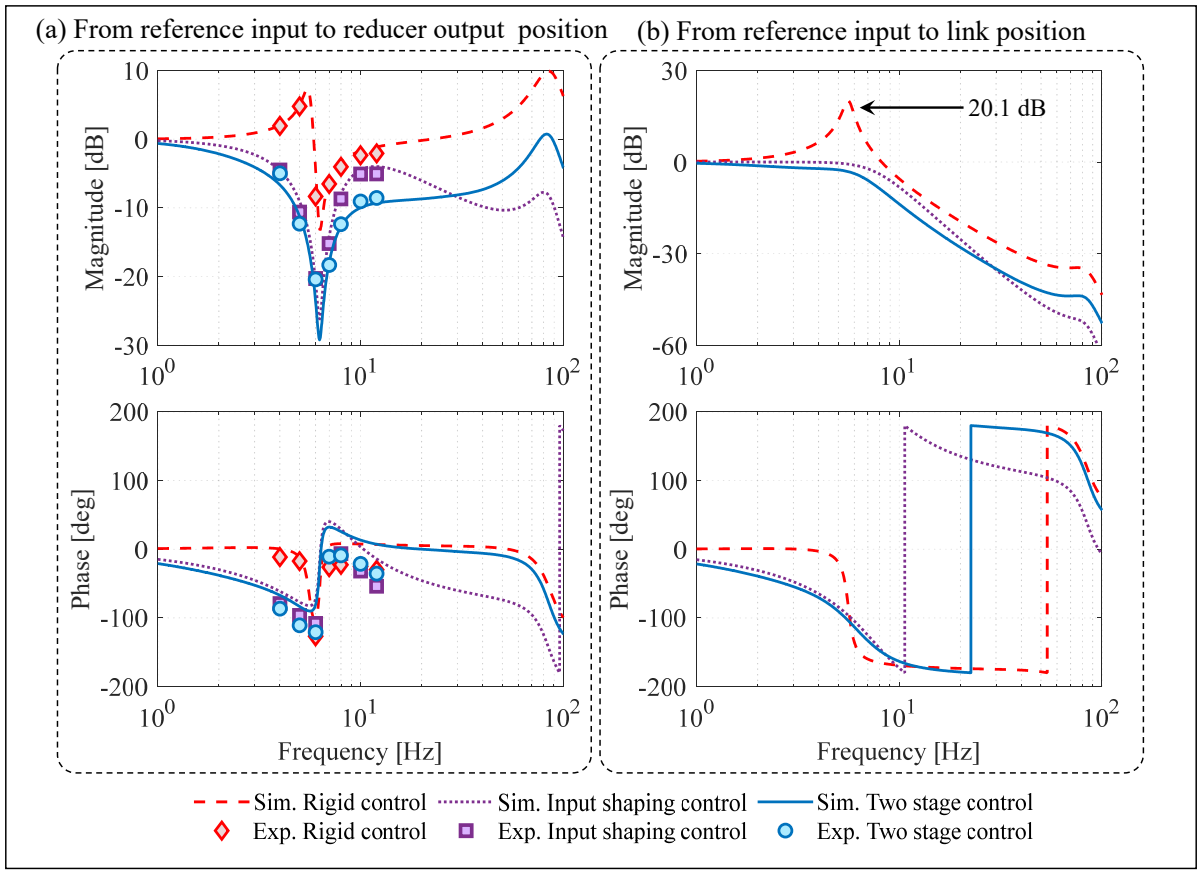

Figure 4.28 Experimental and simulation frequency responses with three controllers: Rigid control, Input shaping control, and Two-stage control; (a) From reference input to reducer output position, (b) From reference input to link position

Experimental and simulation frequency responses of the closed loop with three controllers are given in Figure 4.28. The rigid control is designed with $\lambda_1 = 2.3$. Vibration resonance in the reducer output position and link position are significantly reduced with feedforward and two-stage control. Indeed, the resonance of about 20.1 dB on the link side with rigid control (with $\lambda_1 = 2.3$) is reduced to almost 0 dB with the two-stage control. The bandwidth of the two-stage controller is 5.6 Hz, which is almost twice that of the rigid control at 2.9 Hz. Note that experimental measurements at link side are presented in section 4.4.6.

4.4.5 Validation of time-varying dynamics

In this section, the performance of the proposed controller with the time-varying robot configuration is presented. Figure 4.29(a) is a screenshot from the robot teach pendant that shows the reference trajectory used to test time-varying dynamics. The grinding tool is moved slowly from right to left (Figure 4.29(b-d)), following the red line, while the trapezoidal pattern of joint 2 (green line) is superimposed.

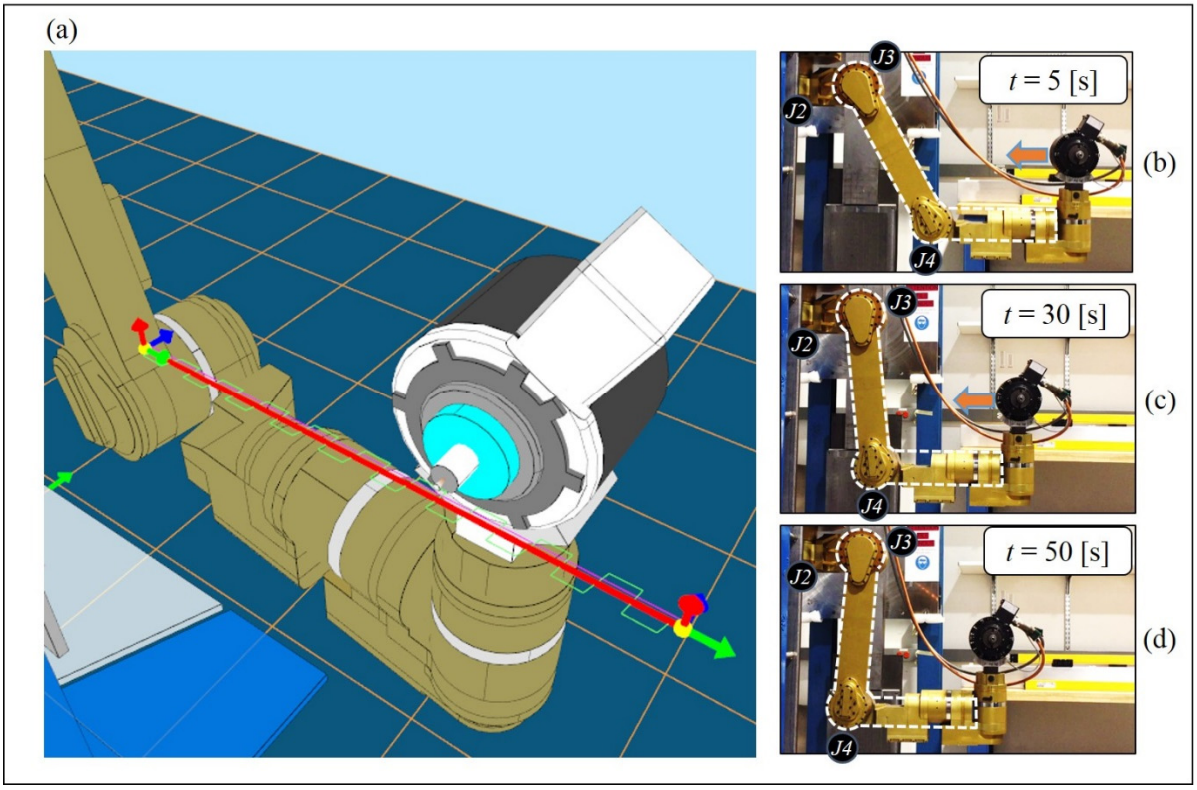

Figure 4.29 (a) Overview of the reference trajectory. The robot configuration changes from (b) large link 2 effective inertia, via (c) average link 2 effective inertia and finishes at (d) minimum link 2 effective side inertia

At initial time, the joint 2 effective inertia is $8.12\,\mathrm{kgm}^2$, the coupling stiffness is 13.39 kNm/rad , and the joint natural frequency is 6.19 Hz. At the end of the trajectory, 50 secs

later, the joint 2 effective inertia is $2.74\ \text{kgm}^2$, the coupling stiffness is $7.79\ \text{kNm/rad}$, and the joint natural frequency is 8.13 Hz.

Figure 4.30 shows the experimental temporal responses for the two-stage controller with and without time-varying dynamics. It is clearly seen that the two-stage controller, with updating dynamics enabled, significantly reduces the vibration as compared to that with updating dynamics disabled, even in the presence of large configuration variations.

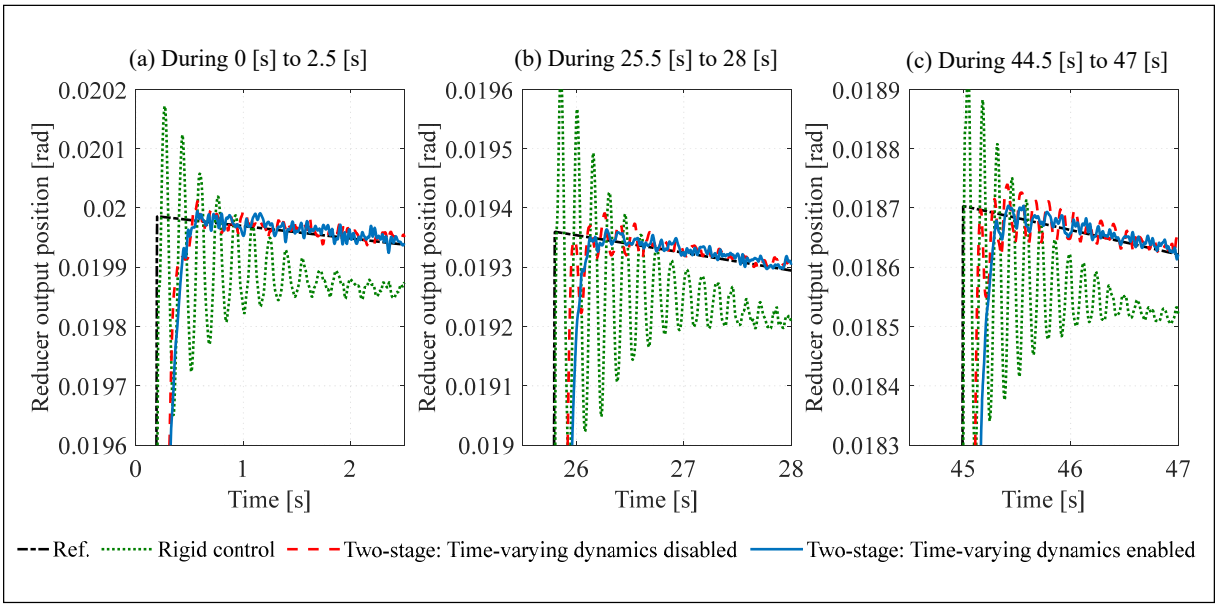

Figure 4.30 Experimental temporal responses of joint 2 for trapezoidal trajectory during configuration change. (a) For large link 2 effective inertia, (b) For average link 2 effective inertia, (c) For minimum link 2 effective inertia

4.4.6 Validation of end effector vibration attenuation

Although a decentralized approach is implemented to reduce vibration at the joint level, the main motivation for the proposed controller is to reduce the vibration at the robot end effector. To validate that the lumped coupling stiffness element introduced into each joint model is satisfactory for predicting the link vibration, measurements at the end effector are required.

To that end, a laser tracker (Faro Vintage) is used. A retro-reflector is attached to the grinder spindle as shown in Figure 4.31. The tracker can measure the Cartesian position of the retro-reflector at a sampling rate of up to 500 Hz, with an accuracy of 0.025 mm.

The end effector temporal response to the same reference trapezoidal trajectory used in sections 4.3 and 4.4 is measured with the laser tracker for the weaving experiments with joints 2, 3 and 4. The measured Cartesian position signals are converted into an angular joint position for comparison with the angular reference signal. The simulated link position, the experimental link position and the experimental reducer output position are plotted in Figure 4.32 to Figure 4.34 for the rigid controller (with $\lambda_1 = 2.3$), the input shaping controller and the two-stage controller.

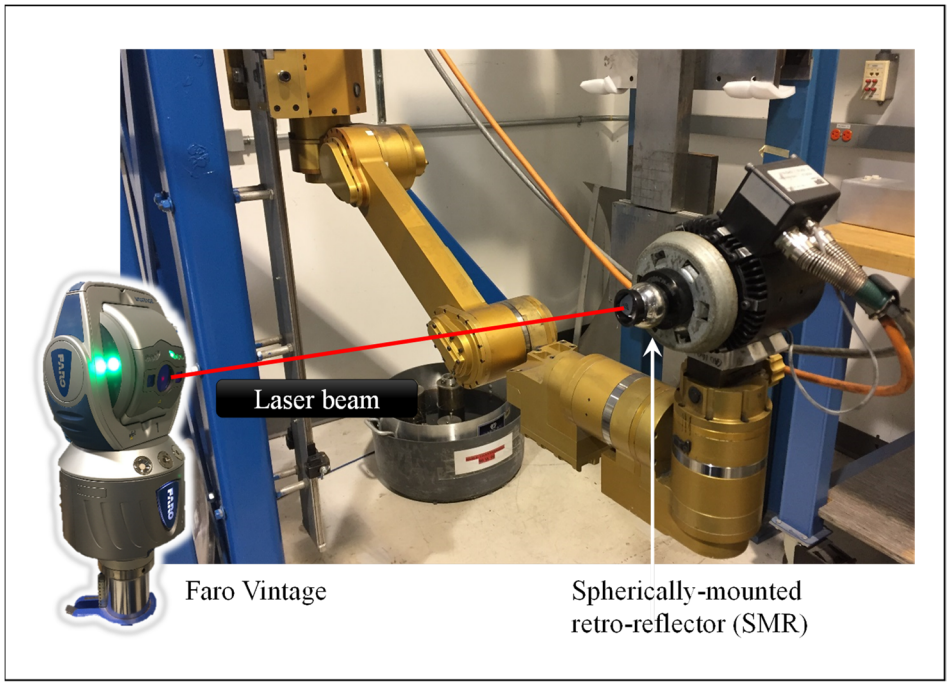

Figure 4.31 Experimental setup for measuring the robot end effector motion

For joints 2 and 3, the experimental measurements at the end effector are in good agreement with the simulation. It is clearly seen that the introduction of a lumped coupling stiffness

creates a significant amplification of the vibration, near resonance, from the reducer output position to the link position. This amplification factor is close to 400%.

For joint 4, there is a significant difference between the experiment and the simulation for the rigid control. The amplitude of link vibration from the simulation is much bigger than that from the experiment. In addition, another frequency of about 17 Hz can be seen (see zoomed-in area in Figure 4.34(a)). This new frequency may be caused by the unmodelled degrees of freedom of the joint 4 coupling dynamics, which are not captured by the lumped coupling stiffness model. Despite the limitations of the lumped model for joint 4, the vibration is still reduced significantly with the input shaping control and the two-stage control, as shown in Figure 4.34(b-c).

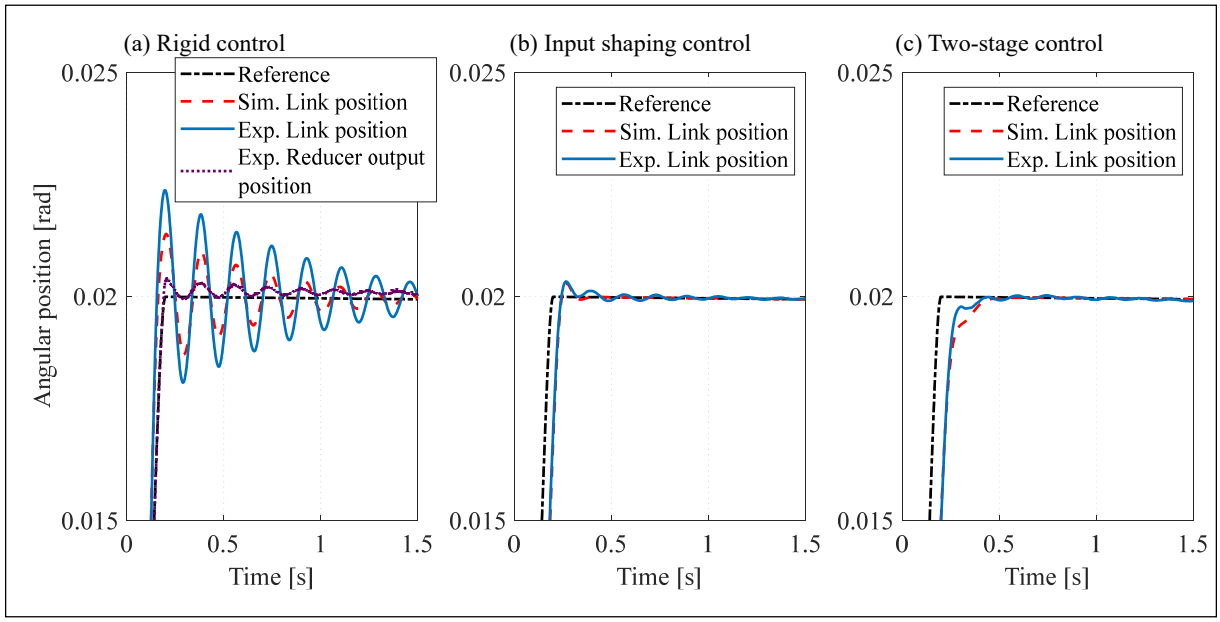

Figure 4.32 Experimental and simulation temporal responses of the end effector with joint 2 weaving for three controllers: (a) Rigid control, (b) Input shaping control, (c) Two-stage control. The measured Cartesian position signals are converted into an angular joint position for comparison with the angular reference signal

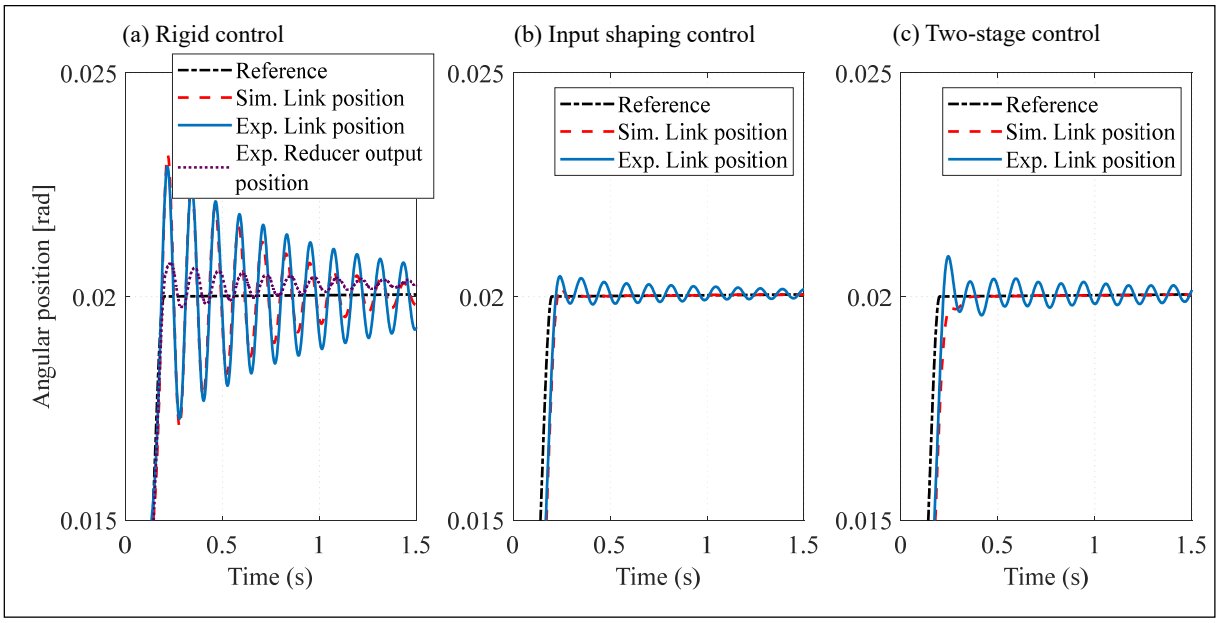

Figure 4.33 Experimental and simulation temporal responses of the end effector with joint 3 weaving for three controllers: (a) Rigid control, (b) Input shaping control, (c) Two-stage control

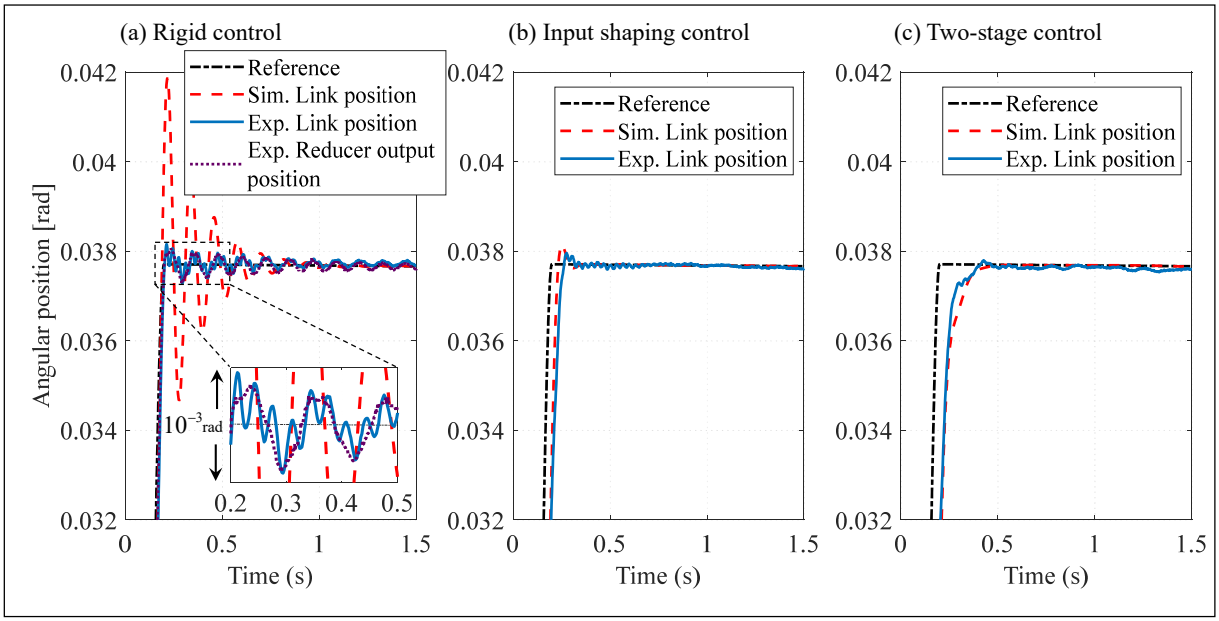

Figure 4.34 Experimental and simulation temporal responses of the end effector with joint 4 weaving for three controllers: (a) Rigid control, (b) Input shaping control, (c) Two-stage control

4.5 Summary

In this chapter, a two-stage controller for a flexible joint robot was presented. The proposed decentralized approach is simple, but effective through the use of a lumped coupling stiffness element in the flexible joint model. A methodology was detailed to design an input shaping discrete feedforward for the first-stage motor feedback control loop. Model parameter identification was realized from a closed-loop temporal response analysis. A second-stage control loop was implemented with a generalized Smith predictor for delay and filtering dynamics compensation. The approach was successfully retrofitted and tested on a six-axis serial robot.

The coefficients of the input shaping feedforward discrete-time transfer function can be time-varied to match the dynamics of the moving robot. The time-varying link inertias could be efficiently computed using the recursive Newton-Euler algorithm. With the tested robot, it was observed that the lumped coupling stiffness of the joints varies with the robot poses. To obtain optimal performance within the whole robot envelope, an interpolating technique to estimate this lumped stiffness would need to be developed.

The input shaping feedforward adds a delay to the position response. For robot motion in free space, the robot trajectory is just a delayed version of the input reference. Most often, the introduced delay is not a problem. However, if a third-stage control loop is required for regulating a process through some feedback measurement, the introduced delay can reduce the third stage bandwidth. In such a case, the delay compensation technique used for the second-stage can be applied to the third-stage.

One shortcoming of the input shaping approach is the poor disturbance rejection near resonance. During motion in free space, the inertial, centrifugal and Coriolis coupling torque disturbances may cause vibrations. These disturbances could be estimated from rigid body dynamics and an input shaping compensation technique could be developed.

The proposed controller is simple enough for retrofitting into existing serial robots. Knowledge of the robot link inertia tensor is required for computing the joint's effective link inertia. The access to joint torque is not needed but the robot must support joint reference position updating with a sampling rate significantly higher than the robot's dominant dynamic frequencies.

CONCLUSION

This thesis presents a study on the dynamics and vibration control of flexible joint robots. Two specific objectives were introduced. The first specific objective is to design vibration control algorithm for a simple case: a single joint robot considering only joint flexibility. The second objective is to design vibration control algorithm for actual industrial multiple flexible joint robots. The proposed control algorithms for these two objectives share the same two-stage architecture but are different in their components.

A vibration control algorithm for a single flexible joint robot was developed in the first phase of the study, which was presented in chapter 3. This study presented some important contributions on vibration control of flexible joint robots as follows: (i) It introduced a two-stage feedback control for flexible joint robot where partitioned controllers are employed on each stage. (ii) It combined the two-stage feedback control with a disturbance-state observer, in which both motor side and link side disturbances were compensated. (iii) It provided experimental validation in terms of extending the control bandwidth and reducing the vibration. Compared to the rigid control, the proposed controller displaces the link with almost no overshoot and the settling time is twice faster, while the vibration resonance due to kinematic error of the harmonic drive is also cut in half. Disturbances were compensated and the feedback noise is reduced. An important requirement to implement the proposed two-stage feedback control with a disturbance-state observer is the access to motor torque command.

Based on the promising results of vibration control of the single flexible joint robot, extensive study on vibration control of multiple flexible joint robot was conducted. Two options to make the testbed for multiple joint robots were considered. The first option was to build a multiple joint robot testbed, in which each joint uses the single flexible joint architecture developed in the first phase. The second option was to directly use an actual industrial robot as the testbed. Each option had its own advantages and disadvantages. If a multiple joint robot was built, as the first option, the vibration control developed in the first phase can be directly applied.

However, building a new robot would have required a lot of time and efforts. The second option was more preferable and finally selected. By using an actual industrial robot, all manpower and time to build robots were saved. However, instead of a full control environment as the self-built single flexible joint testbed, industrial robots normally provide only access to the motor position command (or the motor reference profile). The access to motor torque command was unavailable. Therefore, the two-stage feedback with disturbance-stage observer developed in the first phase, which requires the access to the motor torque command, cannot be directly applied to industrial robots.

In order to adapt to the constraints of industrial robots, a vibration control algorithm based on motor position command was developed. A two-stage controller based on time-varying input shaping and delay compensation was developed in the second phase of this study, which was described in chapter 4. This study provided some important contribution on control of multiple joint robots. (i) It firstly proposed a decentralized flexible joint model, which takes into account a lumped coupling stiffness element. (ii) It provided a two-stage controller including an input shaping feedforward with time-varying updating in the first-stage and a generalized Smith predictor to compensate for delay and feedback sensor filtering in the second-stage. An identification procedure was proposed to obtain all parameters that are needed to implement the proposed method. (iii) It provided experimental validation using an actual industrial serial robot. For implementation, the proposed controller requires a sampling rate significantly higher than the robot's dominant dynamic frequencies. This requirement can be satisfied easily since it is included in the standard setting of most industrial robots.

RECOMMENDATIONS

The research work presented in this thesis might be continued through the recommendations listed in the following:

The experimental study on vibration control of an industrial serial robot indicates that the accuracy of the coupling stiffness is a very important. The coupling stiffness significantly affects the input shaping feedforward transfer function, which determines how well the vibration is attenuated. The coupling stiffness, however, is difficult to be precisely obtained since it varies with the robot pose and no closed-form expression is available. To obtain optimal performance, an interpolating technique to estimate this coupling stiffness within the whole robot envelope is necessary to be developed.

The two-stage control based on input shaping approach has low disturbance rejection performance near the resonance frequency. Even while performing motion in free space, the inertial, centrifugal and Coriolis coupling torques disturbances may cause vibrations. Therefore, it is necessary to include disturbance compensations to the control architecture. A review on recent literature reveals that most disturbance compensation architectures require an access to the motor torque command. This requirement, however, is not fulfilled by the default setting of most recent industrial robots, which normally offer only an access to the reference position input. To overcome this obstacle, further studies focusing on disturbance compensation by reference profile alteration, as discussed in (Tan, Li, Chen, Teo, & Lee, 2019), is a promising research direction.

Another research direction is to apply the proposed two-stage controllers, which are originally for motion tracking applications, to industrial serial robots performing machining tasks. In that case, a third stage is required, which employs a feedback signal from the process. Due to a delay and noise of the process feedback signal, further work is required focusing on appropriate signal processing and filtering of the process feedback signal. A general Smith predictor to

compensate for the filtering dynamics of the process feedback signal may be required on the third-stage.

The machining process normally introduces large disturbances to the robot manipulator, which may cause unwanted distortions on both motor and link positions. In order to reduce the effects of the disturbances due to machining tasks, a disturbance compensation by reference profile alteration may be employed. A comprehensive experimental investigation may be needed to develop the dynamic model of the process, which can be used for designing the disturbance observer.

APPENDIX I

TRANSFORMATION BETWEEN PID AND P/PI COMPENSATORS

The P/PI controller is a dual control loop system, consisting of a proportional-integral compensator for the inner velocity control loop and a proportional compensator for the outer position control loop with velocity feedforward κ_{vf}. The block diagram of the PID and P/PI controllers are shown in Figure A I-1.

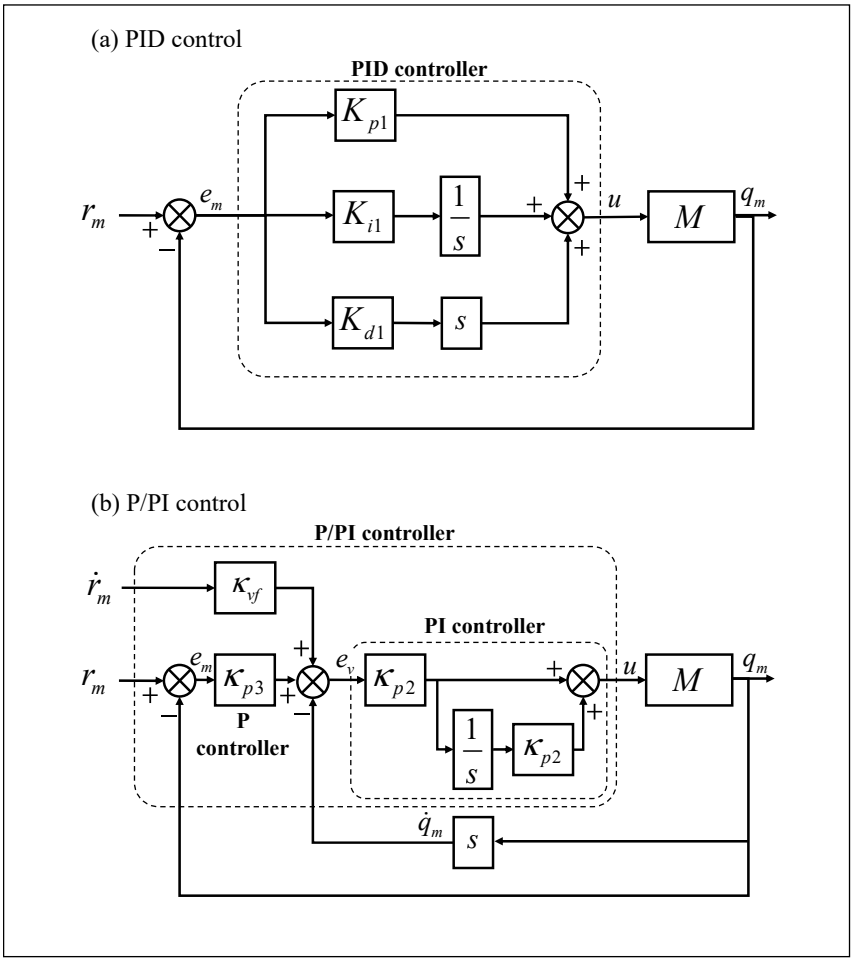

Figure A I-1 (a) Block diagram of PID controller, (b) Block diagram of P/PI controller

When the velocity feedforward gain κ_{vf} is set to 1, the P/PI controller can be transformed into a PID controller through the equations below:

$$\begin{cases} K_{p1} = \kappa_{p3}\kappa_{p2} + \kappa_{p2}\kappa_{i2} \\ K_{i1} = \kappa_{p3}\kappa_{p2}\kappa_{i2} \\ K_{d1} = \kappa_{p2} \end{cases} \tag{A I.1}$$

or

$$\begin{cases} \kappa_{p3} = \dfrac{K_{p1}}{K_{d1}} - \dfrac{1}{2K_{d1}}\left(K_{p1} \pm \sqrt{K_{p1}^2 - 4K_{d1}K_{i1}}\right) \\ \kappa_{p2} = K_{d1} \\ \kappa_{i2} = \dfrac{1}{2K_{d1}}\left(K_{p1} \pm \sqrt{K_{p1}^2 - 4K_{d1}K_{i1}}\right) \end{cases} \tag{A I.2}$$

where K_{p1}, K_{i1}, and K_{d1} are PID gains and κ_{p3}, κ_{p2}, and κ_{i2} are P/PI gains.

Proof:

The transfer function of PID compensator (Figure A I.1 (a)) is given as follows:

$$C_1(s) := \frac{u(s)}{e_m(s)} = K_{p1} + K_{d1}s + \frac{K_{i1}}{s} \tag{A I.3}$$

where K_{p1}, K_{i1}, and K_{d1} are PID gains, and s is the Laplace complex variable.

The output of PID control can be computed as follows:

$$u(s) = \underbrace{\left[\frac{K_{d1}s^2 + K_{p1}s + K_{i1}}{s}\right]}_{\text{PID controller}} e_m(s) \tag{A I.4}$$

where e_m is the motor position tracking error.

Consider the P/PI controller shown in Figure A I.1 (b), the input of the inner loop PI of P/PI can be derived as

$$\begin{aligned} e_v(s) &= r_m(s)s - q_m(s)s + \left[r_m(s) - q_m(s)\right]\kappa_{P3} \\ &= e_m(s)\left(s + \kappa_{P3}\right) \end{aligned} \tag{A I.5}$$

where $e_m(s) = r_m(s) - q_m(s)$.

Then, the output of the inner loop PI of P/PI is defined as:

$$u(s) = \kappa_{p2}\left(1 + \kappa_{i2}\frac{1}{s}\right)e_v(s) \tag{A I.6}$$

Substituting (A I.5) into (A I.6) gives:

$$u(s) = e_m(s)\kappa_{p2}\left(1 + \kappa_{i2}\frac{1}{s}\right)\left(s + \kappa_{p3}\right) \tag{A I.7}$$

By simple manipulating (A I.7) gives the transfer function of P/PI controller:

$$u(s) = \underbrace{\left[\frac{\kappa_{p2}s^2 + \left(\kappa_{p3}\kappa_{p2} + \kappa_{p2}\kappa_{i2}\right)s + \kappa_{p3}\kappa_{p2}\kappa_{i2}}{s}\right]}_{\text{P/PI controller}} e_m(s) \tag{A I.8}$$

To compute an equivalent of PID and P/PI in frequency domain, substituting into gives:

$$K_{D0}s^2 + K_{P0}s + K_{I0} = K_{P2}s^2 + \left(K_{P3}K_{P2} + K_{P2}K_{I2}\right)s + K_{P3}K_{P2}K_{I2} \tag{A I.9}$$

By equalizing corresponding coefficients of (A I.9) gives the linear transformation of gains as shown in (A I.1) and (A I.2).

LIST OF REFERENCES

Al-Ashoor, R. A., Patel, R. V., & Khorasani, K. (1993). Robust adaptive controller design and stability analysis for flexible-joint manipulators. *IEEE Transactions on Systems, Man and Cybernetics, 23*(2), 589-602. doi:10.1109/21.229473

Albu-Schäffer, A., Ott, C., & Hirzinger, G. (2007). A Unified Passivity-based Control Framework for Position, Torque and Impedance Control of Flexible Joint Robots. *The International Journal of Robotics Research, 26*(1), 23-39. doi:10.1177/0278364907073776

An-Chyau, H., & Yuan-Chih, C. (2004). Adaptive sliding control for single-link flexible-joint robot with mismatched uncertainties. *IEEE Transactions on Control Systems Technology, 12*(5), 770-775. doi:10.1109/TCST.2004.826968

Bang, J. S., Shim, H., Park, S. K., & Seo, J. H. (2010). Robust Tracking and Vibration Suppression for a Two-Inertia System by Combining Backstepping Approach With Disturbance Observer. *IEEE Transactions on industrial electronics, 57*(9), 3197-3206. doi:10.1109/TIE.2009.2038398

Baspinar, C. (2011). *Position Control of Flexible Joint Robots by Adapting Methods for Rigid Robots*. Paper presented at the Preprints of the 18th IFAC World Congress, Milano, Italy.

Botsali, F. M., Kalyoncu, M., Tinkir, M., & Onen, U. (2010, 26-28 Feb. 2010). *Fuzzy logic trajectory control of flexible robot manipulator with rotating prismatic joint.* Paper presented at the Computer and Automation Engineering (ICCAE), 2010 The 2nd International Conference on.

Chatlatanagulchai, W., & Meckl, P. H. (2005, 2-6 Aug. 2005). *Intelligent control of a two-link flexible-joint robot, using backstepping, neural networks, and direct method.* Paper presented at the 2005 IEEE/RSJ International Conference on Intelligent Robots and Systems, (IROS 2005).

Chen, M., & Ge, S. S. (2013). Direct Adaptive Neural Control for a Class of Uncertain Nonaffine Nonlinear Systems Based on Disturbance Observer. *IEEE Transactions on Cybernetics, 43*(4), 1213-1225. doi:10.1109/TSMCB.2012.2226577

Chen, W., & Tomizuka, M. (2014). Dual-Stage Iterative Learning Control for MIMO Mismatched System With Application to Robots With Joint Elasticity. *IEEE Transactions on Control Systems Technology, 22*(4), 1350-1361. doi:10.1109/TCST.2013.2279652

Chen, W., Yang, J., Guo, L., & Li, S. (2016). Disturbance-Observer-Based Control and Related Methods—An Overview. *IEEE Transactions on industrial electronics, 63*(2), 1083-1095. doi:10.1109/TIE.2015.2478397

Cheng-Huei, H., Chun-Chih, W., & Masayoshi, T. (2008, 26-28 March 2008). *Suppression of vibration due to transmission error of harmonic drives using peak filter with acceleration feedback.* Paper presented at the 2008 10th IEEE International Workshop on Advanced Motion Control.

Craig, J. J. (1989). *Introduction to Robotics: Mechanics and Control*: Addison-Wesley Longman: Boston, MA, USA.

D.-W. Gu, P. P., M. M. Konstantinov. (2005). *Robust control design with MATLAB*. London: Springer.

Dallali, H., Lee, J., Tsagarakis, N. G., & Caldwell, D. G. (2015). Experimental Study on Linear State Feedback Control of Humanoid Robots with Flexible Joints. *IFAC-PapersOnLine, 48*(19), 130-135. doi:http://dx.doi.org/10.1016/j.ifacol.2015.12.022

Dallali, H., Medrano-Cerda, G., Kashiri, N., Tsagarakis, N., & Caldwell, D. (2014, 21-23 Oct. 2014). *Decentralized Feedback Design for a Compliant Robot Arm.* Paper presented at the 2014 European Modelling Symposium.

De Luca, A. (1998). *Trajectory control of flexible manipulators*, Berlin, Heidelberg.

De Luca, A. (2000). *Feedforward/feedback laws for the control of flexible robots*. Paper presented at the Proceedings of IEEE International Conference on Robotics and Automation.

De Luca, A., & Book, W. (2008). Robots with Flexible Elements. In B. Siciliano & O. Khatib (Eds.), *Springer Handbook of Robotics* (pp. 287-319): Springer Berlin Heidelberg.

De Luca, A., Farina, R., & Lucibello, P. (2005, 18-22 April 2005). *On the Control of Robots with Visco-Elastic Joints.* Paper presented at the Robotics and Automation, 2005. ICRA 2005. Proceedings of the 2005 IEEE International Conference on.

De Luca, A., & Flacco, F. (2011, 9-13 May 2011). *A PD-type regulator with exact gravity cancellation for robots with flexible joints.* Paper presented at the IEEE International Conference on Robotics and Automation (ICRA).

De Luca, A., Siciliano, B., & Zollo, L. (2005). PD control with on-line gravity compensation for robots with elastic joints: Theory and experiments. *Automatica, 41*(10), 1809-1819. doi:http://dx.doi.org/10.1016/j.automatica.2005.05.009

Doria, A., Cocuzza, S., Comand, N., Bottin, M., & Rossi, A. (2019). Analysis of the Compliance Properties of an Industrial Robot with the Mozzi Axis Approach. *Robotics, 8*(3). doi:10.3390/robotics8030080

Elbestawi, M. A., Yuen, K. M., Srivastava, A. K., & Dai, H. (1991). Adaptive Force Control for Robotic Disk Grinding. *CIRP Annals - Manufacturing Technology, 40*(1), 391-394. doi:http://dx.doi.org/10.1016/S0007-8506(07)62014-9

Ellis, G. (2004). *Control System Design Guide (Third Edition)*. Burlington: Academic Press.

Featherstone, R., & Orin, D. (2000, 24-28 April 2000). *Robot dynamics: equations and algorithms.* Paper presented at the Proceedings 2000 ICRA. Millennium Conference. IEEE International Conference on Robotics and Automation. Symposia Proceedings (Cat. No.00CH37065).

Franklin, G. F., Powell, J. D., & Emami-Naeini, A. (2010). *Feedback control of dynamic systems*: Peason Education Ltd.

G. F. Franklin, J. David Powell, & Workman, M. L. (1997). *Digital Control of Dynamic Systems (3rd Edition*: Ellis-Kagle Press.

Gandhi, P. S., & Ghorbel, F. H. (2002). Closed-loop compensation of kinematic error in harmonic drives for precision control applications. *IEEE Transactions on Control Systems Technology, 10*(6), 759-768. doi:10.1109/TCST.2002.804119

Ge, S. S., Lee, T. H., & Tan, E. G. (1997, 5-7 Oct 1997). *Adaptive neural network control of flexible link robots based on singular perturbation.* Paper presented at the Control Applications, 1997., Proceedings of the 1997 IEEE International Conference on.

Gharaaty, S., Shu, T., Joubair, A., Xie, W. F., & Bonev, I. A. (2018). Online pose correction of an industrial robot using an optical coordinate measure machine system. *International Journal of Advanced Robotic Systems, 15*(4), 1729881418787915. doi:10.1177/1729881418787915

Giusti, A., Malzahn, J., Tsagarakis, N. G., & Althoff, M. (2017, May 29 2017-June 3 2017). *Combined inverse-dynamics/passivity-based control for robots with elastic joints.* Paper presented at the 2017 IEEE International Conference on Robotics and Automation (ICRA).

Hamelin, P., Bigras, P., Beaudry, J., Richard, P., & Blain, M. (2014). Multiobjective Optimization of an Observer-Based Controller: Theory and Experiments on an Underwater Grinding Robot. *IEEE Transactions on Control Systems Technology, 22*(5), 1875-1882. doi:10.1109/TCST.2013.2296355

Hamelin, P., Bigras, P., Beaudry, J., Richard, P. L., & Blain, M. (2012). Discrete-Time State Feedback With Velocity Estimation Using a Dual Observer: Application to an

Underwater Direct-Drive Grinding Robot. *IEEE/ASME Transactions on Mechatronics, 17*(1), 187-191. doi:10.1109/TMECH.2011.2154338

Han, J. (2009). From PID to Active Disturbance Rejection Control. *IEEE Transactions on industrial electronics, 56*(3), 900-906. doi:10.1109/TIE.2008.2011621

HarmonicDrive. (2009). *General Catalog Harmonic Drive Gearing & Motion Control*.

Hunmo, K., & Parker, J. K. (1993a, 7-9 Mar 1993). *Artificial neural network for identification and tracking control of a flexible joint single-link robot.* Paper presented at the Twenty-Fifth Southeastern Symposium on System Theory.

Hunmo, K., & Parker, J. K. (1993b, 25-29 Oct. 1993). *Hidden control neural network identification-based tracking control of a flexible joint robot.* Paper presented at the Proceedings of 1993 International Joint Conference on Neural Networks.

Jae Young, L., Je Sung, Y., & Jong Hyeon, P. (2007, 17-20 Sept. 2007). *Robust nonlinear control for flexible joint robot manipulators.* Paper presented at the SICE, 2007 Annual Conference.

Keppler, M., Lakatos, D., Ott, C., & Albu-Schäffer, A. (2018). Elastic Structure Preserving (ESP) Control for Compliantly Actuated Robots. *IEEE Transactions on Robotics, 34*(2), 317-335. doi:10.1109/TRO.2017.2776314

Khorasani, K. (1991, 9-11 Apr 1991). *Adaptive control of flexible joint robots.* Paper presented at the IEEE International Conference on Robotics and Automation.

Kim, M. J., & Chung, W. K. (2015). Disturbance-Observer-Based PD Control of Flexible Joint Robots for Asymptotic Convergence. *IEEE Transactions on Robotics, 31*(6), 1508-1516. doi:10.1109/TRO.2015.2477957

Kim, S.-K., Park, C. R., Yoon, T.-W., & Lee, Y. I. (2015). Disturbance-observer-based model predictive control for output voltage regulation of three-phase inverter for uninterruptible-power-supply applications. *European Journal of Control, 23*, 71-83. doi:https://doi.org/10.1016/j.ejcon.2015.02.004

Kwan, C.-M., & Yeung, K. S. (1993). Robust adaptive control of revolute flexible-joint manipulators using sliding technique. *Systems & Control Letters, 20*(4), 279-288. doi:http://dx.doi.org/10.1016/0167-6911(93)90004-P

Lee, T. H., Ge, S. S., & Wang, Z. P. (2001). Adaptive robust controller design for multi-link flexible robots. *Mechatronics, 11*(8), 951-967. doi:http://dx.doi.org/10.1016/S0957-4158(00)00062-3

Lessard, J., Bigras, P., Liu, Z., & Hazel, B. (2014). Characterization, modeling and vibration control of a flexible joint for a robotic system. *Journal of Vibration and Control, 20*(6), 943-960.

Lightcap, C. A., & Banks, S. A. (2010). An Extended Kalman Filter for Real-Time Estimation and Control of a Rigid-Link Flexible-Joint Manipulator. *IEEE Transactions on Control Systems Technology, 18*(1), 91-103. doi:10.1109/TCST.2009.2014959

Lin, T., & Goldenberg, A. A. (1995, 21-27 May 1995). *Robust adaptive control of flexible joint robots with joint torque feedback.* Paper presented at the Proceedings of 1995 IEEE International Conference on Robotics and Automation.

Liu, H., & Huang, Y. (2018). Robust adaptive output feedback tracking control for flexible-joint robot manipulators based on singularly perturbed decoupling. *Robotica, 36*(6), 822-838. doi:10.1017/S0263574718000061

Losey, D. P., Erwin, A., McDonald, C. G., Sergi, F., & O'Malley, M. K. (2016). A Time-Domain Approach to Control of Series Elastic Actuators: Adaptive Torque and Passivity-Based Impedance Control. *IEEE/ASME Transactions on Mechatronics, 21*(4), 2085-2096. doi:10.1109/TMECH.2016.2557727

Malki, H. A., Misir, D., Feigenspan, D., & Guanrong, C. (1997). Fuzzy PID control of a flexible-joint robot arm with uncertainties from time-varying loads. *IEEE Transactions on Control Systems Technology, 5*(3), 371-378. doi:10.1109/87.572133

Maragos, P., Kaiser, J. F., & Quatieri, T. F. (1993). Energy separation in signal modulations with application to speech analysis. *IEEE Transactions on Signal Processing, 41*(10), 3024-3051. doi:10.1109/78.277799

Miao, Z., & Wang, Y. (2013). Robust dynamic surface control of flexible joint robots using recurrent neural networks. *Journal of Control Theory and Applications, 11*(2), 222-229. doi:10.1007/s11768-013-1240-x

Mills, J. K. (1992). Stability and control of elastic-joint robotic manipulators during constrained-motion tasks. *IEEE Transactions on Robotics and Automation, 8*(1), 119-126. doi:10.1109/70.127246

Mohammadi, A., Tavakoli, M., Marquez, H. J., & Hashemzadeh, F. (2013). Nonlinear disturbance observer design for robotic manipulators. *Control Engineering Practice, 21*(3), 253-267. doi:http://dx.doi.org/10.1016/j.conengprac.2012.10.008

Morales, R., Feliu, V., & Jaramillo, V. (2012). Position control of very lightweight single-link flexible arms with large payload variations by using disturbance observers. *Robotics and Autonomous Systems, 60*(4), 532-547. doi:https://doi.org/10.1016/j.robot.2011.11.016

Nanos, K., & Papadopoulos, E. G. (2015). On the dynamics and control of flexible joint space manipulators. *Control Engineering Practice, 45*, 230-243. doi:https://doi.org/10.1016/j.conengprac.2015.06.009

Oh, J. H., & Lee, J. S. (1997, 20-25 Apr 1997). *Control of flexible joint robot system by backstepping design approach.* Paper presented at the IEEE International Conference on Robotics and Automation.

Oh, J. H., & Lee, J. S. (1999). Control of flexible joint robot system by backstepping design approach. *Intelligent Automation & Soft Computing, 5*(4), 267-278. doi:10.1080/10798587.1999.10750607

Oh, S., & Kong, K. (2017). High-precision robust force control of a series elastic actuator. *IEEE/ASME Transactions on Mechatronics, 22*(1), 71-80. doi:10.1109/TMECH.2016.2614503

Paine, N., Mehling, J. S., Holley, J., Radford, N. A., Johnson, G., Fok, C.-L., & Sentis, L. (2015). Actuator Control for the NASA-JSC Valkyrie Humanoid Robot: A Decoupled Dynamics Approach for Torque Control of Series Elastic Robots. *Journal of Field Robotics, 32*(3), 378-396. doi:10.1002/rob.21556

Parvathy, R., & Daniel, A. E. (2013, 22-23 March 2013). *A survey on active disturbance rejection control.* Paper presented at the 2013 International Mutli-Conference on Automation, Computing, Communication, Control and Compressed Sensing (iMac4s).

Paul, R. P. (1981). *Robot Manipulators*. MIT Press, Cambridge, MA.

Pekař, L., & Kureckova, E. (2011). *Rational approximations for time-delay systems: case studies*.

Pham, M.-N., & Ahn, H.-J. (2014). Experimental optimization of a hybrid foil–magnetic bearing to support a flexible rotor. *Mechanical Systems and Signal Processing, 46*(2), 361-372. doi:http://dx.doi.org/10.1016/j.ymssp.2014.01.012

Pham, M.-N., Hamelin, P., Hazel, B., & Liu, Z. (2019). A Two-Stage State Feedback Controller Supported by Disturbance-State Observer for Vibration Control of a Flexible-Joint Robot. *Robotica*, 1-23. doi:10.1017/S0263574719001267

Pham, M.-N., Hazel, B., Hamelin, P., & Liu, Z. (2019). Vibration control of flexible joint robots using a discrete-time two-stage controller based on time-varying input shaping and delay compensation. *Robotics and Autonomous Systems (Submitted in December 2019)*.

Readman, M. C., & Belanger, P. R. (1990a, 5-7 Dec 1990). *Analysis and control of a flexible joint robot.* Paper presented at the Proceedings of the 29th IEEE Conference on Decision and Control.

Readman, M. C., & Belanger, P. R. (1990b, 5-7 Dec 1990). *Analysis and control of a flexible joint robot.* Paper presented at the Proceedings of the 29th IEEE Conference on Decision and Control.

Sariyildiz, E., Chen, G., & Yu, H. (2016). An Acceleration-Based Robust Motion Controller Design for a Novel Series Elastic Actuator. *IEEE Transactions on industrial electronics, 63*(3), 1900-1910. doi:10.1109/TIE.2015.2512228

Ser Yong, L., Dawson, D. M., Jun, H., & de Queiroz, M. S. (1997). An adaptive link position tracking controller for rigid-link flexible-joint robots without velocity measurements. *IEEE Transactions on Systems, Man, and Cybernetics, Part B: Cybernetics, 27*(3), 412-427. doi:10.1109/3477.584949

Shi, X., Zhang, F., Qu, X., & Liu, B. (2016). An online real-time path compensation system for industrial robots based on laser tracker. *International Journal of Advanced Robotic Systems, 13*(5), 1729881416663366. doi:10.1177/1729881416663366

Shipitko, I. A., & Zmeu, K. V. (2003, 7-11 April 2003). *Predictive control with neural network model for flexible link robot.* Paper presented at the Modern Techniques and Technologies, 2003. MTT 2003. Proceedings of the 9th International Scientific and Practical Conference of Students, Post-graduates and Young Scientists.

Shu, T., Gharaaty, S., Xie, W., Joubair, A., & Bonev, I. A. (2018). Dynamic Path Tracking of Industrial Robots With High Accuracy Using Photogrammetry Sensor. *IEEE/ASME Transactions on Mechatronics, 23*(3), 1159-1170. doi:10.1109/TMECH.2018.2821600

Singhose, W. (2009). Command shaping for flexible systems: A review of the first 50 years. *International Journal of Precision Engineering and Manufacturing, 10*(4), 153-168. doi:10.1007/s12541-009-0084-2

Smith, J. M. (1957). Closer Control of Loops with Dead Time. *Chemical Engineering Progress, 53*(5), 217-219.

Smith, J. Y., Kozak, K., & Singhose, W. E. (2002, 8-10 May 2002). *Input shaping for a simple nonlinear system.* Paper presented at the Proceedings of the 2002 American Control Conference (IEEE Cat. No.CH37301).

Spong, M. W. (1987). Modeling and Control of Elastic Joint Robots. *Journal of Dynamic Systems, Measurement, and Control, 109*(4), 310-318. doi:10.1115/1.3143860

Spong, M. W. (1989). Adaptive control of flexible joint manipulators. *Systems & Control Letters, 13*(1), 15-21. doi:http://dx.doi.org/10.1016/0167-6911(89)90016-9

Spong, M. W. (1990). *Control of Flexible Joint Robots: A Survey*: University of Illinois, Coordinated Science Laboratory.

Sungha Kwon, A. A., Seungkyu Park. (2016). Control of flexible joint robot using integral sliding mode and backstepping. *Automation, Control and Intelligent Systems, 4*(6), 95-100.

Tae-Jun, H., Jaeyoung, L., & Jong Hyeon, P. (2007, 15-18 Dec. 2007). *Robust control by inverse optimal PID approach for flexible joint robot manipulator.* Paper presented at the IEEE International Conference on Robotics and Biomimetics.

Tan, K. K., Li, X., Chen, S., Teo, C. S., & Lee, T. H. (2019). Disturbance Compensation by Reference Profile Alteration With Application to Tray Indexing. *IEEE Transactions on industrial electronics, 66*(12), 9406-9416. doi:10.1109/TIE.2019.2892684

Thiran, J. (1971). Recursive digital filters with maximally flat group delay. *IEEE Transactions on Circuit Theory, 18*(6), 659-664. doi:10.1109/TCT.1971.1083363

Tomei, P. (1991a). A simple PD controller for robots with elastic joints. *IEEE Transactions on Automatic Control, 36*(10), 1208-1213. doi:10.1109/9.90238

Tomei, P. (1991b). A simple PD controller for robots with elastic joints. *IEEE Transactions on Automatic Control, 36*(10), 1208-1213. doi:10.1109/9.90238

Tonshoff, H. K., & Kummetz, J. (1999). Active compensation of kinematic transmission errors in servo drives for machine tools and robots,. *Proceedings of the 1999 American Control Conference (Cat. No. 99CH36251), San Diego, CA,, 4*, 2590-2594

Tsai, L.-W. (1999). *Robot Analysis, The Mechanics of Serial and Parallel Manipulators*: John Wiley & Sons, Inc., New York.

Uh, J. H., Oh, J. H., & Lee, J. S. (1998). Tracking control of RLFJ robot manipulator using only position measurements by backstepping method. *In Proc. of the 13th KACC, international session*.

Wang, C., Minghui, Z., Wang, Z., & Tomizuka, M. (2016, 16-21 May 2016). *Robust two-degree-of-freedom iterative learning control for flexibility compensation of industrial robot manipulators.* Paper presented at the 2016 IEEE International Conference on Robotics and Automation (ICRA).

Wang, C., Zheng, M., Wang, Z., Peng, C., & Tomizuka, M. (2017). Robust Iterative Learning Control for Vibration Suppression of Industrial Robot Manipulators. *Journal of*

Dynamic Systems, Measurement, and Control, 140(1), 011003-011003-011009. doi:10.1115/1.4037265

Wang, L., Freeman, C. T., & Rogers, E. (2016). Predictive iterative learning control with experimental validation. *Control Engineering Practice, 53*, 24-34. doi:https://doi.org/10.1016/j.conengprac.2016.04.001

Wang, Y., Tian, D., Dai, M., Shen, H., & Jia, P. (2018, 9-11 March 2018). *Similarity analysis of disturbance observer and active disturbance rejection control for typical motor-driven system.* Paper presented at the 2018 IEEE 15th International Workshop on Advanced Motion Control (AMC).

Wilson, G. A., & Irwin, G. W. (1993). *Tracking control of manipulators with elastic joints.* Paper presented at the Second IEEE Conference on Control Applications.

Xu, W., Chu, B., & Rogers, E. (2014). Iterative learning control for robotic-assisted upper limb stroke rehabilitation in the presence of muscle fatigue. *Control Engineering Practice, 31*, 63-72. doi:https://doi.org/10.1016/j.conengprac.2014.05.009

Yamada, S., Inukai, K., Fujimoto, H., Omata, K., Takeda, Y., & Makinouchi, S. (2015, 22-24 July 2015). *Joint torque control for two-inertia system with encoders on drive and load sides.* Paper presented at the 2015 IEEE 13th International Conference on Industrial Informatics (INDIN).

Yan, M.-T., & Shiu, Y.-J. (2008). Theory and application of a combined feedback–feedforward control and disturbance observer in linear motor drive wire-EDM machines. *International Journal of Machine Tools and Manufacture, 48*(3), 388-401. doi:https://doi.org/10.1016/j.ijmachtools.2007.09.006

Yang, J., Chen, W., Li, S., Guo, L., & Yan, Y. (2017). Disturbance/Uncertainty Estimation and Attenuation Techniques in PMSM Drives—A Survey. *IEEE Transactions on industrial electronics, 64*(4), 3273-3285. doi:10.1109/TIE.2016.2583412

Yeon, J., Yim, J., & Park, J. (2011). Robust control using recursive design method for flexible joint robot manipulators. *Journal of Mechanical Science and Technology, 25*(12), 3205-3213. doi:10.1007/s12206-011-0822-0

Yeşildirek, A., Vandegrift, M. W., & Lewis, F. L. (1996). A neural network controller for flexible-link robots. *Journal of Intelligent and Robotic Systems, 17*(4), 327-349. doi:10.1007/BF00571697

Yin-Chieh, C., & Jinsiang, S. (2011, 21-23 Nov. 2011). *A Regressor Free Adaptive Backstepping Design of Flexible Joint Robot Based on Function Approximation Technique.* Paper presented at the First International Conference on Robot, Vision and Signal Processing (RVSP).

Yun, J. N., & Su, J. (2014). Design of a Disturbance Observer for a Two-Link Manipulator With Flexible Joints. *IEEE Transactions on Control Systems Technology, 22*(2), 809-815. doi:10.1109/TCST.2013.2248733

Yun, J. N., Su, J., Kim, Y. I., & Kim, Y. C. (2013). Robust Disturbance Observer for Two-Inertia System. *IEEE Transactions on industrial electronics, 60*(7), 2700-2710. doi:10.1109/TIE.2012.2194976

Zhang, Q., Yang, S., Liu, H., Xie, C., Cao, Y., & Wang, Y. (2018). *Real-Time Implementation of a Joint Tracking System in Robotic Laser Welding Based on Optical Camera*, Singapore.

Zhao, Z.-L., & Guo, B.-Z. (2015). On active disturbance rejection control for nonlinear systems using time-varying gain. *European Journal of Control, 23*, 62-70. doi:https://doi.org/10.1016/j.ejcon.2015.02.002

Zinn, M., Khatib, O., Roth, B., & Salisbury, J. K. (2003). A new actuation approach for human friendly robot design. In B. Siciliano & P. Dario (Eds.), *Experimental Robotics VIII* (pp. 113-122, 2003). Berlin, Heidelberg: Springer Berlin Heidelberg.